Summer 2021

Computational Analysis of Type 3 Iodothyronine Deiodinase: Potential Inhibitors, Substrate Binding, and Dimer Structure

Eric Scott Marsan
Old Dominion University, emarsan@odu.edu

COMPUTATIONAL ANALYSIS OF TYPE 3 IODOTHYRONINE DEIODINASE: POTENTIAL INHIBITORS, SUBSTRATE BINDING, AND DIMER STRUCTURE

by

Eric Scott Marsan
B.S. May 2015, Christopher Newport University

A Dissertation Submitted to the Faculty of
Old Dominion University in Partial Fulfillment
of the Requirements for the Degree of

DOCTOR OF PHILOSOPHY

CHEMISTRY

OLD DOMINION UNIVERSITY
August 2021

Approved by:

Craig Bayse (Director)

Erin Purcell (Member)

Alvin Holder (Member)

Jennifer Poutsma (Member)

Jing He (Member)

ABSTRACT

COMPUTATIONAL ANALYSIS OF TYPE 3 IODOTHYRONINE DEIODINASE: POTENTIAL INHIBITORS, SUBSTRATE BINDING, AND DIMER STRUCTURE

Eric Scott Marsan
Old Dominion University, 2020
Director: Dr. Craig Bayse

Thyroid hormones (THs) in mammalian tissues are crucial for development and maintaining metabolic homeostasis. Iodothyronine deiodinases (Dios) remove iodines from THs by a selenocysteine (Sec) residue, which either activates or inactivates them. Halogen bonding (XB) has been proposed to describe the interaction between the Se and I atoms of the T_4-Dio complex. Disruption of TH homeostasis by xenobiotics, such as polybrominated diphenyl ethers (PBDEs) and polychlorinated biphenyls (PCBs) can cause deleterious effects on the endocrine system. Experimental studies have indicated that PBDEs and PCBs could disrupt TH homeostasis by inhibiting Dio through XB formation. However, no current quantitative study exists that compares the relative strengths of PBDE and PCB XB strengths. Trends in XB interactions of a small model of the active site ($MeSe^-$) with THs and potential inhibitors PBDEs and PCBs are analyzed using density functional theory (DFT). In agreement with trends in XB, XB favorability follows in the order of THs > PBDEs > PCBs (i.e., I > Br > Cl). Highly brominated PBDEs show similar interaction energies to THs, suggesting possible inhibition and debromination of these compounds.

Schweizer et al. solved the crystal structure of the monomeric catalytic domain of Dio3. However, Dio3 must dimerize in order to perform catalytic deiodination, and no structural data currently exists regarding a Dio3 dimer. A debate between two groups has been ongoing in the literature regarding how Dio3 undergoes dimerization. Proposed Dio3 dimer structures by Sagar and Schweizer may be attributed to the observance of A-type and B-type dimers within peroxiredoxins (Prxs). Sequential comparisons using Clustal Omega of Dio3 to known A-type and B-type dimers show the B-type dimerization dimerization is more plausible for Dio3. I*n silico* protein-protein docking databases

SymmDock and GalaxyRefineComplex were employed to successfully construct a Dio3 dimer based upon the B-type description. The refined Dio3 dimer was subject to MD simulations to test for the stability of the dimer. MMGBSA calculations show formation of the dimer is stable and interdimer interactions between the β-sheets and α-helices stabilize the dimer.

This dissertation is dedicated to all who have aided me
throughout the graduate school process.

ACKNOWLEDGMENTS

I would like to thank my committee members, especially my advisor Dr. Craig Bayse, for their wisdom and guidance throughout the writing and preparation of this dissertation. I would also like to thank my family for their unyielding support to help push me to achieve my goals. Finally, I would like to thank the chemistry faculty at Christopher Newport University for their encouragement to pursue my degree.

NOMENCLATURE

TTR	Transthyretin
$\Delta E_{D\rightarrow A}$	Donor-acceptor interaction energy, kcal mol^{-1}
ΔE_{ZPE}	Zero-point correction energy, kcal mol^{-1}
EDC	Endocrine disrupting chemicals
XB	Halogen bonding
IRD	Inner ring deiodination
MM	Molecular Mechanics
MD	Molecular Dynamics
ORD	Outer ring deiodination
Prx	Peroxiredoxin
PBDE	Polybrominated diphenyl ether
PCB	Polychlorinated biphenyl
Sec	Selenocysteine
TBG	Thyroid-binding globulin
Dio1	Type I Iodothyronine Deiodinase
Dio2	Type II Iodothyronine Deiodinase
Dio3	Type III Iodothyronine Deiodinase
Gpx	Glutathione Peroxidase
Trx	Thioredoxin

TABLE OF CONTENTS

Page

LIST OF TABLES xi

LIST OF FIGURES x

Chapter

1. INTRODUCTION 1

2. HALOGEN BONDING INTERACTIONS OF POLYBROMINATED DIPHENYL ETHERS AND THYROID HORMONE DERIVATIVES: A POTENTIAL MECHANISM FOR INHIBITION OF IODOTHYRONINE DEIODINASE 11
   - 2.1 INTRODUCTION 11
   - 2.2 RESULTS AND DISCUSSION 14
   - 2.3 CONCLUSIONS 27
   - 2.4 COMPUTATIONAL METHODS 28

3. HALOGEN BONDING INTERACTIONS OF POLYCHLORINATED BIPHENYLS AND THE POTENTIAL FOR THYROID DISRUPTION 29
   - 3.1 INTRODUCTION 29
   - 3.2 RESULTS AND DISCUSSION 32
   - 3.3 CONCLUSIONS 41
   - 3.4 COMPUTATIONAL METHODS 42

4. AN *IN SILICO* APPROACH TO ELUCIDATE A DIMERIC STRUCTURE OF IODOTHYRONINE DEIODINASE III 43
   - 4.1 INTRODUCTION 43
   - 4.2 RESULTS AND DISCUSSION 45
   - 4.3 CONCLUSION 67
   - 4.4 COMPUTATIONAL METHODS 68

5. CONCLUSION 70

REFERENCES 72

APPENDICES 87
   - A. COMPLETE TABLE OF PBDE DATA 87
   - B. COMPLETE LIST OF PCBs WITH THEIR CORRESPONDING STRUCTURES 91
   - C. COMPLETE TABLE OF PCB DATA 99
   - D. LICENSE FOR USE OF CHAPTER 2 IN DISSERTATION 123
   - E. LICENSE FOR USE OF CHAPTER 3 IN DISSERTATION 124

VITA 125

LIST OF TABLES

Table Page

1. Optimized geometries of the TH derivatives, XB position, activation of C-I bond (Δd(C—I)), XB distance (d(I—Se)), energy of complex formation (ΔE_{ZPE}), and donor-acceptor energies ($\Delta E_{D\rightarrow A}$) using the mPW1PW91/TZVP basis set 15

2. Oligomer template structural data generated by GalaxyGemini for $Dio3_{(\mathbf{X\text{-}ray})}$ and $Dio3_{(\mathbf{C})}$ 53

3. Binding energies (in kcal mol^{-1}) of the top 10 models of $Dio3_{(\mathbf{X\text{-}ray})}$ and $Dio3_{(\mathbf{C})}$ predicted by HawkDock 54

4. List of results generated from GalaxyRefineComplex and their respective ligand RMSDs 58

5. Energy of hydrogen bonds along the dimer interface region of Dio3 during the *holo* simulation 64

6. Energy of hydrogen bonds along the dimer interface region of Dio3 during the *apo* simulation 64

7. List of all notable hydrogen bonds and interactions in the other B-type proteins examined in this study 65

LIST OF FIGURES

Figure Page

1. Structures of thyroxine (T_4) and triiodothyronine (T_3) 1

2. Biosynthetic process of THs within the thyroid follicular cells 3

3. Overview of the general mechanistic pathway of TH transport 4

4. Pathways of metabolism of THs 5

5. Pathways for deiodination of THs by the iodothyronine deiodinase family of selenoproteins 12

6. PBDE/OH-BDEs mechanisms of inhibition towards the transport protein transthyretin (TTR) and Dio2 13

7. XB interactions as described by A) MO model; B) valence bond model 14

8. LUMOs and next-lowest LUMO energies for TH derivatives, and the correlation of ΔE_{ZPE} to the LUMO energy 18

9. Structures of iopanoic acid and tyropanoic acid 19

10. Structures of PBDEs/OH-BDEs used in this study 20

11. Comparison of bond distances by A) XB position and B) degree of bromination and donor-acceptor energy by C) XB position and D) degree of bromination 21

12. LUMO orbitals containing the lowest energy and the next-lowest energy for 2a-HO-BDE-28 (4 Brs), 3-HO-BDE-47 (4 Brs), 6-HO-BDE-157 (6 Brs), and 3a-HO-BDE-154 (6 Brs) 22

13. Comparison of the activation of C-Br with respect to ΔE_{ZPE} in the PBDEs/OH-BDEs by A) XB location; B) degree of bromination 24

14. DFT optimized structures of selected compounds, with their corresponding ΔE_{ZPE} values 26

15. Selected sample structures of PCBs and TCDD 30

16. XB interactions as described by the molecular orbital model 31

17. Comparison of donor-acceptor energies vs. *d*(C-Cl) by A) XB position and B) degree of bromination and donor-acceptor energy and donor-acceptor energies vs. *d*(Cl-Se) by C) XB position and D) degree of bromination 33

18. Comparison of zero-point energy corrected interaction energies (ΔE_{ZPE}) to A) the activation of the C-Cl bond (Δd(C-Cl)) by XB position; B) percent contribution of X (%X) by XB position 34

19. XB interactions at both the *meta* and *para* positions respectively, along with the LUMO orbitals containing the lowest and next-lowest energies for PCB-77 35

Figure Page

20. Pathways of TH inner ring and outer ring deiodination (IRD, ORD) and their byproducts, with PCBs that may specifically target Dio2 (PCB-80) and Dio3 (PCB-54) respectively 38

21. PES curves for the rotation around the central bond of PCBs with various *ortho*-substitution patterns 39

22. Template structures used as the basis for describing Dio3 dimerization 45

23. Decameric structure of plasmodium vivax Prx1a (PDB = 4L0U) and a close-up of the A-type and B-type dimer interfaces with key regions of each interface highlighted in opaque 46

24. Sequence alignment of Dio3 (4TR4) vs. A-type dimer proteins 47

25. Sequence alignment of Dio3 (4TR4) vs. B-type dimer proteins 48

26. Structures of comparable 'ball-and-socket' interactions within A) 1ERU; B) 1XIY; C) 3I43 49

27. Structural overlays of Dio3 monomers (in blue, pink) on top of dimeric structures of A) 1XIY; B) 3I43 (in tan) 51

28. Structures of the template structures generated using the Galaxy server with the structure of Dio3 as the input with templates (A) 3HA9; (B) 2P5Q 54

29. Structure of the B-type (model 6) dimer generated from $Dio3_{(C)}$ using the HawkDock Server 55

30. Dimers generated from the SymmDock server 56

31. Overlays of the high-quality models generated by GalaxyRefineComplex according to CAPRI 58

32. Evolution of interaction energy profiles in the $Dio3_{(C)}$ dimer interface region 60

33. Evolution of interdimer interactions at the $Dio3_{(C)}$ dimer interface region 60

34. Statistical analysis of the MD simulation of the $Dio3_{(C)}$ dimer after the 2 T_4 residues are removed 61

35. Distance plots of the two stable hydrogen bonds between Met270-Gln272 backbone atoms; B) initial and final structures of the Met270-Gln272 hydrogen bonding interactions 63

36. Comparison of the orientation of Arg291 in Dio3 to A) Arg156 of 1QQ2; B) Arg161 of 2P5R; C) Arg187 of 4KCE 67

CHAPTER 1

INTRODUCTION

Thyroid hormones (THs) were first isolated by Edward Calvin Kendall in 1915. He was eventually awarded (along with his colleagues Tadeusz Reichstein and Phillip Hench) a Nobel Prize in Physiology and Medicine for his contribution.[1] These biomolecules are essential for many bodily processes such as body temperature regulation, digestion, bone growth, and heart rate.[2–5] Thyroid hormones, in the form of thyroxine (T_4) or triiodothyronine (T_3), are secreted in a roughly 14:1 ratio from the thyroid gland upon binding of a thyroid stimulating hormone (TSH) (Figure 1).[6,7] These hormones contain the essential trace element iodine, which can be obtained from a diet consisting of vegetables, seafood, and iodized table salt.[8] Insufficient iodine intake leads to reduced production of thyroid hormones, causing hypothyroidism, goiter, and cretinism.[9,10] On the other hand, excessive iodine intake from diet can lead to a surplus in TH levels, leading to hyperthyroidism, diarrhea, irregular heartbeats (arrhythmia), and thyroid enlargement.[11]

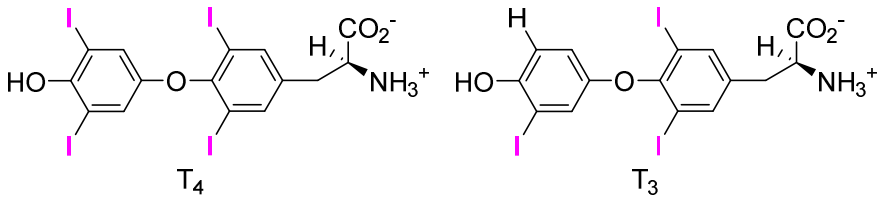

Figure 1. Structures of thyroxine (T_4) and triiodothyronine (T_3).

Fortunately, there are treatments and preventive measures in place for TH imbalances by hypothyroidism or hyperthyroidism. Incorporating iodine into foods, such as by adding salt, can ensure an adequate amount of iodine is available for TH production. In more severe cases of hypothyroidism, combination therapy, which uses levothyroxine (L-thyroxine) and liothyronine (synthetic T_3), has shown some improvement in the well-being of patients, however clinical trials have generally failed to show a noticeable benefit.[12,13] In the case of hyperthyroidism, avoiding foods containing high iodine content is often advised. Like hypothyroidism, treatments are available for hyperthyroidism. Administration of beta-blockers such as propranolol are used to suppress the symptoms of hyperthyroidism, however it has been shown to be an ineffective treatment long-term.[14] In the most extreme cases of hyperthyroidism, radioiodine therapy is commonly performed in which iodine-131 is taken orally to completely suppress the hyperactive thyroid gland.[15] Unfortunately, patients treated using radioiodine therapy have an increased risk of cancer in the stomach, kidney and breast.[15] Because of the shortcomings of the current treatments of hypo- and hyperthyroidism, there is a demand for more effective treatments and/or methods to combat TH imbalances. Understanding the underlying causes of TH imbalances will be paramount for treating endocrine-related diseases and deficits.

The synthetic process of THs occurs over multiple steps and involves the hypothalamus, pituitary gland, and thyroid gland (Figure 2).[2,16,17] First, inorganic iodine is extracted from the bloodstream into the thyroid follicular cell by a unique transport system mediated by the sodium iodide symporter (NIS).[18] The inorganic iodine is then transported through the thyroid follicular cells into the thyroid gland, binding to heme-containing thyroid peroxidase (TPO).[19] TPO is an enzyme within the thyroid gland that begins the organification process of iodines for use in THs. During iodine extraction, peroxidases (DUOX1 and DUOX2) generate hydrogen peroxide (H_2O_2).[20] H_2O_2 aids in iodination and phenolic coupling of tyrosyl ends of thyroglobulin (Tg) with TPO to form the Tg-T_4/T_3 complex.[20] The Tg-T_4/T_3 complexes are stored in the follicular lumen.[2] As TSH concentration increases, the Tg-T_4/T_3 complexes are slowly moved from the lumen into the follicular cells. The T_4 and T_3 residues are then cleaved from the Tg by proteolysis in

preparation for secretion.[2] Upon secretion, THs bind to transport proteins (TPs) such as transthyretin (TTR) or thyroglobulin (TBG) to be transported to various tissues to perform a variety of functions. For example, THs can be transported to the heart to regulate heart rate, or they can be transported to the liver to facilitate cholesterol synthesis (Figure 3).

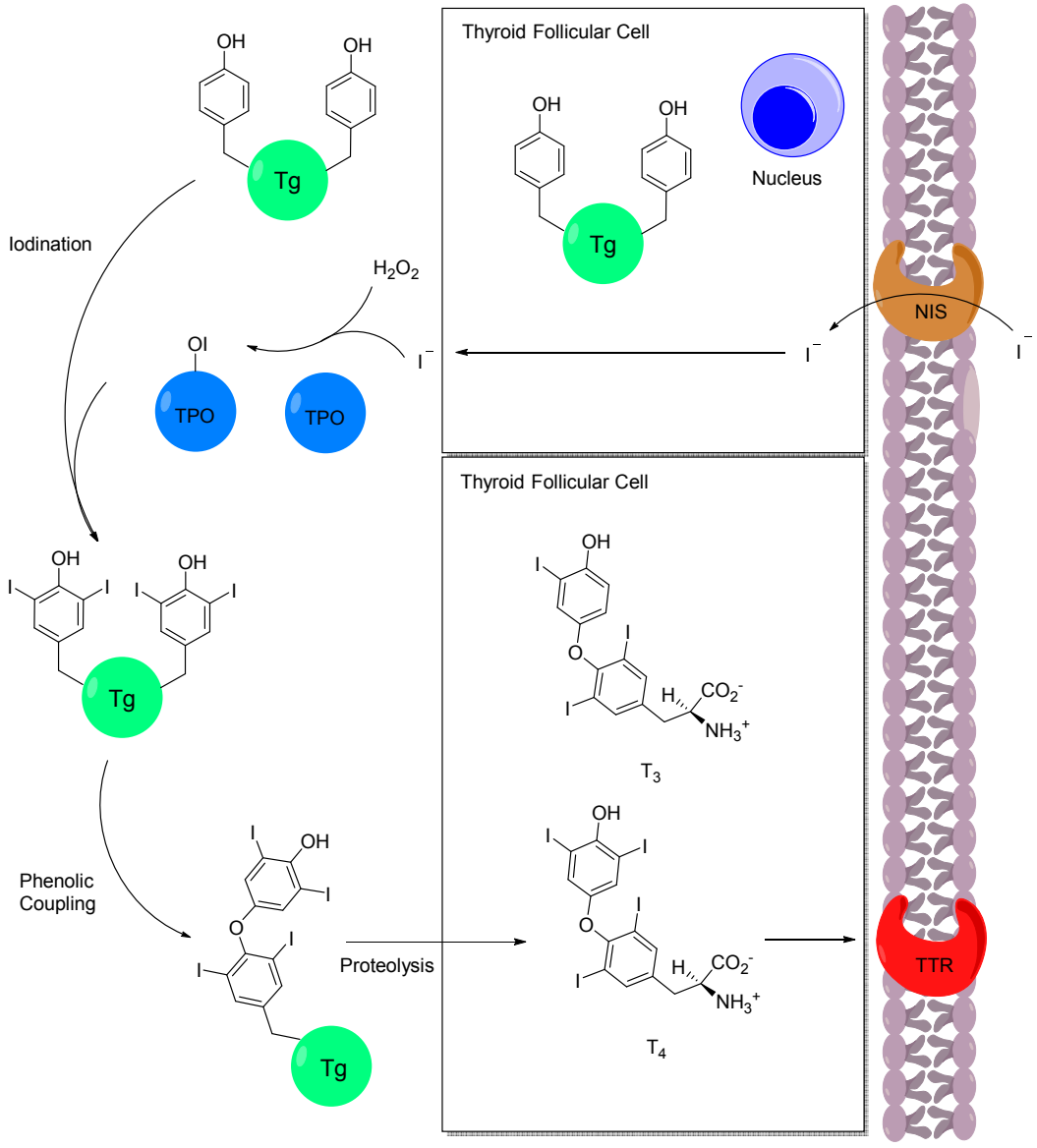

Figure 2. Biosynthetic process of THs within the thyroid follicular cells.

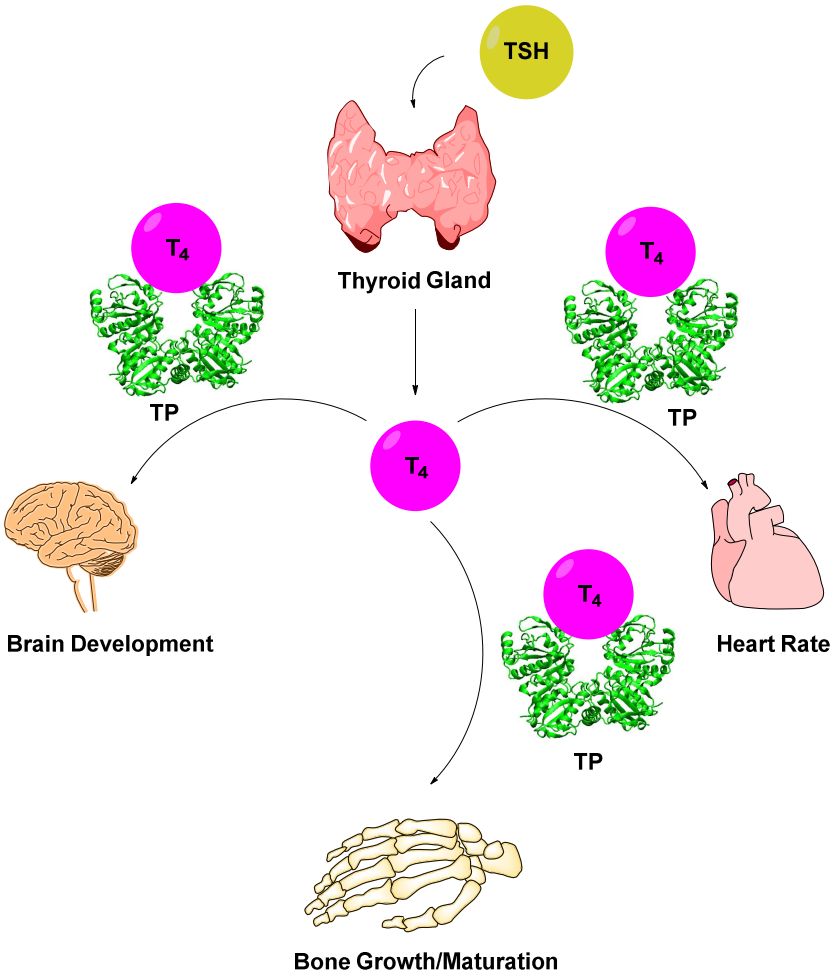

Figure 3. Overview of the general mechanistic pathway of TH transport. Adapted from ref. 2.

When THs reach their designated location, they may be metabolized in many ways.[21] Sulfation or glucuronidation of THs by cytosolic sulfotransferases (SULTs) or 5'-diphosphate-glucuronosyltransferases (UGTs) inactivates THs.[22] These pathways are considered 'reservoirs' for the active thyroid hormones, as both processes are reversible.[22] THs can also be deaminated or decarboxylated to form iodothyroacetic acids or iodothyronamines (TAMs) respectively (Figure 4).[23,24] Decarboxylation of THs to TAMs is a common pathway in the brain, as TAMs bind to trace amine-associated receptors (TAARs) to ease neurotransmitter usage.[25–27] On the other hand, *in vivo* studies of iodothyroacetic acids (TA_4 or Tetrac) show these compounds suppress TH secretion by inhibiting

receptor sites on TSH.[28] Finally, THs can have their iodines removed by iodothyronine deiodinases (Dios), which activates or inactivates THs, thereby regulating TH homeostasis.

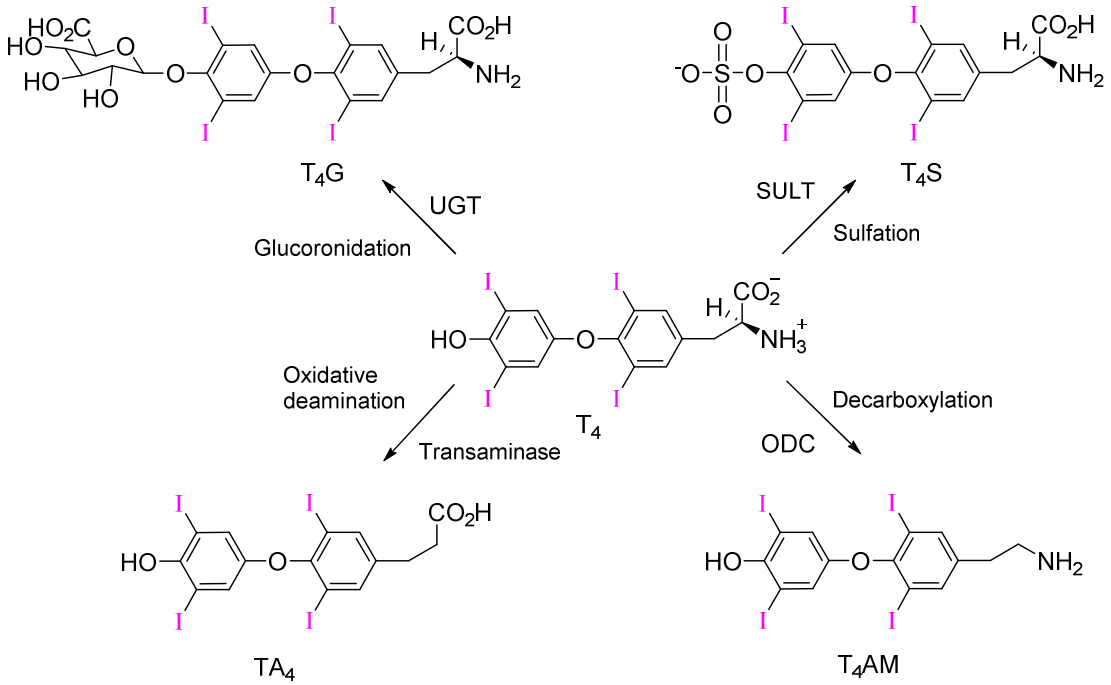

Figure 4. Pathways of metabolism of THs.

Dios constitute three separate proteins, Dio1, Dio2 and Dio3, that are encoded by separate genes and each is involved in regioselective deiodination of THs.[29] These proteins have been studied for nearly half a century and the roles and features of these proteins are well-defined. The most notable feature of these proteins is that they are classified as selenoenzymes, meaning they contain a selenocysteine (Sec) residue embedded within the active site.[30] The Sec residue has been proposed to directly participate in deiodination, and mutation of Sec either reduces or completely suppresses Dio activity.[31] In vertebrates, Dio2 and Dio3 are highly expressed during developmental stages and are essential for regulating TH levels in tissues and the bloodstream.[32] Overexpression of Dio activity has been implicated in disease

states. For example, excessive Dio3 activity leads to consumptive hypothyroidism, where the production of T_3 becomes much faster than the ability of the thyroid gland to secrete THs.[33] Consumptive hypothyroidism can lead to many ailments, including increased weight gain, depression, and goiter.[34] Structurally, all Dios adopt a thioredoxin (Trx) fold and have a Dio-insertion region between β_2 and α_D that is overlooked by an unstructured loop-D. Loop-D has been proposed to aid substrate binding due to its proximity to the active site.[35] This unstructured loop region has a conserved N-terminal AHxxDGW sequence across the Dio family, however the length and sequence of the loops vary greatly.[36] Halogen bonding (XB) has been proposed as a mechanism in which Dio removes an iodine from THs through formation of a strong Se—I bond between a TH iodine and the Sec selenium.[37] XB is supported experimentally through a study involving naphthyl-based deiodinase mimics which show deiodination activity through chalcogen and halogen bonding and by the crystal structure of monomeric Dio3.[35,38]

One area to be addressed in this study is how endocrine disrupting chemicals (EDCs), such as polybrominated diphenyl ethers (PBDEs) and polychlorinated biphenyls (PCBs), affect Dio activity. PBDEs and PCBs are used primarily in commercialized products to increase flame resistance.[39,40] Excess intake of organohalogen EDCs has been shown to have long-term negative health effects such as cardiovascular diseases and hypo/hyperthyroidism.[2,6] Prenatal exposure to EDCs has been associated with impaired thyroid function, leading to lower levels of free T_4 and T_3 in circulation.[41] In addition, industrial runoff of these PCBs has shown to contaminate the Michigan water supply, which has led to a civil court case of Michigan v. Robert Massey over a violation of the Clean Water Act.[42] Experimental studies have shown these EDCs can suppress Dio activity leading to decreased serum T_3 and rT_3 levels.[43–45] EDCs could form X—Se XB interactions to active site Sec similar to THs. However, no quantitative study currently exists in the literature that compares the relative strengths of the interactions between EDCs and Dio.

Another problem regarding research on Dio3 is the lack of a solved dimeric structure of Dio3. While structural data exists for monomeric Dio3, this is the inactive form of the protein. An experimental

study involving fluorescence resonance energy transfer (FRET) shows Dio3 is catalytically active only as a homodimer.[46] In addition, within the literature, there are conflicting viewpoints regarding the interface of the Dio3 dimer.[35,47] Resolving a dimeric structure based upon the isolated monomeric structure of the catalytic region would be an essential first step to help expand our understanding of the structural and catalytic aspects of Dio3.

In this dissertation, computational (i.e., *in silico*) methods are used to determine and identify the key interactions between Dio and halogenated aromatics and potential Dio inhibitors (THs, PBDEs, PCBs) on an atomistic level. *In silico* techniques have two distinct advantages over experimental methods. Biochemical systems can be viewed at the atomistic level, which allows key interactions within systems, such as salt bridges, hydrogen bonds, and van der Waals interactions to be easily identified. Visualization programs such as Visual Molecular Dynamics (VMD), CHIMERA, and Pymol are commonly used for inspection of proteins and biochemical systems.[48–50] *In silico* techniques also have the advantage of being highly flexible and/or adaptable. A user can 'fine-tune' the parameters of a system, such as temperature, pH, volume, pressure, and salt concentration, to emulate typical experimental conditions of a given system. *In silico* techniques are also useful for predicting the efficacy of small molecules of a given biological system before they are synthesized.[51,52] A combination of *in silico* methods, Density Functional Theory and Molecular Dynamics, have been employed to visualize and describe XB interactions within Dio.

Density Functional Theory (DFT) is a quantum-mechanical computational technique first derived in the 1960s by Hohenberg and Kohn.[53] Although DFT was technically first described by Thomas and Fermi in the 1920s, the applications were largely limited due to electron correlation being neglected.[54] DFT has been shown over the past three decades to be versatile and have growing applications in the areas of computational physics, computational chemistry, and material sciences. The mathematical basis of DFT is summarized via the Hohenberg and Kohn (H-K) theorem.[53] The theorem states the structural and electronic properties of many-atom systems can be described quantum mechanically by using

functionals of the electron density.[53] Hohenberg and Kohn considered a system enclosed in a box with an arbitrary number of electrons and moving with the external potential function $v(r)$ and repulsive forces. The resulting Hamiltonian and the corresponding terms are given below (eqs. 1-4):

$$H = T + V + U \tag{1}$$

$$T = \frac{1}{2}\int \nabla\psi^*(r)\,\nabla\psi(r)dr \tag{2}$$

$$V = \int v(r)\psi^*(r)\,\psi(r)dr \tag{3}$$

$$U = \frac{1}{2}\int \frac{1}{|r-r'|}\psi^*(r)\,\psi^*(r')\psi(r')\psi(r)drdr' \tag{4}$$

The authors then showed that in the ground state **ψ**, the electron density of the system can be written as eq (5), which shows the electron density $n(r)$ is a functional of the external potential $v(r)$:

$$n(r) = (\boldsymbol{\psi}, \psi^*(r)\psi(r)\boldsymbol{\psi}) \tag{5}$$

Within DFT, natural bond orbital (NBO) theory emerged as a method for analyzing hybridization and covalency effects in polyatomic molecules.[55,56] The input atomic orbital (AO) basis set (χ_i) undergoes a series of transformations to distinct localized basis sets through natural atomic orbitals (NAOs) and natural hybrid orbitals (NHOs), which is automated through the use of the NBO program in the Gaussian09 software package.[57] NBOs are the calculated bonding orbitals with the highest possible electron density, giving the most accurate representation of **ψ** for a system.[55] NBO calculations were used previously to quantitatively assess XB strengths of Dio model complexes to THs in terms of donor-acceptor ($\Delta E_{D\rightarrow A}$) energies.[37] $\Delta E_{D\rightarrow A}$ energies are correlated to the mixing of the lone-pair orbital fragment of a nucleophilic base and an antibonding σ* R-X orbital, which results in a stronger XB interaction. Methyl selenolate ($MeSe^-$) was found to form the strongest interaction to the TH model compounds by roughly 25 kcal mol^{-1}.[37] In this dissertation, NBO calculations were performed using the same $MeSe^-$ donor to PBDEs and PCBs and were compared to THs to see the overall trends in XB strengths across all three groups. In addition, NBO analysis was used to assess how substitution patterns

(*ortho*, *meta*, *para*) or degree of halogenation affected the relative XB strengths within each grouping. For these DFT calculations, the MPW1PW91 and M062X functionals were employed, which have been shown by display a high level of accuracy over a variety of systems.[58]

Molecular Mechanics (MM) is a computational technique that approximates motions of atoms and molecules using classical Newtonian mechanics.[59] Quantum mechanical motions of large systems are too complex to calculate for even the best supercomputers. MM bypasses the barrier of calculating quantum-mechanical motions by instead treating the system via molecular mechanics as shown in eq (6):

$$E_{total} = \sum_{bonds} K_r(r - r_{eq}) + \sum_{angles} K_\theta(\theta - \theta_{eq}) + \sum_{dihedrals} \frac{V_n}{2}[1 + \cos(\mathrm{n}\emptyset - \gamma)] + \sum_{i<j}[\frac{A_{ij}}{R_{ij}^{12}} - \frac{B_{ij}}{R_{ij}^{6}} + \frac{q_i q_j}{\epsilon R_{ij}}] \quad (6)$$

where the first two terms represent the van der Waals contributions from individual bonds, angles, and dihedrals between atoms. The latter term, the Lennard-Jones potential, takes into account the Coulombic (electrostatic) interactions of the system.[60] Bonds and angles between atoms are treated as virtual springs, while dihedral angles are represented by sinusoidal functions that account for energetic differences between staggered and eclipsed conformations.[61] These forces are often parameterized to agree with known experimental structures, such as NMR or spectroscopic data. Parameterization is needed to identify ideal charges of atoms, van der Waal radii of atoms, and length and stiffness of springs, which in turn describes the 'force field'.[61] Many different force fields, such as CHARMM, GROMOS, and AMBER, are implemented within MD simulation packages and have steadily improved in accuracy.[62–69] The primary application of MM is in molecular dynamics (MD), which is an *in silico* simulation-based method to track and analyze the motions of atoms and molecules within a given system.

To carry out an MD simulation, an initial model of a protein or molecule (usually a crystal or an NMR structure, although other initial structures or models can be used) is placed in solution, typically water. As the MD simulation is carried out, the atoms of the system move according to eq (6), which produces a trajectory of the system. This in turn advances the time of the simulation, which is dependent on the step size of the system. These steps are typically on the order of femtoseconds or nanoseconds

depending on accuracy. This process is repeated millions to billions of times depending on simulation length, which often require computer clusters or supercomputers to run the calculations in a timely manner. These trajectories can then be viewed by a visualization program such as Visual Molecular Dynamics (VMD), CHIMERA, or Pymol.[48–50] MD simulations of dimeric Dio3 could provide insight into what the key residue(s) are that hold the dimer interface together and how they change over the course of the simulation. Data can be extracted from the trajectory files, such as hydrogen bonding distances, by using *CPPTRAJ,* which is the main program used by AMBER to process trajectory files.[70] Overall protein and individual residue movements can be determined by plotting the root mean square deviation (RMSD) or the root mean square fluctuation (RMSF) respectively. RMSD calculations can be used to determine the stability of the Dio3 dimer over the course of a simulation. Hydrogen bond breaking or formation over an MD simulation can be tracked via distance plots and can identify the persistent hydrogen bonding interactions in the Dio3 dimer.

In summary, this dissertation attempts to tackle two main questions: 1) can *in silico* methods be used to model XB interactions of PBDEs and PCBs to a small model of the Dio3 active site, and how do the substitutional preferences (*ortho, meta, para*) and degree of halogenation affect the strength of the XB interaction; 2) given the crystal structure of monomeric Dio3, can a dimer of Dio3 be constructed using known *in silico* protein-protein docking databases, and what are the key interactions that hold the dimer together during an MD simulation. This dissertation is divided into three separate chapters: Chapter 2 discusses halogen bonding of PBDEs to a small model of the active site of Dio3 using DFT. Chapter 3 extends the application of Chapter 2 towards PCB XB interactions to a small model of the active site of Dio3 using DFT. Chapter 4 compares the recently solved crystal structure of Dio3 to those of other thioredoxin-fold dimers along with the results of MD simulations of constructed Dio3 dimers using *in silico* databases.

CHAPTER 2

HALOGEN BONDING INTERACTIONS OF POLYBROMINATED DIPHENYL ETHERS AND THYROID HORMONE DERIVATIVES: A POTENTIAL MECHANISM FOR INHIBITION OF IODOTHYRONINE DEIODINASE[a]

2.1 Introduction

Thyroid hormones (THs) play a crucial role in neurodevelopment, particularly in the early stages of life.[2–4,17,71,72] The thyroid pro-hormone thyroxine (T_4) and, to a lesser extent, the active triiodothyronine (T_3) are synthesized in the thyroid by iodination of the amino acid tyrosine by thyroglobulin (TBG).[73,74] THs are secreted upon stimulation by thyroid stimulating hormone (TSH).[75] T_4 is transported to target cells based on metabolic and/or developmental needs and activated by the iodothyronine deiodinase (Dio) family of selenoproteins. Three Dio classes regioselectively deiodinate TH derivatives to maintain TH homeostasis which is essential for many functions such as regulation of body temperature, bone growth, heart rate, and digestion.[76,77] Dio1 deiodinates both the inner and outer rings of T_4 to form the active hormone T_3 and the inactive hormone rT_3, respectively.[78,79] Dio2 is specific to the outer ring deiodination, and Dio3 targets only the inner ring (Figure 5). T_3 and rT_3 can undergo further deiodination to diiodothyronines (3,3'-T_2, 3,5- T_2, or 3',5'-T_2) depending on mechanism of deiodination. The 3,5-T_2 isomer exhibits thyromimetic properties and activates thyroid receptors (TRs) to allow for T_4 transport and to maintain TH homeostasis.[2,80,81] Further order deiodinations can produce lower-order mono- and diiodinated THs.[2] Disruption of TH homeostasis causes severe side effects such as structural abnormalities, hearing loss, cardiovascular diseases, and hypothyroidism.[82–87]

[a] This chapter was adapted from an article in *Chem Eur. J.* For the full citation, see ref. 39.

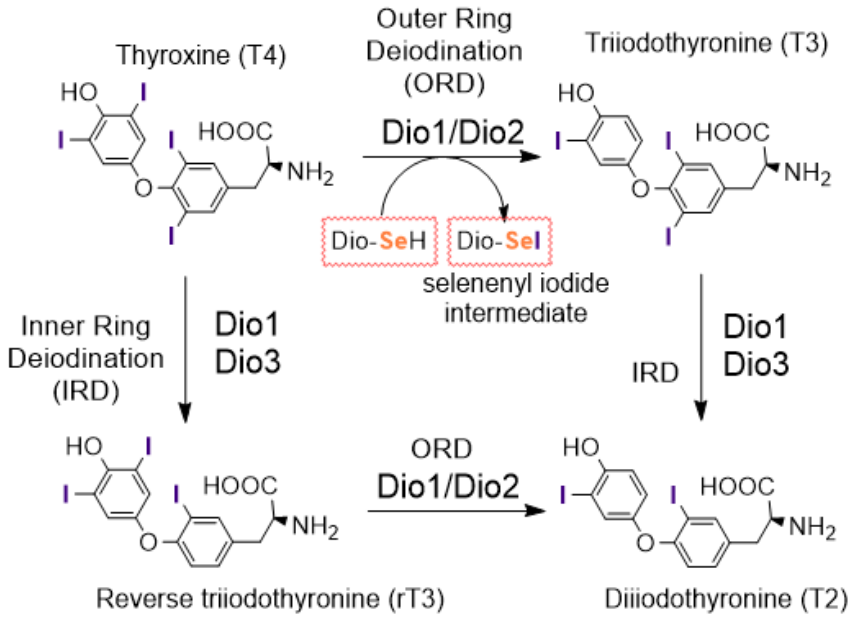

Figure 5. Pathways for deiodination of THs by the iodothyronine deiodinase family of selenoproteins.

Polybrominated diphenyl ethers (PBDEs) are well-known TH disruptors[88–90] and are widely used in various household products to increase flame resistance.[91] Humans are exposed to PBDEs via inhalation or ingestion of contaminated house dust.[45] Bioaccumulation in breast milk can cause adverse developmental effects for the nursing child.[92] As a result, many formulations of PBDEs have been banned.[89] Although PBDEs have been implicated in neurotoxicity, the mechanism of disruption has yet to be determined, although many theories have emerged.[93] For example, PBDEs and their hydroxylated metabolites (OH-BDEs), in particular, may interfere with T_4 transport by interacting with transport proteins, such as transthyretin (TTR, Figure 6A).[94,95] Studies in fish have suggested higher-order PBDEs (> 5 Br) are debrominated by Dio proteins to form lower-order BDEs,[96,97] the most potent congeners for neurotoxicity due to efficient bioaccumulation[96,98,99] and mobility through the atmosphere.[96,97,100,101] Alternatively, the competitive inhibition of Dio2 by PBDEs and OH-BDEs (Figure 6B)[45] may disrupt TH regulation by blocking access to the active site selenocysteine (Sec170) through a Se—Br halogen

bonding (XB) interaction. Our group has proposed a mechanism for deiodination by Dio based upon an initial Se—I XB intermediate between the TH and the selenocysteine residue at the Dio active site.[37] Subsequent experimental studies have supported this novel mechanism, as has the interpretation of the recently solved X-ray structure of the active site region of Dio3.[35]

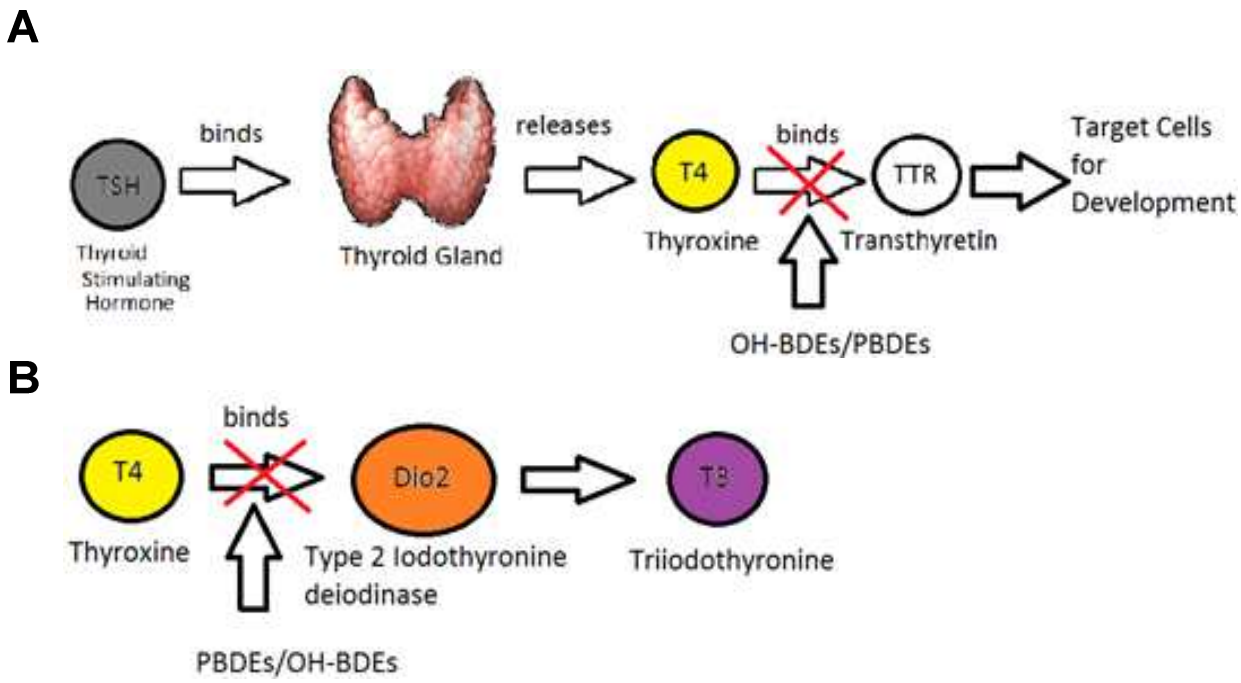

Figure 6. A) PBDE/OH-BDEs inhibit T_4 binding to transport protein transthyretin (TTR); B) PBDE/OH-BDEs inhibit deiodination of T_4 to T_3 by competitive inhibition to Dio2.

XB is an intermolecular interaction between a Lewis base (typically a nucleophile, although there are some exceptions) and a halogen atom.[102,103] The σ-hole model is often used to explain the interaction as the attraction of a donor D for a region of positive electrostatic potential on the otherwise electron-dense halogen.[104] Because the σ-hole lies along the bond axis opposite the R group, the R-X—D bond angle is approximately 180 degrees. Alternatively, a molecular orbital (MO) model can describe XB in terms of the mixing of an antibonding R-X* acceptor orbital and a lone pair (lp) orbital fragment on the

donor (Figure 7A).[37,105,106] The XB interaction becomes more favorable with weaker R-X bonds, which have lower-lying R-X* MOs, and stronger Lewis bases, in which the lp MO is destabilized. Each of these effects enhance mixing of the donor and acceptor MOs to strengthen the interaction. From another perspective, a valence bond (VB) model describes XB in terms of resonance structures similar to those used for three-center-four-electron (3c4e) bonding in hypervalent molecules. Stronger donors and weaker R-X bonds increase the admixture of the right-hand resonance structure to strengthen the XB interaction (Figure 7B). Stabilization of this resonance structure by protonation to RH results in nucleophilic substitution as proposed in our XB-based mechanism.[37] In this study, density functional theory (DFT) calculations compare and contrast the relative XB interactions of THs, iodinated contrast agents and PBDEs/OH-BDEs with $MeSe^-$, a simplified model of the Sec170 residue found at the Dio active site.

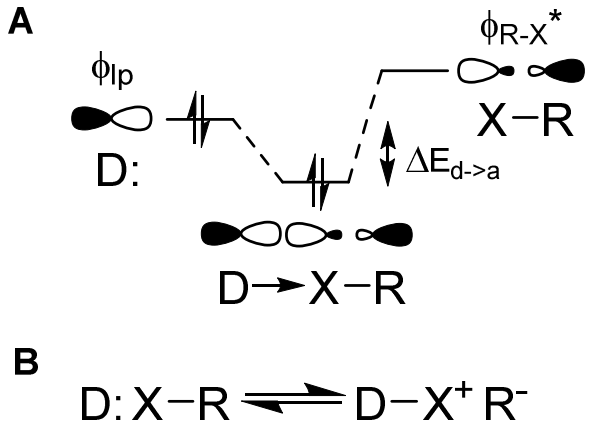

Figure 7. XB interactions as described by A) MO model; B) valence bond model.

2.2 Results and Discussion

Before examining XB to PBDEs/OH-BDEs, we review interactions for various TH derivatives. The geometries for XB complexes of $MeSe^-$ with each unique iodine center of the TH derivatives were calculated at the DFT/mPW1PW91 level (Table 1). From the relative zero-point energies

((ΔE_{ZPE}=E_{ZPE}($MeSe^{-}_{(TH)}$)-E_{ZPE}($MeSe^{-}$)-E_{ZPE}(TH))) and NBO donor-acceptor energies ($\Delta E_{D\rightarrow A}$), the most favorable position for XB depends upon the extent of iodination and is generally stronger for diiodinated rings (average ΔE_{ZPE} = -29.2 kcal mol^{-1}) than for monoiodinated rings (average ΔE_{ZPE} = -25.2 kcal mol^{-1}). For example, T_3 and rT_3 favor XB at the more-substituted inner and outer ring, respectively. Because the potential for nucleophilic substitution (i.e. deiodination) should correlate to XB strength, subsequent reactions would be predicted to occur at the more-substituted ring to form 3,3'-T_2. However, the actual regioselectivity will also depend upon interactions of the TH with residues at the Dio active site. XB interactions with 3,3'-T_2 and 3',5'-T_2 on the outer ring, stabilized by the neighboring hydroxyl group, are more favorable than T_3, consistent with their ability to regulate T_3 levels by binding to Dio3. The THs with monoiodinated rings have less favorable interactions compared to THs with diiodinated rings, as can be shown with 3-T_1 and 3'-T_1 (Table 1); the latter is more stable (ΔE_{ZPE} = -21.41 kcal mol^{-1} versus -27.29 kcal mol^{-1}) consistent with the ability of 3'-T_1 to undergo further deiodination to thyronine (T_0) while 3-T_1 does not.[107] 3-T_1 constitutes the weakest XB interaction for a TH derivative with the selenolate nucleophile, suggesting a threshold interaction strength must be met in order for deiodination to occur.

Table 1. Optimized geometries of the TH derivatives, XB position, activation of C-I bond (Δd(C—I)), XB distance (d(I—Se)), energy of complex formation (ΔE_{ZPE}), and donor-acceptor energies ($\Delta E_{D\rightarrow A}$) using the mPW1PW91/TZVP basis set.

Compound	XB Position	LUMO orb. (energy, a.u.)	d(C—I), Å; (Δd(C—I), Å)	d(I--Se), Å	ΔE_{ZPE}, kcal mol^{-1}	$\Delta E_{D\rightarrow A}$, kcal mol^{-1}
T_4	Inner	LUMO (-0.06401)	2.300 (+0.198)	2.917	-29.59	53.58, 4.18[a]
T_4	Outer	LUMO+1 (-0.06632)	2.282 (+0.169)	2.960	-29.50	45.93, 3.83[a]
T_3	Inner	LUMO (-0.06370)	2.299 (+0.197)	2.922	-28.43	52.87, 3.96[a]
T_3	Outer	LUMO+2 (-0.04955)	2.256 (+0.144)	3.006	-24.84	40.25, 3.03[a]
rT_3	Inner	LUMO+2 (-0.04296)	2.276 (+0.174)	2.953	-25.14	48.43, 3.17[a]

Table 1. Continued.

Compound	XB Position	LUMO orb. (energy, a.u.)	*d*(C—I), Å; (Δ*d*(C—I), Å)	*d*(I--Se), Å	ΔE_{ZPE}, kcal mol^{-1}	$\Delta E_{D\rightarrow A}$, kcal mol^{-1}
rT_3	Outer	LUMO (-0.06980)	2.291 (+0.190)	2.946	-33.07	48.98, 4.12[a]
3,3'-T_2	Inner	LUMO+2 (-0.03952)	2.272 (+0.169)	2.960	-23.56	46.89, 3.20[a]
3,3'-T_2	Outer	LUMO (-0.05416)	2.265 (+0.153)	2.990	-28.46	43.06, 3.61[a]
3,5-T_2	Inner	LUMO (-0.06022)	2.286 (+0.184)	2.942	-26.61	48.51
3',5'-T_2	Outer	LUMO (-0.06672)	2.287 (+0.173)	2.954	-32.02	47.48
3-T_1	Inner	LUMO+1 (-0.03616)	2.262 (+0.158)	2.980	-21.41	43.43
3'-T_1	Outer	LUMO+1 (-0.03303)	2.260 (+0.158)	3.002	-27.29	41.18
Iopanoic Acid	**A**	N/A	2.279 (+0.166)	2.968	-26.83	45.63
Iopanoic Acid	**B**	N/A	2.315 (+0.185)	2.959	-28.10	48.21
Iopanoic Acid	**C**	N/A	2.294 (+0.174)	2.960	-24.31	45.44
Tyropanoic Acid	**A**	N/A	2.301 (+0.197)	2.912	-29.79	54.12
Tyropanoic Acid	**B**	N/A	2.341 (+0.221)	2.901	-31.09	56.78
Tyropanoic Acid	**C**	N/A	2.311 (+0.192)	2.922	-30.79	52.00

[a] Donor-acceptor interaction energies with MeSeH from Manna et al.[108]

These results are consistent with the findings of Manna et al.,[108,109] who modeled the XB interaction of THs with methyl selenol (MeSeH) representing Dio. Se—I interactions for T_4 and T_3 were favored to the inner ring albeit with lower interaction energies due to the use of a neutral selenol donor. The selenolate is used as a Dio model in this study because SeCys is likely to be deprotonated at normal physiological pH. The stronger nucleophilicity of $MeSe^-$ produces larger donor-acceptor energies for the interaction with $MeSe^-$ relative to MeSeH ($\Delta E_{D\rightarrow A}$ = 39.3 kcal mol^{-1} vs 6.5 kcal mol^{-1}).[37]

The trends in XB can be understood in terms of the energy and C-I* character of the TH lowest unoccupied molecular orbitals (LUMOs). In agreement with the MO model for XB (Figure 7A), increased donation into a lower energy C-I* MO strengthens the I—Se interaction and activates the C-I bond leading to lower ΔE_{ZPE} and higher $\Delta E_{D\rightarrow A}$ values (Table 1).[110] ΔE_{ZPE}s correlate with the energy of the C-I*-type LUMOs, which decrease with increased iodination, within each TH analogue (inner-mono < outer-mono ≤ outer-di < inner-di). For T_4, the LUMO is delocalized over both rings with slightly larger C-I* lobes on the inner ring consistent with the slight preference (< 1 kcal mol^{-1}, Table 1) for XB at that position in agreement with the ability of Dio1 to deiodinate at either ring (Figure 5) and the selectivity of organoselenium Dio mimics.[111] However, the specificity of Dio2 for deiodination of the outer ring of T_4 and Dio3 for the inner ring must be governed by additional interactions at the active site.

In lower-order THs, the LUMO is localized on the diiodinated ring: outer for rT_3 and 3',5'-T_2 and inner for T_3 and 3,5-T_2 (Figure 8). The next lowest energy MO with C-I* character tends to be localized on the ring opposite the LUMO (Figure 8); T_4 has its next lowest C-I*-type MO at LUMO+1, while all others are found at LUMO+2. In addition, the energy difference between the LUMO and LUMO+1(+2) is smaller for T_4 than for other THs. Slight non-linearity in the inner-ring correlation plots (Figure 8) are attributed to the less favorable interactions of T_4 and T_3 with the higher energy LUMO+1(+2) inner-ring C-I* MO.

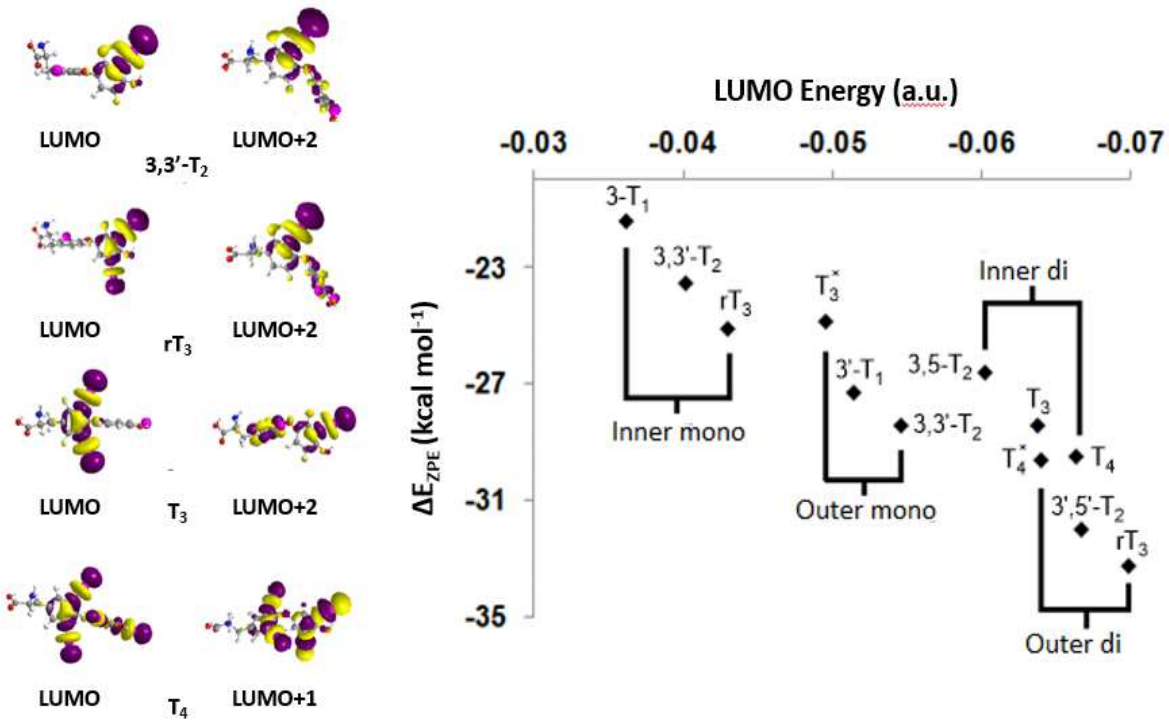

Figure 8. LUMOs and next-lowest LUMO energies for TH derivatives, and the correlation of ΔE_{ZPE} to the LUMO energy. Each TH derivative was grouped based upon the number of iodines on the outer and inner rings. Entries marked with an asterisk indicate an interaction with LUMO+1 (T_4) or LUMO+2 (T_3).

For comparison, XB interactions were modeled with two tri-iodinated contrast agents: iopanoic acid and tyropanoic acid (Table 1 and Figure 9). The former inhibits T_4 expression to treat hyperthyroidism and undergoes deiodination by Dio1.[112] Tyropanoic acid prevents hepatic binding of thyroxine, although its mechanism of inhibition of Dio is not well understood.[113] XB on the iodine adjacent to the two substituents is favorable for both contrast agents ($\Delta E_{D\rightarrow A}$ = 56.78 kcal mol^{-1} and 48.21 kcal mol^{-1}, respectively). The results for iopanoic acid are comparable to the other THs, in agreement with its ability to undergo deiodination.[112] Tyropanoic acid exhibits a strong XB interaction (average ΔE_{ZPE} = -30.56 kcal mol^{-1}) as well as significant activation of the C-I bond (average Δd(C-I) = +0.191 Å). However, steric interactions between its bulky substituents and the Dio active site may prevent deiodination.

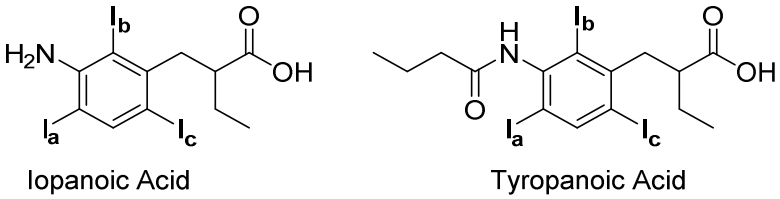

Figure 9. Structures of iopanoic acid and tyropanoic acid.

Br—Se XB interactions with $MeSe^-$ were modeled for a set of four PBDEs used by Roberts et. al.[45] and 18 OH-BDEs in Yu et. al. (Figure 10, Appendix A).[114] XB complexes are designated by the ring position at which XB takes place (*o*, *m*, or *p*) using a prime for interactions to the ring opposite the hydroxyl group. For example, for XB-*o*'-3a-OH-BDE-7, XB occurs at the *ortho* position of 3a-OH-BDE-7 on the ring opposite the hydroxyl group. XB complexes with $MeSe^-$ were calculated for all possible interactions of selenium with each unique bromine. In general, XB interactions for the PBDEs and OH-BDEs were less favorable than the TH derivatives (average ΔE_{ZPE} = -18.5 kcal mol^{-1} vs. -27.6 kcal mol^{-1}). In addition, the C-Br bonds of the PBDEs/OH-BDEs are not activated as strongly as for THs (average Δd(C-Br) = +0.15 Å; average Δd(C-I) = +0.17 Å). As the Se—Br distance decreases due to a stronger interaction, the C-Br bond lengthens resulting in activation of the bond (Figures 11A and 11B). Interactions at the *ortho* and *meta* positions more strongly activate the C-Br bond compared to the *para* position. This activation corresponds to increased donation of the Se lp orbital into the C-Br* acceptor fragment consistent with larger $\Delta E_{D\rightarrow A}$ values (Figures 11C and 11D). In general, higher-order brominated compounds exhibit shorter Se—Br distances and increased donation of the Se lp, with the decabrominated BDE-209 being a notable exception (Figures 11B and 11D). These results are consistent with the trend in C-X bond strength (C-Br > C-I)[110] and the absence of debrominated products in the studies of Dio2 inhibition by PBDEs.[45] In a few cases, the XB interaction to an *ortho* Br with an *ortho* OH on the opposite ring led to highly activated C-Br bonds (e.g., XB-o'-6-OH-BDE-82: Δd(C-Br) = +0.377 Å; ΔE_{ZPE} = -21.84 kcal mol^{-1}). The proximity of the OH proton to Br in some OH-BDEs (such as

3a-OH-BDE-154) allows for a hydrogen-bonding interaction that stabilizes the partial charge of the carbon end of the activated C-Br bond, favoring the right-hand resonance structure of the XB interaction (Figure 7B, Figure 9). Although these cases agree with the overall trends found for XB to PBDE/OH-PBDEs, they were omitted from the following analysis because their interactions were considered exaggerated by the gas-phase calculations.

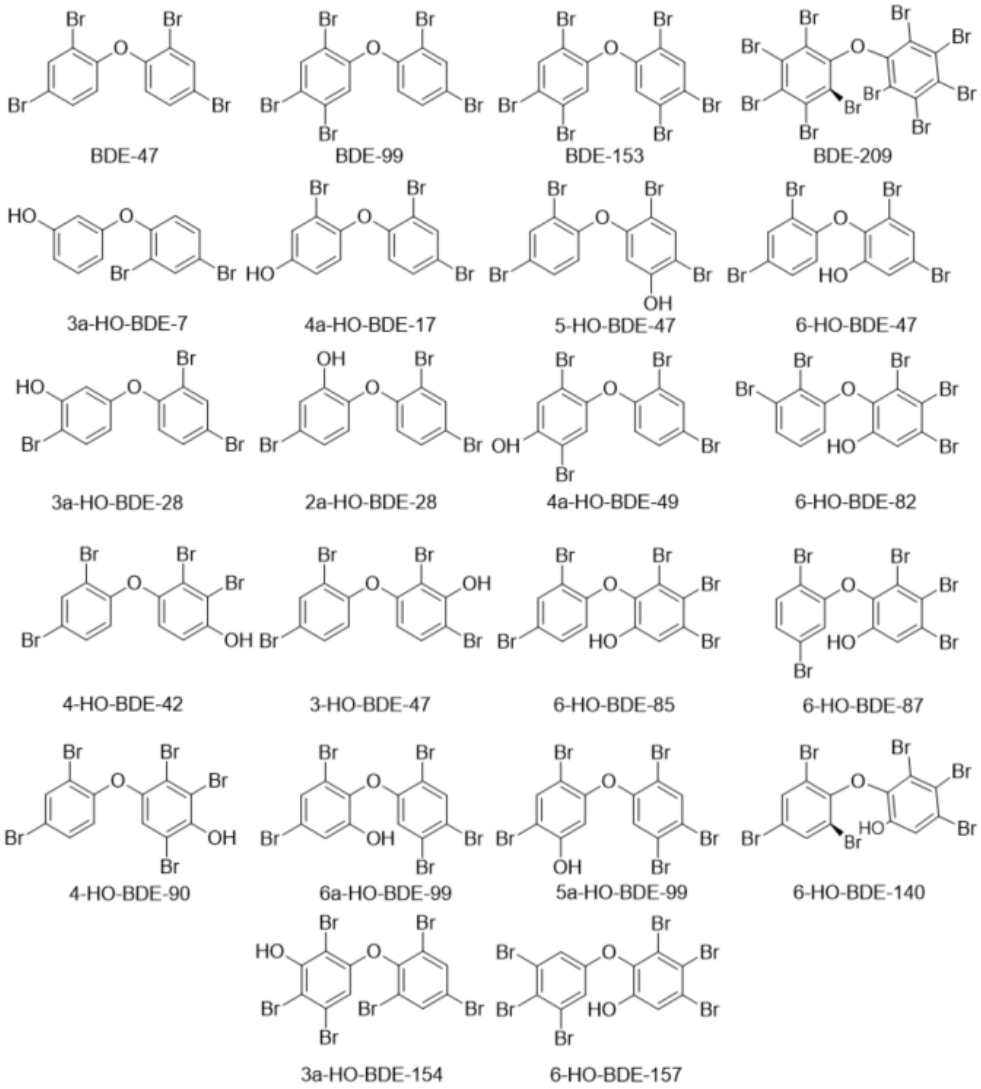

Figure 10. Structures of PBDEs/OH-BDEs used in this study.

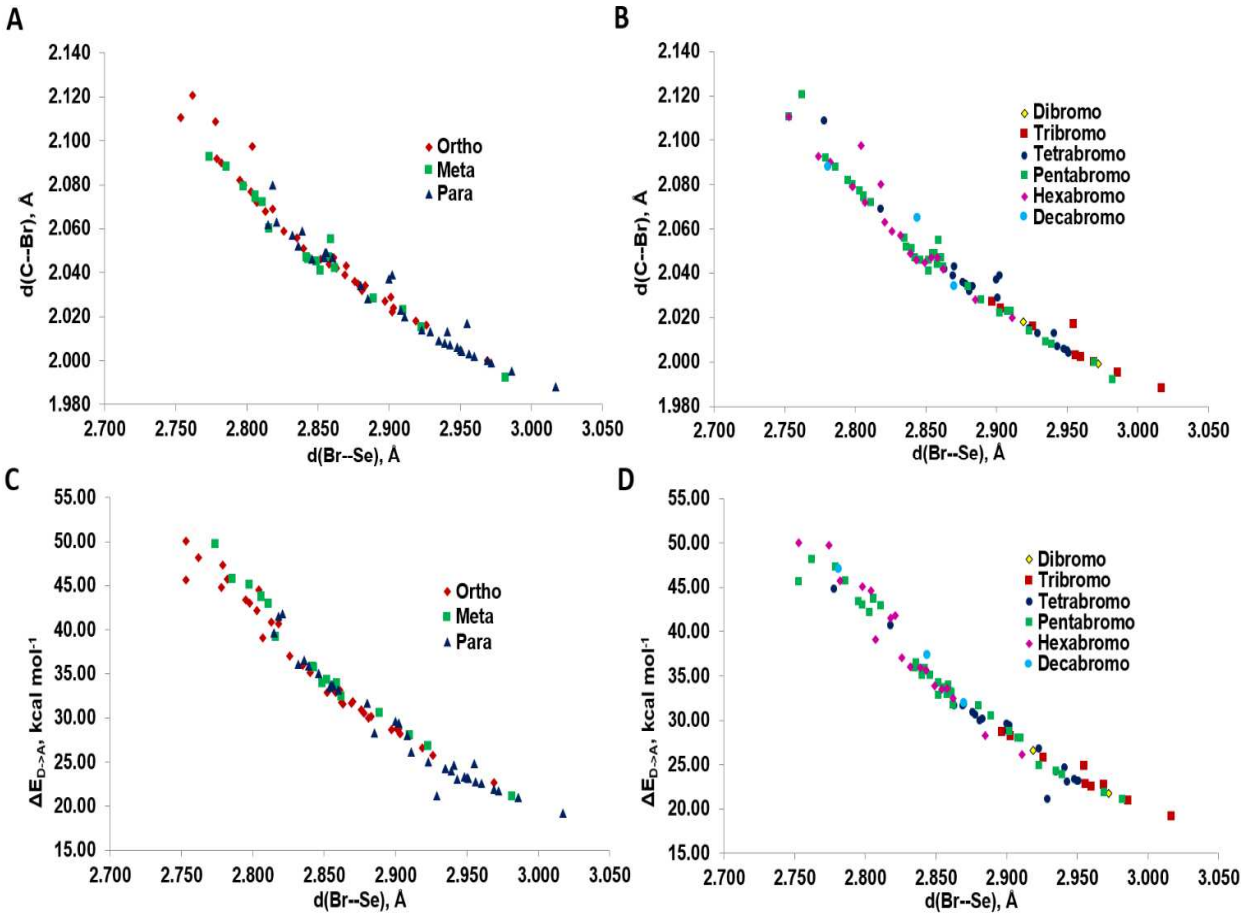

Figure 11. Comparison of bond distances by A) XB position and B) degree of bromination and donor-acceptor energy by C) XB position and D) degree of bromination.

In general, stronger C-Br bonds have a higher energy C-Br* acceptor MO and weaker XB interactions relative to C-I bonds. In a previous study of XB interactions between Me_2Se and PhX, the less favorable C-Br* MO of PhBr resulted in a smaller $\Delta E_{D\rightarrow A}$ than PhI (3.4 vs 7.3 kcal mol^{-1}).[37] The LUMOs of highly brominated PBDE/OH-PBDEs have C-Br* character (i.e., 6-HO-BDE-157, Figure 12), but those with the fewer bromines have π*-type LUMOs with higher energy unoccupied C-Br* LUMOs (i.e. 2-HO-BDE-28, 3-HO-BDE-47, Figure 12) resulting in less favorable XB interaction energies and less activation of the C-X bond in comparison to the aryliodine derivatives. Increased substitution with either -Br or -OH lowers the energy of the C-Br* MO, strengthening the XB interaction. Some highly

brominated PBDEs/OH-BDEs have comparable MO energies to the THs and therefore similar XB interaction energies (e.g. XB-*o*-3a-HO-BDE-154, ε_{LUMO} = -0.05824; ΔE_{ZPE} = -25.46 kcal mol^{-1}).

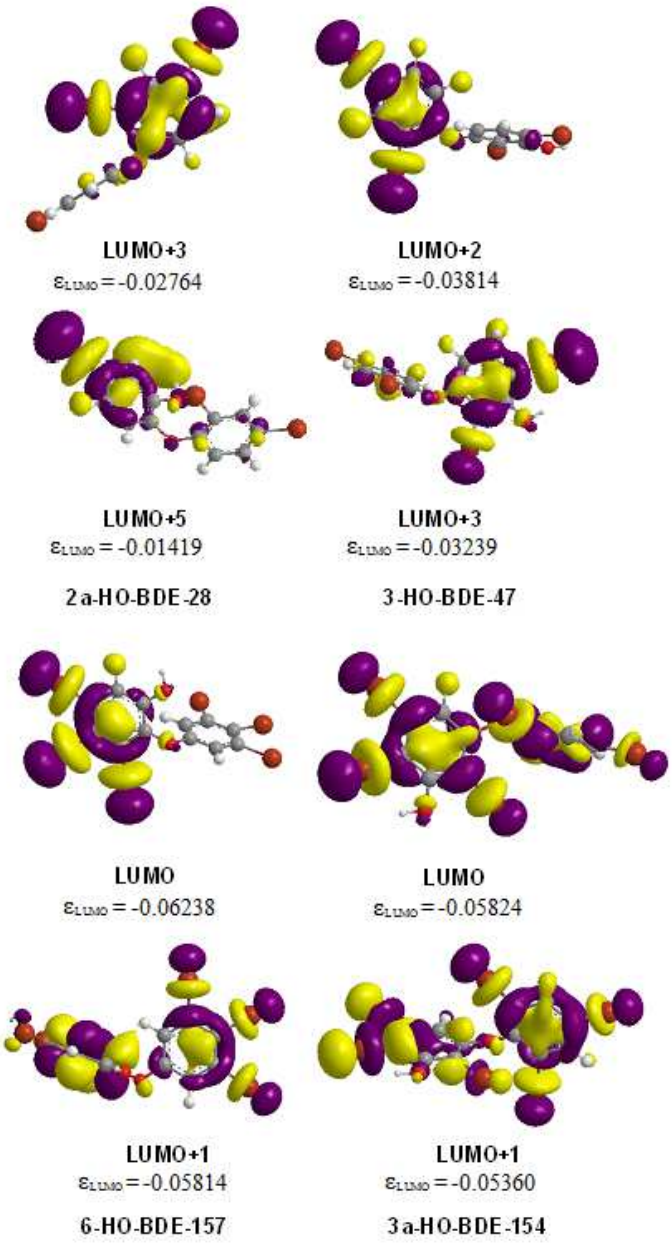

Figure 12. LUMO orbitals containing the lowest energy and the next-lowest energy for 2a-HO-BDE-28 (4 Brs), 3-HO-BDE-47 (4 Brs), 6-HO-BDE-157 (6 Brs), and 3a-HO-BDE-154 (6 Brs).

The XB interactions for the PBDEs/OH-BDEs at each position of the phenylic rings (*ortho, meta, para*) with $MeSe^-$ were also compared in terms of activation of the C-X bond and the overall energy in terms of ΔE_{ZPE}. XB interactions with *para* positions are generally clustered at low ΔE_{ZPE} with a weak activation of the C-Br bond (average Δd(C-Br) = +0.118 Å, Figure 13). *Ortho*- and *meta*- XB interactions tend to have more activated C-Br bonds (average Δd(C-Br) = +0.17 Å and +0.15 Å, respectively), albeit over a similar energy range as at the *para* position. For example, in 3-HO-BDE-47, the C-Br bonds are more activated at the *ortho* positions (average Δd(C-Br) = +0.151 Å) relative to *para* (average Δd(C-Br) = +0.110 Å). These results are consistent with the donor-acceptor energies. The favorability for XB in *ortho*/*meta* positions in PBDEs/OH-BDEs is consistent with the conserved *ortho*/*meta* iodination of THs. These important biomolecules may have adopted this regiospecificity due to the higher activation of C-I bonds at these positions. Highly active PBDEs/OH-BDEs are likely those whose structural similarity allows them to mimic the binding of THs to various proteins.

The clustering observed in Figure 13 is due to the additional effect of higher order substitution in the PBDEs/OH-BDEs. The C-Br bonds tend to be more activated and XB generally more favorable as the number of electron-withdrawing substituents increases. Many of the penta- and hexabrominated compounds have ΔE_{ZPE} and Δd(C-X) values similar to the TH derivatives, consistent with the potential for highly substituted PBDEs to undergo debromination as suggested in fish studies.[96,115] For example, in decabrominated BDE-209, ΔE_{ZPE} for XB interactions at all sites is favorable by more than -26.00 kcal mol^{-1} in agreement with a study showing debromination at each site.[115] However, its C-Br bonds are less activated than expected compared to the penta- and hexabrominated compounds, considering its more favorable ΔE_{ZPE}. This discrepancy is the result of the C-Br* character being delocalized over all C-Br bonds in the LUMO. In addition, a study of THRβ (which is involved in binding T_3) showed that increasingly brominated PBDEs/OH-BDEs caused a steady increase in overall inhibition, a trend similar to our computational results albeit for different types of XB interactions.[114]

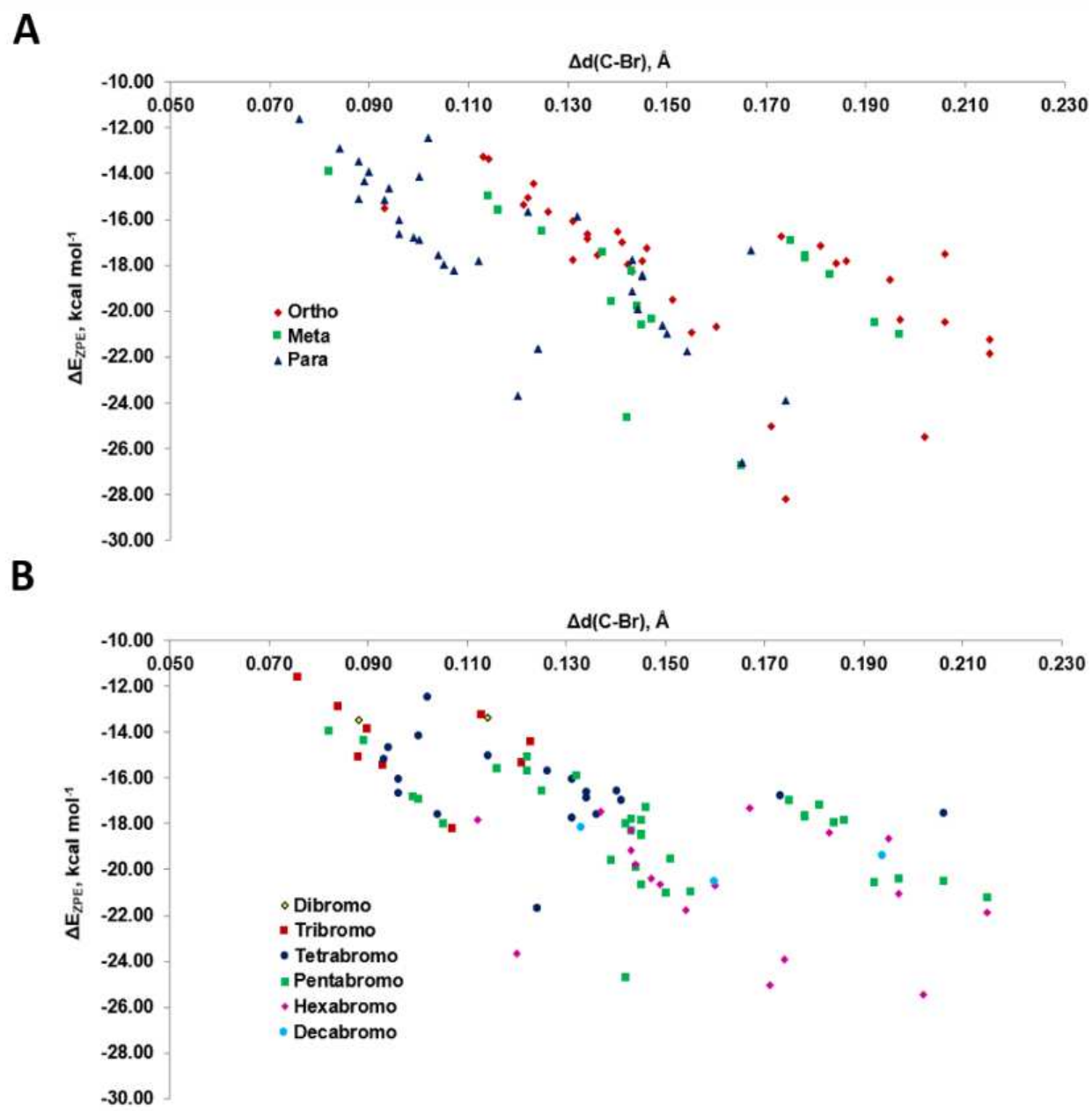

Figure 13. Comparison of the activation of C-Br with respect to ΔE_{ZPE} in the PBDEs/OH-BDEs by A) XB location; B) degree of bromination.

The addition of hydroxyl groups to OH-BDEs may enhance their affinity for Dio. XB strength and activation of C-Br bond for OH-BDEs varies depending on the proximity of the hydroxyl group to the site of XB and the identity of the compound. An adjacent hydroxyl group can stabilize the XB

interactions on some of the PBDEs/OH-BDEs (Figure 14). For example, XB at the para position of OH-BDE-154 has a more favorable interaction (XB-*p*-OH-BDE-154: ΔE_{ZPE}=-23.90 kcal mol^{-1}) than at the meta position (XB-*m*-OH-BDE-154: ΔE_{ZPE} = -19.79 kcal mol^{-1}) even though interactions to para XB are generally weak. Additionally, both XB-*p*-5a-OH-BDE-99 and XB-*p*-6a-OH-BDE-99 have hydroxyl groups on the same ring as the *para*-XB interaction, but in the former molecule, the adjacent hydroxyl group activates the C-Br more (+0.122 Å vs. +0.105 Å) near the hydroxyl group (Figure 14). However, XB-*p*-6a-OH-BDE-99 has a more favorable XB interaction (ΔE_{ZPE} = -17.97 kcal mol^{-1}) than XB-*p*-5a-OH-BDE-99 (ΔE_{ZPE} = -15.65 kcal mol^{-1}). Despite XB-*p*-5a-OH-BDE-99 having a neighboring OH group to the XB site, the DFT optimized structure has the OH proton facing away, preventing stabilization of the partial charge of the carbon within the C-Br bond, leading to a less favorable XB interaction. 4-OH-BDE-90 appears to follow the opposite trend: its most favorable interaction is next to a hydroxyl group (XB-*m*-4-OH-BDE-90, with ΔE_{ZPE} = -24.67 kcal mol^{-1}) however activation of C-Br is highest at XB-*o*-4-OH-BDE-90 (+0.197 Å). In contrast for 3-OH-BDE-47, the most favorable XB reaction occurs adjacent to the hydroxyl group and activates the C-Br bond the most (ΔE_{ZPE} = -22.63 kcal mol^{-1}, Δd(C-Br) = +0.167 Å). In general, the most favorable interactions in these compounds may result from interactions to a halogen adjacent to a hydroxyl group flanked by another halogen. Similarly, interactions with OH-BDEs were favored when the hydroxyl group was nested between two bromine groups in in silico sulfotransferase docking simulations of SULT1A1. OH-BDEs may have adopted this pattern to mimic the structure of TH substrates, which could explain the higher levels of toxicity and stronger XBs relative to PBDEs with no OH groups.

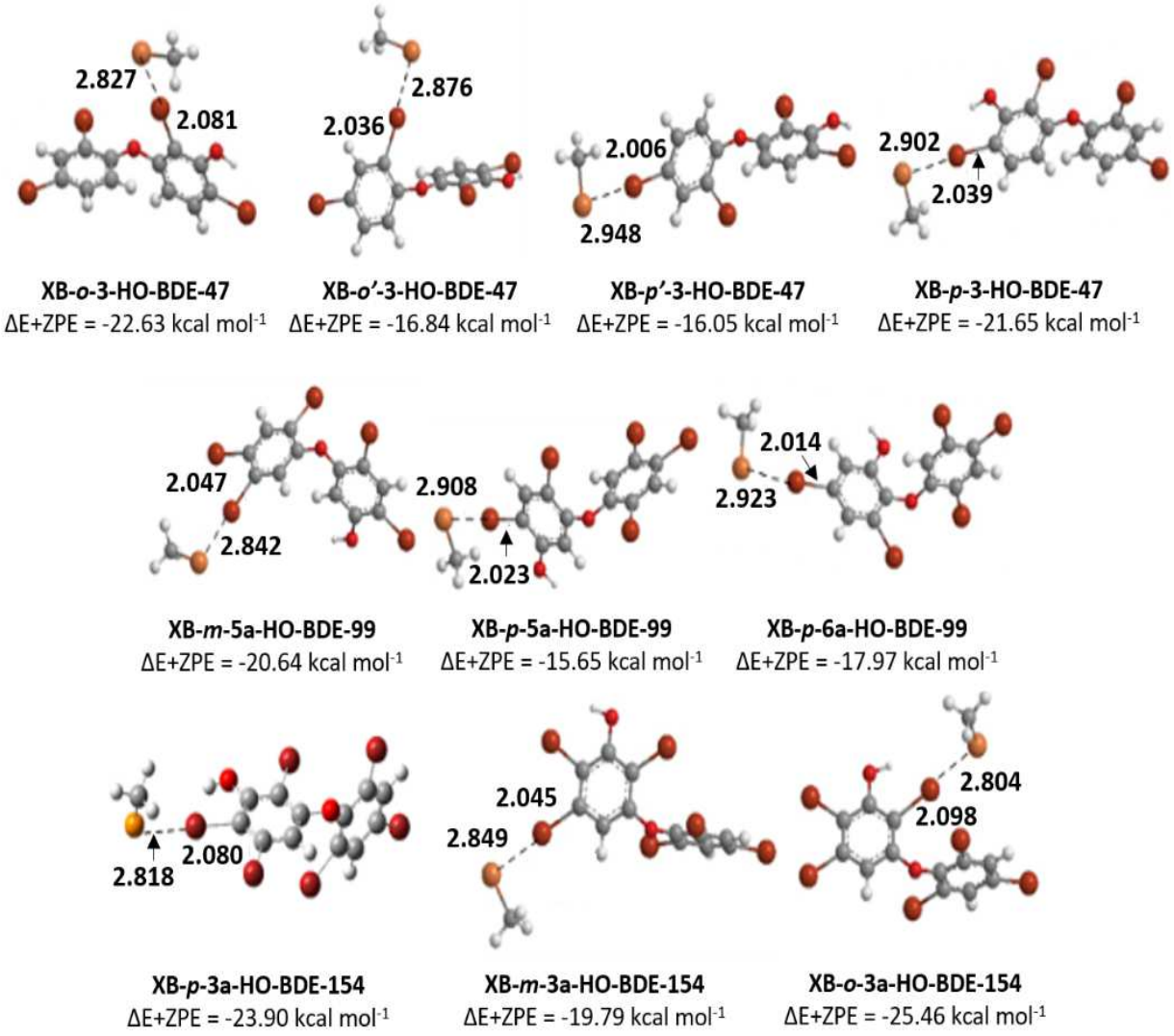

Figure 14. DFT optimized structures of selected compounds, with their corresponding ΔE_{ZPE} values.

The trends found for PBDEs are consistent with experimental observations of inhibition of TH pathways by Roberts et al.,[45] who compared the inhibition of Dio2 with several PBDEs and OH-BDEs. For these compounds, there is no noticeable effect on deiodination of T_4 at the low-nM range expected physiologically for BDE-99 and 5'-OH-BDE-99. Significantly higher concentrations (1000-5000 nM) were needed for Dio2 inhibition as the brominated compounds have less favorable XB interactions compared to the THs. 3-OH-BDE-47 (4 Brs, ΔE_{ZPE} = -22.63 kcal mol^{-1}) was the best inhibitor and the

only OH-BDE that exhibits short-term inhibition (1 hr) at a reasonably low concentration (1000 nM). Neither BDE-47 (4 Brs, ΔE_{ZPE} = -17.54 kcal mol^{-1}) nor 6-OH-BDE-47 (4 Brs, ΔE_{ZPE} = -17.57 kcal mol^{-1}) were suitable inhibitors of Dio2. Neither compound exhibited inhibition shorter than 6 hours, and 6-OH-BDE-47 exhibited only slight inhibition (approximately 20%) at 5000 nM after 12 hours. However, 6-OH-BDE-47 inhibits transthyretin (TTR) a known TH transport protein. This suggests that different substitutions will be effective in inhibiting different pathways.[116] Our results are comparable with the findings of Roberts et al., as each of the PBDEs/OH-BDEs used in their Dio inhibition study were modelled by us in the small DFT models. In DFT, the XB interaction for 3-OH-BDE-47 was more favorable than the other compounds by ~5 kcal mol^{-1}. Despite the higher level of bromination of 5'-OH-BDE-99 (5 Brs) which is more effective at inhibiting Dio1,[117,118] the structural similarity of 3-OH-BDE-47 to TH derivatives may contribute to its favorable XB interaction with Dio2. In addition, these results suggest that either the threshold that separates XB interaction from nucleophilic dehalogenation is not exceeded (i.e. ΔE_{ZPE} values from the set of OH-BDEs from Roberts et al.[45] are less than -23 kcal mol^{-1}) with this set of OH-BDEs or that deiodination is governed by other interactions with the Dio active site.

2.3 Conclusions

Modeling of XB interactions of THs, contrast agents and PBDEs using DFT provides insight into the competitive inhibition of TH processes by xenobiotics and how they may disrupt thyroid pathways. In comparison to THs, PBDEs and OH-BDEs form less favorable XB interactions with $MeSe^-$, both in terms of their interaction energies and the activation of the C-Br bond, suggesting that PBDEs/OH-BDEs may competitively bind to the active site to prevent the THs from being deiodinated. Overall, XB interactions tend to be most favorable at the *ortho* and *meta* positions relative to the ether group, and weaker at the *para* position. The lower affinity at the *para* position may shed light on why THs are only *ortho*- and *meta*- substituted suggesting a structure-activity relationship that may be targeted for drug design. Substitution of additional electron withdrawing groups in both THs and PBDEs enhance XB interactions due to stabilization of the LUMO. The fact that weakly interacting TH derivatives also do not

undergo deiodination may suggest a threshold for the Se—X interaction strength that must be exceeded to convert the XB interaction to a nucleophilic attack. Interactions with the residues surrounding the selenocysteine (Sec170) of Dio will also be a factor in the ability of THs and PBDEs/OH-BDEs to interact with and either undergo dehalogenation or block the active site. Full modeling of XB interactions to the active site of Dio are underway to determine the role of active site residues in selectivity.

2.4 Computational Methods

DFT optimized geometries of the selected compounds were calculated using Gaussian 09[57] using the hybrid exchange correlation functional mPW1PW91[119] paired with a triple-ξ basis set for the heavy atoms (TZVP).[120] The relativistic effective core potential basis sets of Hurley et. al.[121] and Wadt and Hay[122] were used for selenium and the halogens, respectively, and augmented with polarization and diffuse functions. Optimized structures were confirmed as minima on the potential energy surface by inspection of their vibrational frequencies. Donor-acceptor interactions were calculated using NBO 3.0[55] as implemented in Gaussian 09 to quantify the XB interaction in terms of the MO model.

CHAPTER 3

HALOGEN BONDING INTERACTIONS OF POLYCHLORINATED BIPHENYLS AND THE POTENTIAL FOR THYROID DISRUPTION[b]

3.1 Introduction

Polychlorinated biphenyls (PCBs) are a class of industrial flame retardants with high chemical stability.[123,124] Runoff of these persistent organic pollutants is of concern because they do not readily breakdown in the environment and bioaccumulate in various organisms.[124–126] Pollution by microplastics may contribute to contamination by PCBs and other organohalogen compounds.[127,128] PCBs are well-known endocrine disruptors that may interfere with thyroid hormone (TH) homeostasis.[129–132] Exposure to PCBs can cause negative long-term neurodevelopmental effects and cognitive deficits,[133–135] including lower motor activity,[136–138] autism,[139,140] and ADHD.[141,142] Although many formulations of PCBs ceased production in the late 1970s, they still contaminate many urban areas.[143–146]

PCBs are classified as dioxin-like (no *ortho* chlorines) or non-dioxin-like (one or more *ortho* chlorines) (Figure 15).[147–149] The former have been considered structurally similar to the toxic polychlorinated dibenzodioxins (PCDDs, i.e. 2,3,7,8-tetrachlorodibenzodioxin (TCDD), Figure 15), which are agonists to the aryl hydrocarbon receptor (AhR).[150] Non-dioxin-like PCBs (one or more *ortho* chlorine), on the other hand, are neurotoxic at much higher concentrations[151] and inhibit transthyretin (TTR), a transport protein for thyroid hormones.[152] PCBs do not readily inhibit thsyroxine-binding globulin (TBG), but certain hydroxylated PCBs (OH-PCBs) have strong affinities for both TTR and TBG[153–155] and inhibit TH sulfation.[156,157]

[b] This chapter was adapted from an article in *Chem Eur. J.* For the full citation, see ref. 40.

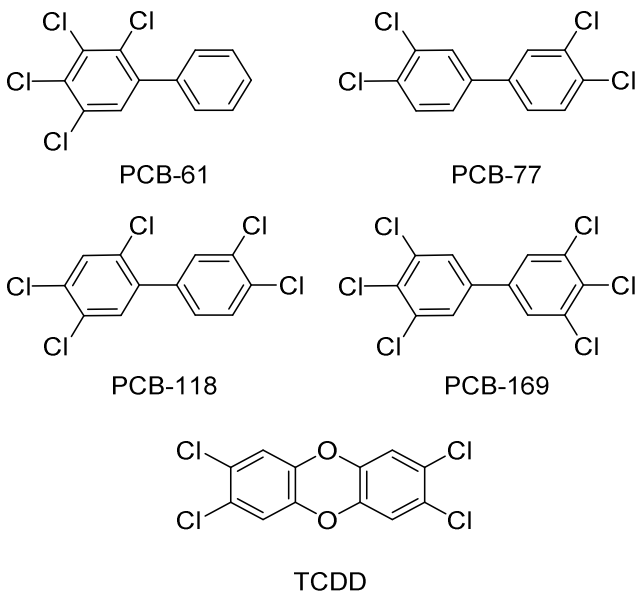

Figure 15. Selected sample structures of PCBs and TCDD.

Iodothyronine deiodinases (Dio) are thioredoxin-fold selenoproteins that regulate TH homeostasis.[2,5,78,158] For example, deiodination of the prohormone thyroxine (T_4) to triiodothyronine (T_3) is an activating pathway. Disruption of thyroid hormone homeostasis leads to side effects including hypothyroidism, cardiovascular disease, and structural abnormalities.[39,82,86] Dio proteins play an important role in early developmental stages[108] and a recent study suggests that PCBs may inhibit their activity in infants.[159] PCBs, dioxins and other organochlorine compounds have also been shown to inhibit Dio in various organisms, such as rats,[43,160,161] fish,[162] birds,[163] chickens,[164,165] and eels.[166] However, other studies show inconsistent relationships between organochlorine levels and Dio activity.[44,160,167–171]

Deiodination is facilitated by a conserved selenocysteine (Sec) residue at the Dio active site.[35] Bayse et. al[37] have linked halogen bonding (XB) to the deiodination mechanism of THs with support from other groups through experimental studies using Dio mimics,[172,173] computational modeling and the X-ray structure of Dio3 catalytic region.[35] XB interactions have numerous applications to drug design and crystal engineering[103,174–176] and are often described as an electrostatic interaction with a "σ-hole" along

the bond axis of the halogen.[102,104,177,178] However, several authors have noted that this popular model de-emphasizes significant contributions such as covalency and dispersion to the XB interaction.[179–187] Alternatively, XB can be described as the donation of electron density from the lone pair of a donor (such as S or Se) to the antibonding $\sigma_{R\text{-}X}$* orbital (where X = I, Br, or Cl) of the acceptor (Figure 16).[37,39,105,106,179,188,189] Overall strength of the XB donor-acceptor interaction ($\Delta E_{D\rightarrow A}$) is inversely related to the strength of the C-X bond, due to the lower lying $\sigma_{R\text{-}X}$* orbitals of weaker bonds, such as those in heavier halogenated organics.

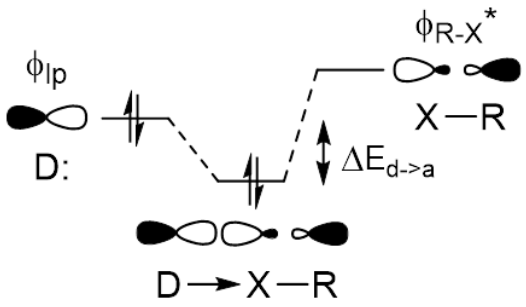

Figure 16. XB interactions as described by the molecular orbital model.

XB has been proposed as a possible means of inhibition of Dio activity by halogenated organic compounds.[39,179] PCBs, for example, could block deiodination through an XB interaction with the selenium center of the active site Sec. In a previous study, we compared the strength of XB interactions between a small model of the Dio active site ($SeMe^-$) and a series of THs and potential organohalogen inhibitors: polybrominated diphenyl ethers (PBDEs) and their hydroxylated metabolites (OH-BDEs).[39] The iodinated THs had stronger XB interactions than the PBDEs by approximately 10 kcal mol^{-1}, consistent with more favorable XB interactions in larger halogens (I > Br > Cl).[104] In this study, trends in the strength of Cl—Se interactions with the $SeMe^-$ model of Dio are examined using density functional

theory (DFT) in terms of the potential for PCBs to inhibit Dio mediation of TH homeostasis. Additionally, the conformational flexibility of PCBs is discussed in terms of the inhibition of a wider range of TH-related proteins. Both the XB interaction strength and the ability of the PCB to adapt to the protein active site are likely key factors in the toxicity of individual compounds.

3.2 Results and Discussion

Cl—Se XB interactions with $SeMe^-$ were modelled at the DFT(M06-2X)/TZVP+ level for all 209 possible PCB congeners at each unique ring position (*ortho, meta, para*) to examine trends in terms of Natural Bond Orbital (NBO) donor-acceptor energies ($\Delta E_{D\rightarrow A}$)[55] and zero-point energy corrected interaction energies ($\Delta E_{ZPE}=E_{ZPE}(MeSe^-_{(PCB)})-E_{ZPE}(MeSe^-)-E_{ZPE}(PCB)$) (Appendix B and C). XB complexes are labeled according to the position where XB takes place (i.e. 2, 2', etc.). For example, XB-3-PCB-77 designates the complex with the XB interaction at the 3-position on PCB-77 (3,3',4,4'-Cl).

PCBs generally have weaker X—Se interactions (ΔE_{ZPE} = -1.0 - -16.0 kcal mol^{-1}) compared to PBDEs (ΔE_{ZPE} = -11.5 - -28.2 kcal mol^{-1}) and THs (ΔE_{ZPE} = -21.0 - -33.0 kcal mol^{-1}),[39] consistent with less favorable XB with decreasing size of the halogen. Similar to PBDEs and THs, the interaction strength increases with increased chlorination of the PCB (i.e. ΔE_{ZPE} = -2.28 kcal mol^{-1} for XB-4-PCB-3, ΔE_{ZPE} = -11.62 kcal mol^{-1} for XB-2-PCB-209 (2,2',3,3',4,4',5,5',6,6'-Cl).) Based upon the lack of deiodination for 3-T_1,[39] which has the weakest XB interaction (ΔE_{ZPE} = -21.42 kcal mol^{-1})[39] of the series of THs, we have proposed that the strength of the XB interaction must exceed a threshold in order for nucleophilic dehalogenation to be favorable.[39] Because the aryl chlorides' XB interaction strengths are generally lower than the THs, PCBs are unlikely to meet the energy threshold required to undergo dehalogenation, and instead reversibly bind to the active site to block TH activation.

Overlap between the Se lone pair and the high energy C-Cl* orbital is less favorable than donation to the lower energy C-Br* and C-I* orbitals (average $\varepsilon_{LUMO} \approx$ 1.5241 eV for PCBs, -1.0882 eV for PBDEs, -1.9054 eV for THs).[39] Reduced donation of the Se lp orbital into the C-Cl* orbital fragment leads to smaller donor-acceptor energies ($\Delta E_{D\rightarrow A}$ ranges from 1.0 to 10.0 kcal mol^{-1} for PCBs (Figure 17)

vs. 20.0-50.0 kcal mol^{-1} for PBDEs and 40.0-55.0 kcal mol^{-1} for THs).[39] Similar to results for PBDEs,[39] the higher-substituted PCBs exhibit shorter Cl—Se distances and increased donation from the Se lp fragment (Figure 17). However, because C-Cl bonds are weak XB partners, Cl—Se distances in PCBs are generally longer than Br—Se distances observed for PBDEs and I—Se interactions of THs (average *d*(Cl—Se) = 3.285 Å for PCBs, *d*(Br—Se) = 2.830 Å for PBDEs, and *d*(I—Se) = 2.961 Å for THs).[39]

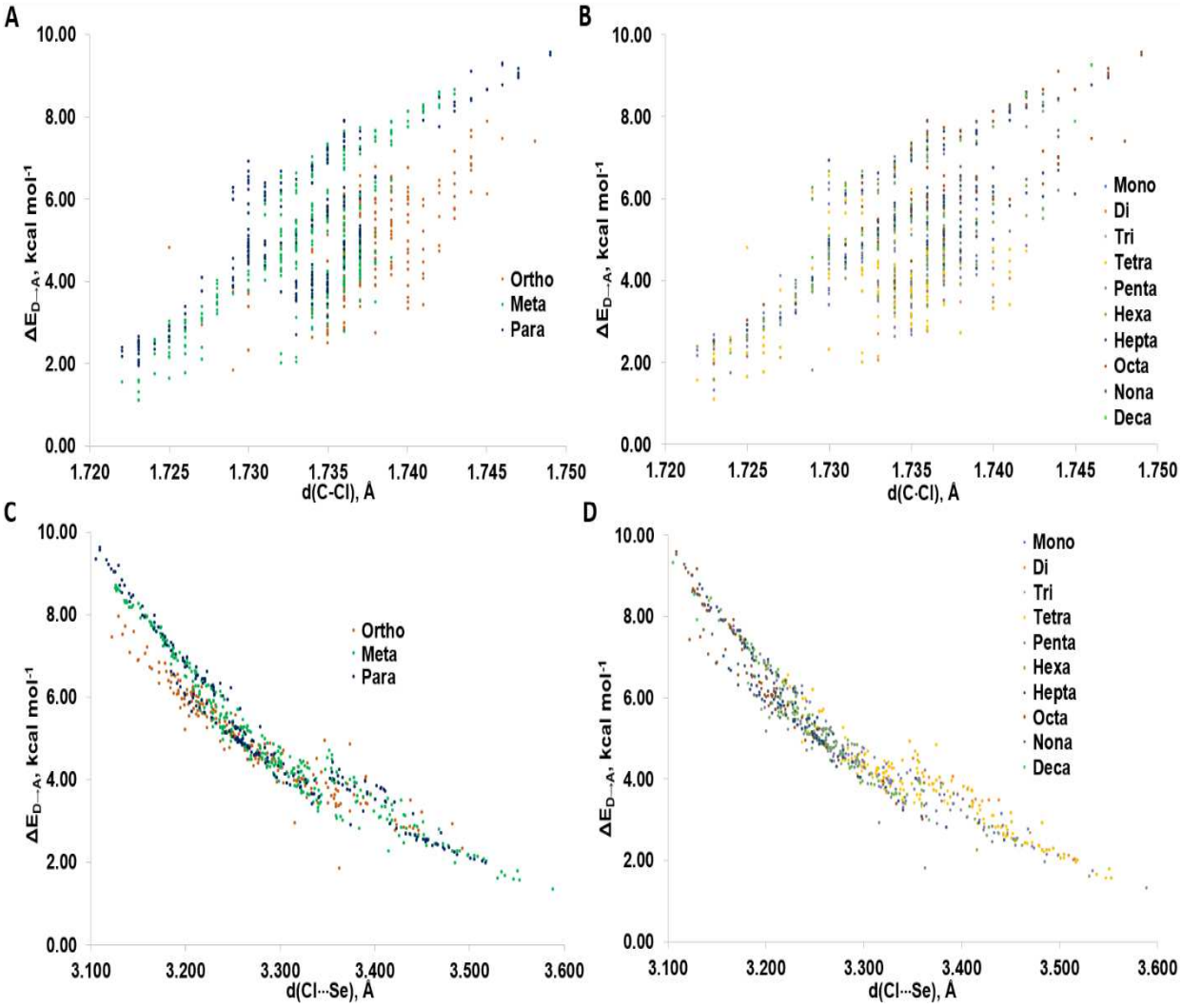

Figure 17. Comparison of donor-acceptor energies vs. *d*(C-Cl) by A) XB position and B) degree of bromination and donor-acceptor energy and donor-acceptor energies vs. *d*(Cl-Se) by C) XB position and D) degree of bromination.

The donation of electron density into the R-X* MO in an XB interaction lengthens and activates the R-X bond for nucleophilic attack in proportion to the strength of the XB interaction. Average XB interaction strengths correlate with the weak activation of the C-Cl bond (Δd(C-Cl)= +0.003 Å, $\Delta E_{D\rightarrow A}$ = 7.35 kcal mol^{-1}, Figures 17 and 18A) compared to the PBDEs (Δd(C-Br)= +0.150 Å, $\Delta E_{D\rightarrow A}$ = 39.14 kcal mol^{-1}) and THs (Δd(C-I)= +0.177 Å, $\Delta E_{D\rightarrow A}$ = 47.49 kcal mol^{-1}).[39] d(C-Cl) and d(Cl-Se) appear to be independent of XB position, but increased halogenation generally leads to increased C-Cl bond lengths (Figure 17). For example, XB to PCB-205 (8 Cls) has a greater activation of C-Cl than to PCB-61 (4 Cls) (i.e., Δd(C-Cl) = +0.029 for XB-4-PCB-205 and +0.012 Å for XB-4-PCB-61 respectively, Figure 18).

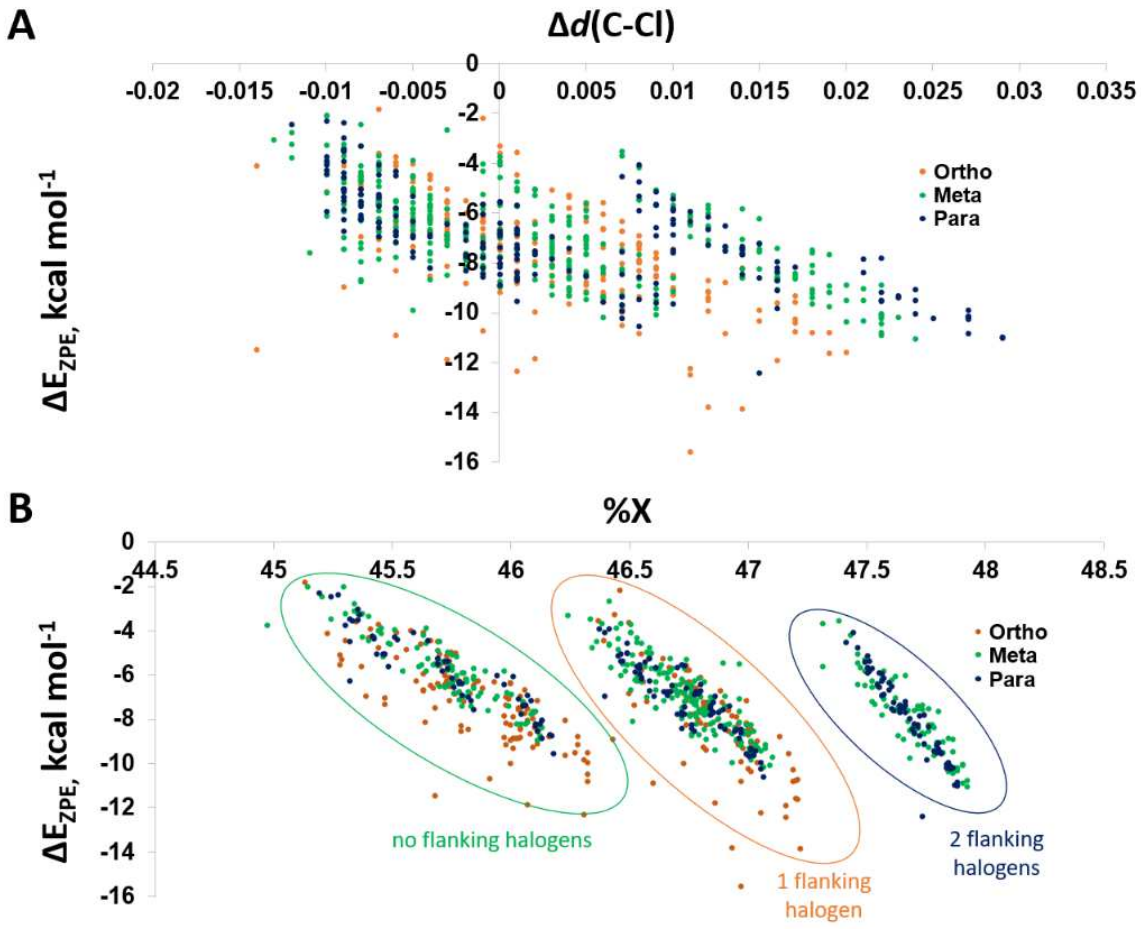

Figure 18. Comparison of zero-point energy corrected interaction energies (ΔE_{ZPE}) to A) the activation of the C-Cl bond (Δd(C-Cl)) by XB position; B) percent contribution of X (%X) by XB position.

NBO analysis was used to determine the weighting of $\sigma_{R\text{-}X}$* towards X (%X). %X measures the donation of X into the C-X σ* antibonding orbital, which enhances overlap with the donor lone pair. Therefore, a higher %X should correspond to a stronger XB interaction.[179] The stronger XB interactions of brominated and iodinated aromatics correlate with the higher contribution of X to the $\sigma_{R\text{-}X}$*-type MOs (%X for aryl bromides = 50-55%; for aryl iodides = 55-65%).[179] In contrast, %X for PCBs range from approximately 45% to 48% (Appendix C), similar to other aryl chlorides (%X = 40-50%).[179] Additionally, although the acceptor $\sigma_{R\text{-}X}$* MO is generally the LUMO of heavier aryl halides, PCBs tend to have LUMOs with π* character due to the stronger C-Cl bonds with higher energy $\sigma_{R\text{-}Cl}$* MOs (Figure 19).

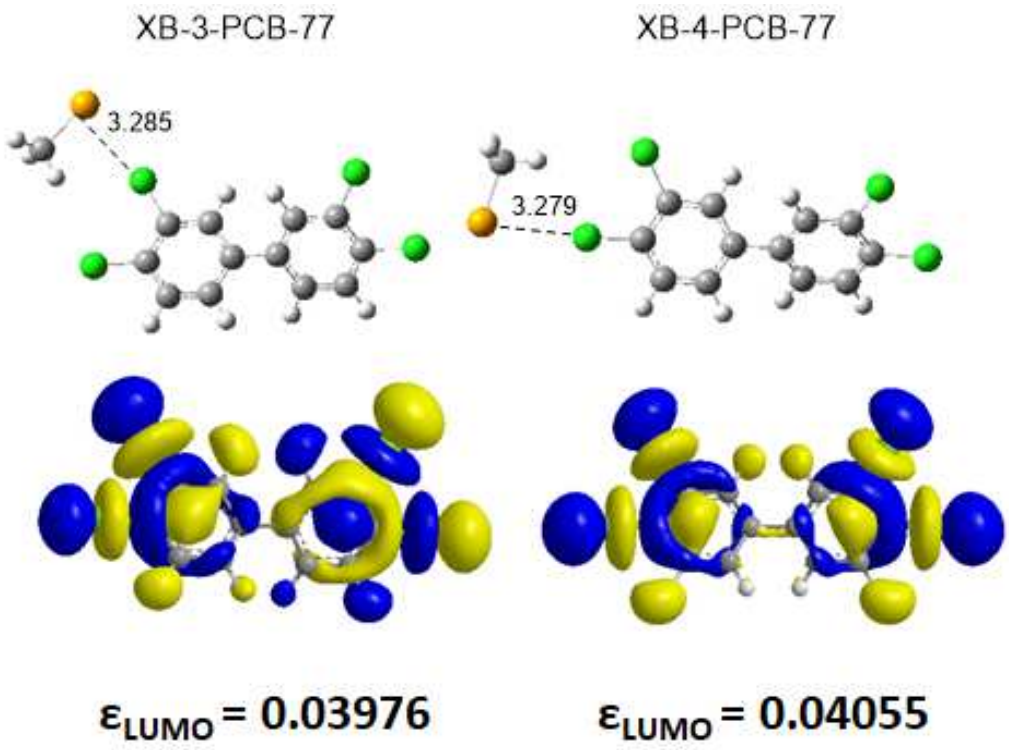

Figure 19. XB interactions at both the *meta* and *para* positions respectively, along with the LUMO orbitals containing the lowest and next-lowest energies for PCB-77. Distances are in Angstroms.

Cl—Se XB interactions are strengthened by the electron-withdrawing effect of the neighboring chlorines which stabilize $\sigma_{R\text{-}X}$* and increase their %X contribution.[179] The largest $\Delta E_{D\rightarrow A}$ are found for *meta* and *para* XB complexes that interact through a chlorine flanked by two other chlorines. The weaker donor-acceptor energies at the *ortho* position resulted in a number of cases where the interaction was so weak that no stable XB complexes could be found. In contrast, PBDEs have their largest $\Delta E_{D\rightarrow A}$ values primarily for *ortho* and *meta* XB interactions.[39] In terms of the interaction energy ΔE_{ZPE}, electrostatic interactions with the adjacent ring lead to slightly more favorable XB interactions at *ortho* positions (-7.62 kcal mol^{-1}) on average compared to *meta* and *para* (-6.84 and -7.01 kcal mol^{-1} respectively). ΔE_{ZPE} (Figure 18B) for *meta* and *para* XB interactions to chlorines with two adjacent halogens cluster at higher %X (average %X = 47.6 ± 0.3%) and shift toward lower overall ΔE_{ZPE} than PCBs with one (middle cluster, average %X = 46.8 ± 0.3% across all PCBs) or no neighboring halogens (leftmost cluster, average %X = 45.9 ± 0.4% (*ortho*) and 45.8 ± 0.4% (*meta* and *para*) respectively, Figure 18).

Experimental data on the disruption of Dio activity by PCBs is limited.[159,190,191] Coimbra et al. assessed Dio activity in tilapia upon exposure to Aroclor 1254, an industrial mixture containing PCB-77 ($\Delta E_{D\rightarrow A}$ = 4.49 and 5.28 for *meta* and *para* positions respectively). Dio3 activity increased in the brain over the course of 3 and 5 weeks, while hepatic Dio1 and brain Dio2 activity decreased.[191] Exposure to Aroclor 1254 caused an increase in plasma TH levels, which could be indicative of Dio inhibition. In a similar study, Morse et al. found that neither PCB-77 nor Aroclor 1254 had an effect on brain Dio2 activity in adult mice.[190] Analysis of a select group of PCBs on deiodinase activity in the cord blood in infants found a positive correlation between 2,4,5-substituted PCBs 118 (2,3',4,4',5-Cl), 138 (2,2',3,4,4',5'-Cl), 146 (2,2',3,4',5,5'-Cl), 153 (2,2',4,4',5,5'-Cl), 183 (2,2',3,4,4',5',6-Cl), and 187 (2,2',3,4',5,5',6) concentrations and the T_3/rT_3 ratio, suggesting a negative effect on Dio3 activity[159] consistent with stronger interactions to highly-halogenated PCBs (≥ 5 Cl). The C-Cl bond is most activated at the *meta* position of the 2,4,5 ring of PCB-118 and PCB-153 ($\Delta E_{D\rightarrow A}$ = 5.24 kcal mol^{-1} and 5.57 kcal mol^{-1}) while the most activated C-Cl bond for PCB-138 and PCB-183 is located at the *meta*

position opposite the 2,4,5 ring ($\Delta E_{D\rightarrow A}$ = 6.62 kcal mol^{-1} and 7.27 kcal mol^{-1}). Finally, the *ortho* C-Cl bonds opposite of the 2,4,5 ring in PCB-146 and PCB-187 are the most activated ($\Delta E_{D\rightarrow A}$ = 5.51 kcal mol^{-1} and 6.21 kcal mol^{-1}).

The position dependence of the XB donor-acceptor strengths suggests that PCBs with substitution patterns similar to the preferred TH substrate for a Dio paralog[192] may more effectively inhibit that Dio type. For example, Dio1 can deiodinate both inner and outer rings and has a high affinity for rT_3, while Dio2 and Dio3 are specific to outer ring deiodination (ORD, or *meta*-deiodination) and inner ring deiodination (IRD, or *ortho*-deiodination) and prefer T_4 and T_3 respectively (Figure 20). A PCB like PCB-80 (3,3',5,5'-Cl) with key interactions at a *meta* chlorine ($\Delta E_{D\rightarrow A}$ = 4.42 kcal mol^{-1}) may display better inhibition towards Dio2 (Figure 20).[192] Likewise, a PCB like PCB-54 (2,2',6,6'-Cl) which interacts only at an *ortho* chlorine ($\Delta E_{D\rightarrow A}$ = 3.62 kcal mol^{-1}) may suggest better inhibition towards Dio3 (Figure 20). A PCB like PCB-155 (2,2',4,4',6,6'-Cl) is most activated at the *ortho* position compared to the *para* position ($\Delta E_{D\rightarrow A}$ = 5.38 vs. 4.96 kcal mol^{-1}) and may preferentially target Dio3. A PCB like PCB-136 (2,2',3,3',6,6'-Cl) is more activated at 6-Cl ($\Delta E_{D\rightarrow A}$ = 4.63 kcal mol^{-1}, *ortho*) than at 3-Cl ($\Delta E_{D\rightarrow A}$ = 3.62 kcal mol^{-1}, *meta*) may also favor inhibition of Dio3. PCBs that display both *ortho* and *meta* chlorines but have the highest activation of C-Cl at the *para* position (i.e., PCB-128 (2,2',3,3',4,4'-Cl) ($\Delta E_{D\rightarrow A}$ = 6.72 kcal mol^{-1}) may either have a lesser effect or bind differently to Dio.

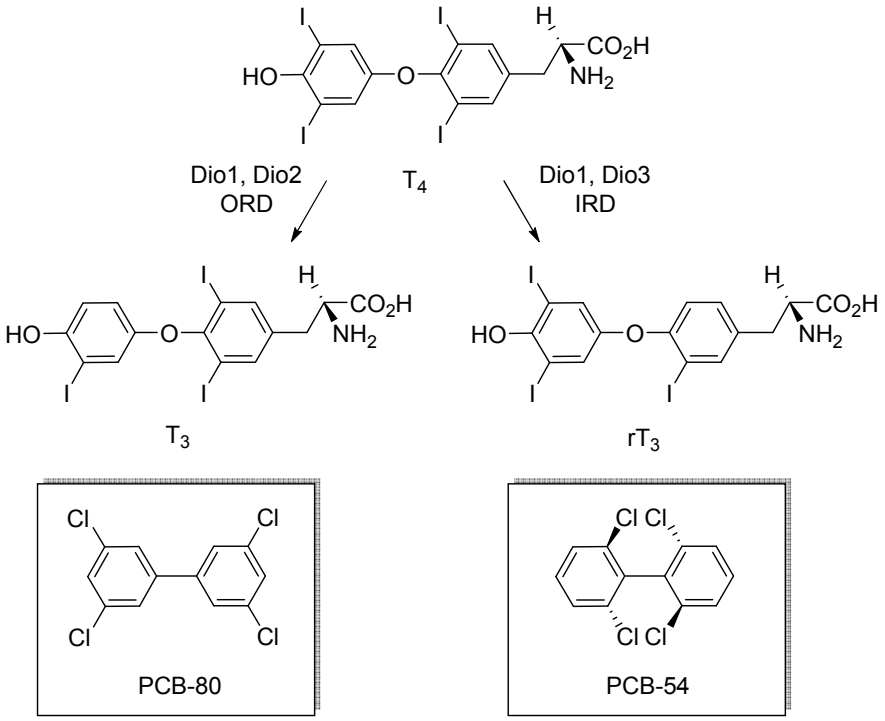

Figure 20. Pathways of TH inner ring and outer ring deiodination (IRD, ORD) and their byproducts, with PCBs that may specifically target Dio2 (PCB-80) and Dio3 (PCB-54) respectively.

While the ΔE_{ZPE} and $\Delta E_{D\rightarrow A}$ energies provide insight to the favorability of XB interactions with PCBs, many proteins require ligands to bind in a certain conformation for substrate recognition.[193,194] For example, different TH orientations were found within the active site(s) of TH-binding proteins from the crystallographic data obtained from the Protein Data Bank.[195] The large iodine atoms of THs cause some conformations to become unfavorable due to steric clashes with residues on the surface of proteins.[195,196] PCBs have been incorrectly assumed to have a coplanar structure (i.e., with an inter-ring dihedral of $\theta = 0°$) in analogy to the structure of TCDD. However, the optimized geometries of all PCBs are nonplanar[197] and X-ray crystal structures of TTR-PCB complexes show that the PCBs are not coplanar within the binding pocket (PDB IDs: 2G5U, 2G9K, 2GAB).[198] At the coplanar orientation ($\theta = 0°$), delocalization of the biphenyl π-electrons is maximized, but sterics between the *ortho* positions on the opposing rings contributes to a large barrier for twisting through this conformation.[199] In contrast, when the rings are

perpendicular (θ = 90°), steric interactions are minimized, but there is no delocalization between the phenyl rings. The slightly twisted structure of the unsubstituted biphenyl with two minima at θ = 40° and θ = 140°, separated by a larger barrier at 0° and a small one at θ = 90°, represents a balance between these steric and electronic factors (Figure 19).[199–201] The non-*ortho* PCBs have been shown to have a lower twist barrier at θ = 0° and a higher twist barrier at θ = 90° in the presence of explicit water.[197] The 2,2‘-PCBs have their lowest energy structure near θ = 80° where steric clashes between Cls on opposite rings is minimized (Figure 21). As the *ortho* positions become halogenated, the minima shift closer to θ = 90° up to 2,2‘,6,6‘-*ortho* PCBs which has a single minimum. Increased *ortho*-substitution also results in higher and steeper barriers for twisting through the coplanar conformation leading to less flexibility about the central C-C bond.

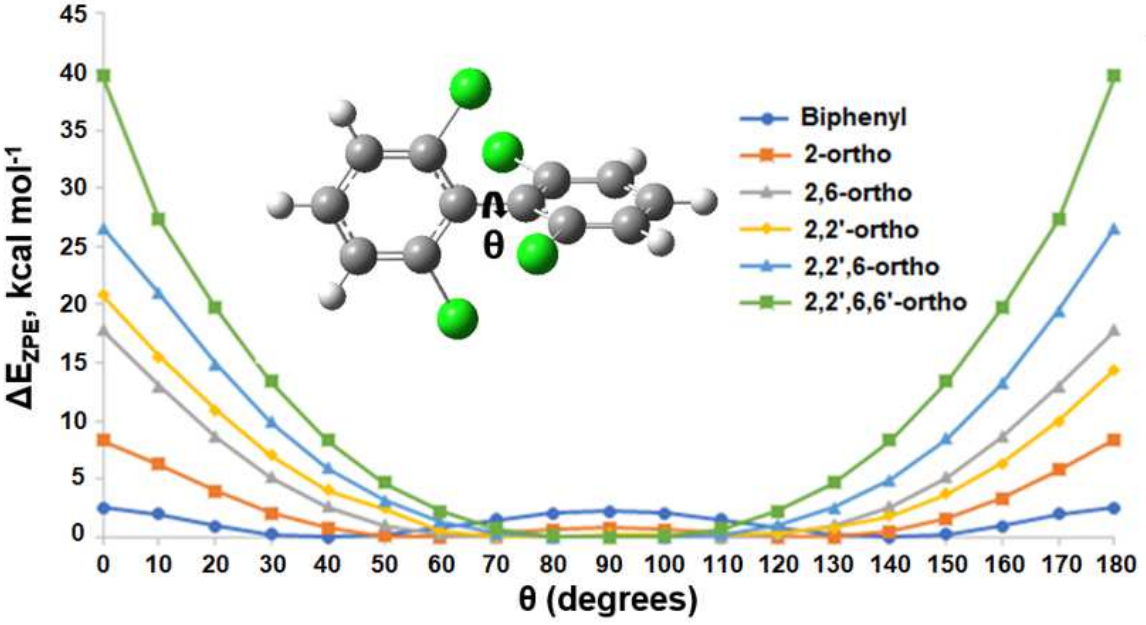

Figure 21. PES curves for the rotation around the central bond of PCBs with various *ortho*-substitution patterns.

Previous studies proposed a "buttressing" effect, where adding *meta* chlorines to *ortho*-chlorinated PCBs showed that the barrier for forcing coplanarity was increased, but only in cases where the *meta* addition is adjacent to an *ortho* chlorine.[202–204] The adjacent *meta* Cl repels the *ortho* Cl, forcing it out of the plane of the ring. The PES curves of PCB-10 (2,2'-Cl), PCB-24 (2,3,6-Cl), and PCB-27 (2,3',6-Cl) show the effect on the barrier for twisting at $\theta = 0°$ only increases by approximately 1.0 kcal mol^{-1}.[199,204] While some highly *ortho*-chlorinated PCBs like PCB-204 (2,2',3,4,4',5,6,6'-Cl, $\Delta E_{D\rightarrow A} = 6.04$ kcal mol^{-1}) and PCB-209 (2,2',3,3',4,4',5,5',6,6'-Cl, $\Delta E_{D\rightarrow A} = 7.94$ kcal mol^{-1}) have favorable XB interactions, the inflexibility of these compounds due to steric hinderance of the *ortho* chlorines may reduce their ability to bind to Dio or other TH-related proteins.

PCBs have been shown to disrupt other pathways, such as displacement of THs from transport proteins (i.e. TTR)[94,205] and inhibition of the sodium-iodide symporter (NIS),[206–208] which may account for the increase of THs in plasma. Chauhan et al.[138] determined the trends in the inhibition of a transport protein TTR for a series of PCBs. For PCBs without *ortho* chlorides, competitive binding to TTR for lightly chlorinated species is strongest in the order of PCB-38 (3,4,5-Cl) > PCB-14 (3,5-Cl) > PCB-39 (3,4',5-Cl) > PCB-35 (3,3',4-Cl) > PCB-11 (3,3'-Cl) > PCB-37 (3,4,4'-Cl) = PCB-15 (4,4'-Cl). Heavily chlorinated PCBs (≥ 4 Cl) inhibit TTR binding in the order of PCB-127 (3,3',4,5,5'-Cl) > PCB-80 (3,3',5,5'-Cl) > PCB-126 (3,3',4,4',5-Cl) > PCB-77 (3,3',4,4'-Cl). Although the Cl—Se XB interactions with the $SeMe^-$ Dio model are stronger than any XB interactions found with the TTR binding site,[209] the trends in XB strength should be similar. The trend within the lightly and heavily chlorinated PCBs track closely with the ability to inhibit TTR. For example, PCB-38 had the most favorable Cl—Se interaction ($\Delta E_{D\rightarrow A} = 6.22$ kcal mol^{-1}) while PCB-11 had the least favorable interaction ($\Delta E_{D\rightarrow A} = 2.06$ kcal mol^{-1}) of the lightly chlorinated series. PCB-127 contains the most favorable XB interaction ($\Delta E_{D\rightarrow A} = 6.50$ kcal mol^{-1}) and PCB-77 has the least favorable interaction ($\Delta E_{D\rightarrow A} = 2.20$ kcal mol^{-1}) for the most substituted series. Generally, *para* (4,4') PCBs had very low affinity for TTR, with the exception of highly substituted PCB-169 (3,3',4,4',5,5'-Cl),[138] despite the possibility of favorable XB interactions. For

example, PCB-126 is almost equal to PCB-127 ($\Delta E_{D\rightarrow A}$ = 6.43 kcal mol^{-1} vs 6.50 kcal mol^{-1}), but its TTR inhibition is over two orders of magnitude smaller. Substitution at both *para* positions may have a steric effect not reflected in our small model that prevents PCBs from accessing the TTR binding site.

In the *ortho*-only substituted PCBs, the order of inhibition strength towards TTR was PCB-19 (2,2',6-Cl) > PCB-4 (2,2'-Cl) = PCB-10 (2,6-Cl) >> PCB-1 (2-Cl) = PCB-54 (2,2',6,6'-Cl). Although the XB strengths for this series are comparable to the non-*ortho* PCBs, their activity is more than two orders of magnitude lower than the non-*ortho* PCBs due to the reduced flexibility of the *ortho* PCBs. The most substituted of this series, PCB-19 and PCB-54, have similar Cl—Se interactions ($\Delta E_{D\rightarrow A}$ = 3.90 and 3.62 kcal mol^{-1}, respectively), but PCB-19 is better able to inhibit TTR given its limited conformational flexibility relative to the more rigid PCB-54 (Figure 19). Overall, the inflexibility of *ortho*-substituted PCBs despite having potential XB interactions of similar strength to non-*ortho* PCBs could explain their lower toxicity.

3.3 Conclusions

Understanding the PCB interactions within the endocrine system could have significant pharmacological implications, such as the design of mimics that target TH-binding proteins. Modelling the Cl—Se XB interaction between the $SeMe^-$ model and PCBs provides insight on the potential inhibition of the iodothyronine deiodinases through competitive active site binding. PCBs have less favorable interactions than THs or organobromine PBDE inhibitors, in agreement with XB dependence on the size of the halogen (I > Br > Cl). PCBs would be unlikely to meet the proposed energy threshold for dehalogenation and would inhibit Dio by blocking the active site through a Cl—Se interaction. *Meta* and *para* XB donor-acceptor interactions are generally more favorable than *ortho*-XB interactions in PCBs, since these XB interactions can contain more than one adjacent Cl. In these cases, the electron withdrawing adjacent Cls stabilize the R-Cl* acceptor MO and increases the %X contribution for improved overlap with the $SeMe^-$ donor. PCBs may target different Dios depending on the donor-acceptor energies of the XB interactions. For example, PCBs with strong *meta*-XB interactions may prefer Dio2

inhibition, while those with strong *ortho*-XB interactions may prefer Dio3 inhibition. As PCBs become more *ortho*-halogenated, the twisting energy barrier around the C-C biphenyl bond increases, limiting flexibility and preventing some conformations from being readily accessible, suggesting the ability to adapt to the binding site may be important for inhibition of Dio and other thyroid hormone related proteins.

3.4 Computational Methods

Gaussian09[57] was used to calculate the DFT optimized geometries of the PCBs and the XB complexes with $SeMe^-$ using the M06-2X exchange-correlation functional[104] with a triple-ζ basis set for heavy atoms (TZVP). The relativistic core potential basis sets of Wadt and Hay was used for selenium atoms and augmented with polarization and diffuse functions.[122] Inspection of vibrational frequencies confirmed that optimized geometries were true minima. Donor-acceptor interaction energies $\Delta E_{D\rightarrow A}$ were determined by second-order perturbation theory as the stabilization of a filled σ-type orbital by the interaction with an empty σ*-type orbital. as described by Reed et al.[55] $\Delta E_{D\rightarrow A}$ values were calculated using NBO 3.0 as implemented in Gaussian09 to quantify the XB interaction in terms of the MO model.[175]

CHAPTER 4

AN *IN SILICO* APPROACH TO ELUCIDATE A DIMERIC STRUCTURE OF IODOTHYRONINE DEIODINASE III

4.1 Introduction

Iodothyronine deiodinases (Dios) are selenoproteins containing a rare selenocysteine residue involved in catalytic deiodination.[35,210–213] Dios adopt a thioredoxin-fold, containing five β-strands flanked by four α-helices.[214–218] Unlike other Trx proteins, which contain a CXXC motif in the active site, Dios incorporate a SCTU sequence (U = Sec). Three classes have been studied (Dio1, Dio2, Dio3), with each involved in regioselective deiodination of THs.[78,79,219–223] Dio2 and Dio3 are specific to outer ring deiodination (ORD) and inner ring deiodination (IRD) respectively, while Dio1 can perform both. Because of the regiospecificity of each Dio, they play different roles to maintain TH homeostasis. For example, ORD by Dio2 is essential for activating thyroid hormones to T_3, while IRD by Dio3 produces rT_3, an inactive TH metabolite. Deiodinase activity can be inhibited by endocrine disrupting chemicals (EDCs) such as polybrominated diphenyl ethers (PBDEs), polychlorinated biphenyls (PCBs), dibenzodioxins, iodoacetic acid (IAc), and gold thioglucose (GTG).[39,40,150,224,225]

The crystal structure of the Dio3 catalytic domain (PDB = 4TR4) was isolated by Schweizer et al.[35] The active site containing the Sec residue is overlooked by a flexible D-loop. The loop is on the surface of the protein and contains roughly 20 residues.[35] This irregular secondary structure has been classified as an Ω-loop, which was first described by Fetrow et al.[226] Ω-loops are found almost exclusively on protein surfaces and serve either a structural or catalytic role within the protein. For example, point mutations within the Ω-loop of β-lactamase show a decrease in catalytic activity.[227] The proximity of the Ω-loop to the active site in Dio3 suggests it has a possible role in substrate binding and catalytic deiodination.[36] During a 20 μs MD simulation, multiple stable conformations of the Ω-loop were observed, with the most stable conformation (**C**) exposing a cleft in the active site where T_4 can bind.[36] AutoDock was used to dock the T_4 substrate within the cleft of this conformation. The bonding,

nonbonding, and charge parameters of the I—Se XB interaction between the T_4 iodine and Sec selenium were derived from a previous study.[228] A "dummy atom" approach accounted for the σ-holes on iodines not directly involved in the XB interaction.[228] A 4.0 μs MD simulation of the $Dio3_{(C)}$-T_4 complex shows that the protein is stable and an ancillary outer ring XB interaction forms to a carboxylate oxygen of Asp211 within the Ω-loop.[36]

Currently, no structural data regarding a dimeric form of Dio3, which is the active form of the protein. An experimental study suggests Dio3 is catalytically active only as a homodimer.[46] Obtaining crystal structures of membrane-bound proteins is challenging.[229] Predicting these interactions automatically using high accuracy *in silico* methods level is computationally expensive for large systems.[230] Numerous protein-protein docking websites have been developed over the past 30 years, such as ClusPro, ZDOCK, and ATTRACT, with each differing in the algorithm used for searching the six-dimensional transformation space.[231–233] There are conflicting viewpoints regarding the location of the dimerization interface of Dio3. Sagar et al. suggests dimerization occurs at a large interfacial region that includes the top of two β-strands that make up an elongated β-sheet within the Ω-loop similar to the canonical $\beta_1\alpha_2\beta_2$ motif in thioredoxin (Figure 22A).[46,47] Because of the high level of sequence similarity around the $\beta_1\alpha_2\beta_2$ motif to that of oxidized human thioredoxin (PDB = 1ERU), a Dio model was superimposed onto the crystal structure of human thioredoxin.[47] On the other hand, Schweizer et al. postulates that Dio3 dimerizes along the $\alpha_3\beta_4$ interface.[35] In mammalian 2-Cys peroxiredoxin (HBP23, PDB = 1QQ2), the $\alpha_3\beta_4$ region mediates dimerization (Figure 22B).[234] The $\alpha_3\beta_4$ region shares high sequence similarity to the same domain in Dio3, and as such the Dio interface proposed by Schweizer was fitted onto that of HBP23.

In the present study, we compare the structure and sequence of Dio3 to other known thioredoxin-fold proteins to gain insight into the conflicting hypotheses regarding Dio3 dimerization. After determining the probable dimer interface of Dio3, a homodimer was constructed and refined using *in silico* databases SymmDock and GalaxyRefineComplex. The refined symmetric dimer was subject to MD

simulations to test for dimer stability. Hydrogen bonding analysis and MMGBSA calculations were performed to discern the key residues and interactions at the dimer interface that hold the oligomer together.

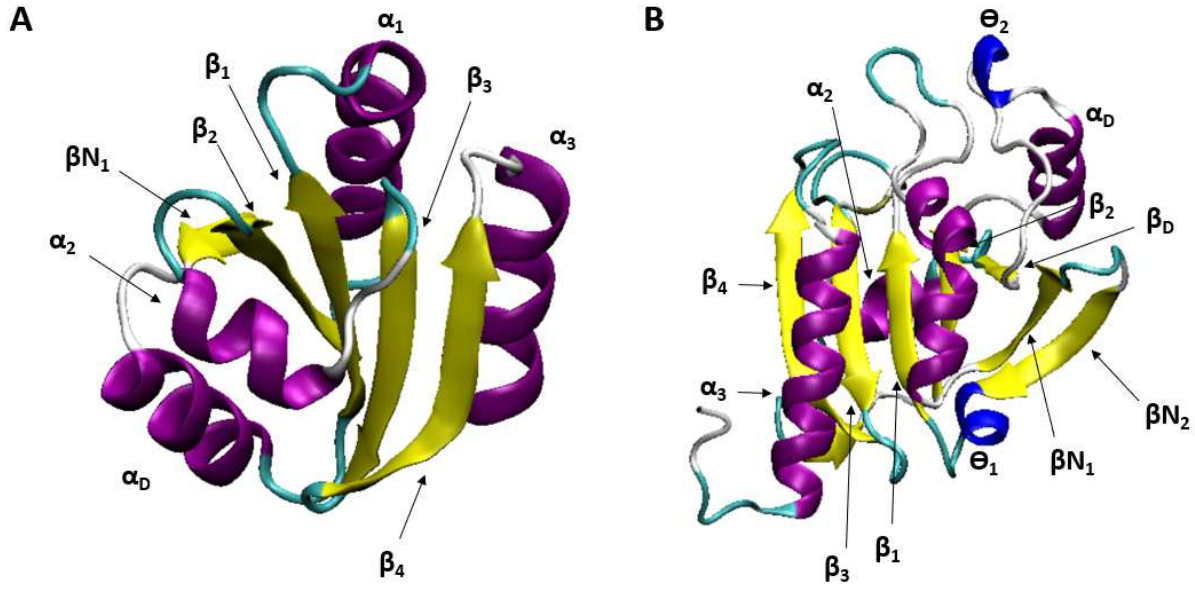

Figure 22. Template structures used as the basis for describing Dio3 dimerization. A) Human thioredoxin (PDB = 1ERU); B) HBP23 (PDB = 1QQ2). The regions involved in dimerization interactions in each protein are shown in opaque.

4.2 Results and Discussion

The structures of Dios are comparable to other proteins, such as glutaredoxins (Grxs), protein disulfide bond isomerases, and peroxiredoxins (Prxs), as they contain a thioredoxin-fold.[235] Prxs are proteins that serve as antioxidant proteins by reducing reactive oxygen and nitrogen species.[236,237] Most proteins in this subfamily have two conserved Cys residues (2-Cys): a peroxidatic cysteine (C_P) and a resolving cysteine (C_R). The C_P is located at the second cysteine of the universal thioredoxin CXXC motif and is directly involved in reducing peroxide substrates.[238] The C_R is typically located in the C-terminal

helix of peroxiredoxins and forms an inter-subunit disulfide bond to C_P.[236] The oligomeric state of peroxiredoxins changes depending on whether the protein is reduced or oxidized. In the reduced form, peroxiredoxins form $(\alpha_2)_5$ decamer structures such as the structure of plasmodium vivax Prx1a (PDB = 4L0U, Figure 23).[239] In the oxidized form, peroxiredoxins dissociate to from the decameric form to produce dimeric structures. Dissociation can occur at either the B-interface or the A-interface of decamers, which produces either A-type or B-type dimers respectively.[240] A-type (or "alternate") dimers are formed primarily by interactions at the $\beta_1\alpha_1$ turn, an α_D region, and a variable double β-sheet sequence region, while B-type (for β-strand) dimers consist of interactions of α_3 and β_4 (Figure 23).[236] Peroxiredoxins are further classified into different subfamilies (Prx1, Prx5, Prx6, Tpx) with each preferring different types of dimerization. For example, Prx5 and Tpx proteins prefer A-type dimerization, while Prx1 and Prx6 proteins prefer B-type dimerization.[236]

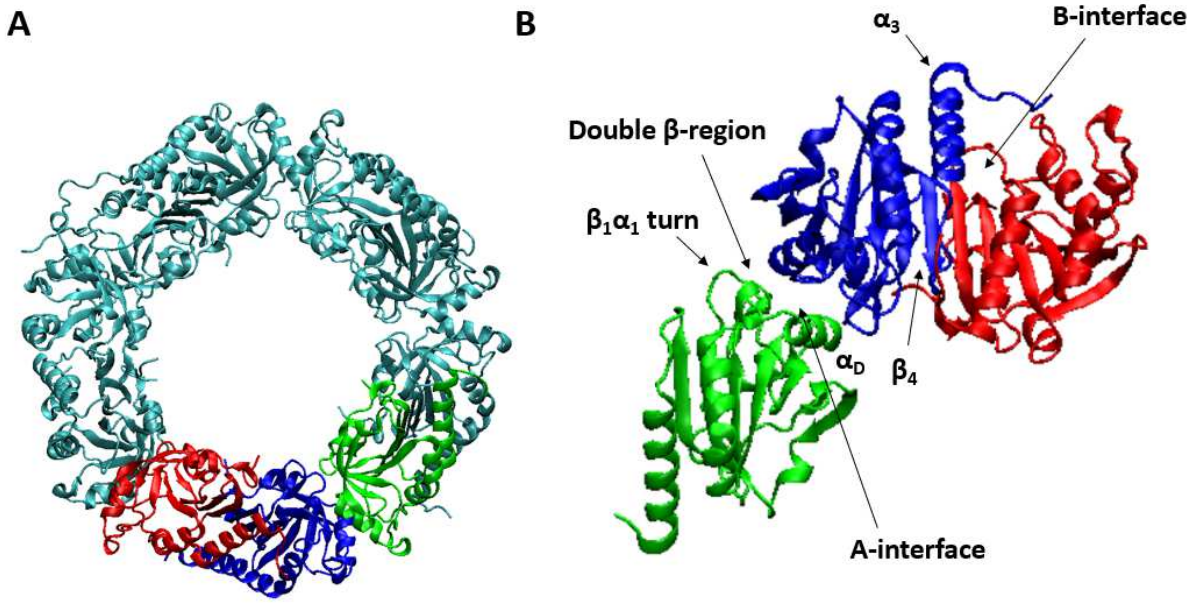

Figure 23. A) Decameric structure of plasmodium vivax Prx1a (PDB = 4L0U); B) close-up of the A-type and B-type dimer interfaces with key regions of each interface highlighted in opaque.

The conflicting viewpoints of proposed dimer interfaces of Dio3 between within the literature could be attributed to the observance of different dimerization interfaces in Prxs. To determine which description is the most reasonable to describe Dio3 dimerization, sequence alignments of Dio3 (4TR4) vs. A-type and B-type dimers was performed using the Clustal-Omega server (Figure 24, 25).[241] The regions of Dio3 (4TR4) aligns well with both A-type and B-type dimers up through β_2, however the variable sequence regions between β_2 and α_2 differs in both sequence alignments.

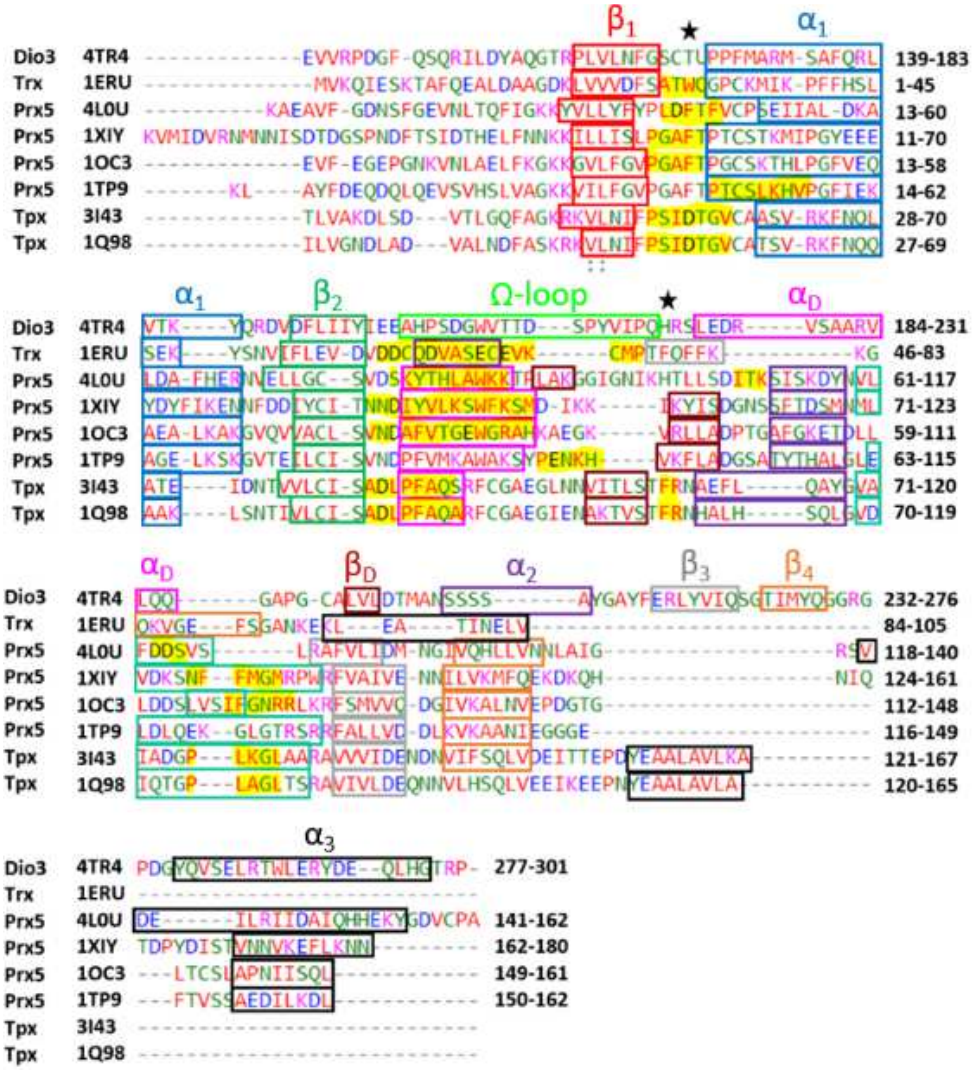

Figure 24. Sequence alignment of Dio3 (4TR4) vs. A-type dimer proteins. The dimer interface residues are highlighted in yellow. The locations of the conserved Phe residues in 'ball-and-socket' interactions are indicated with stars.

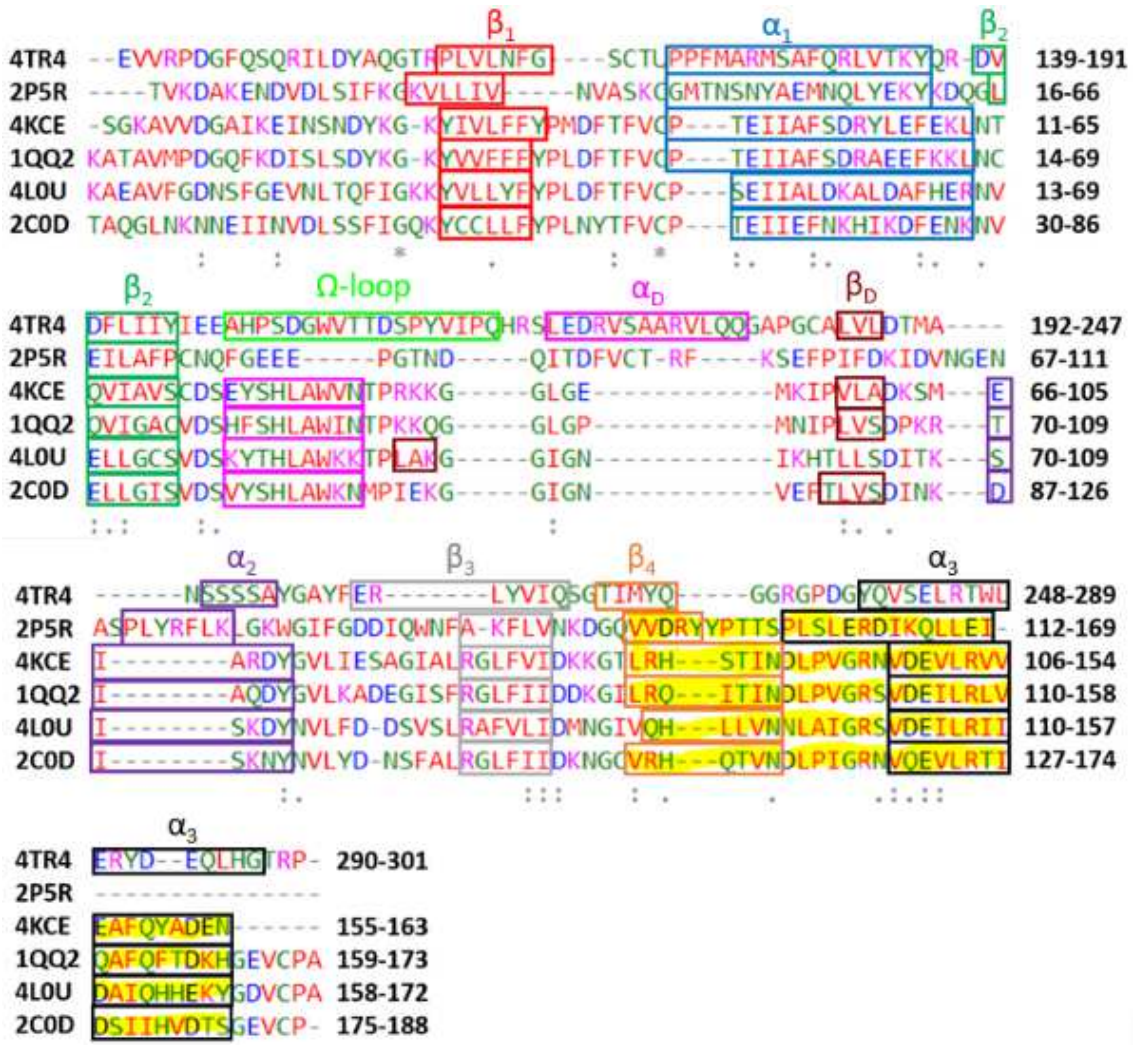

Figure 25. Sequence alignment of Dio3 (4TR4) vs. B-type dimer proteins. The dimer interface residues are highlighted in yellow.

In comparing Dio3 (4TR4) to the other A-type proteins, the sequence identity is very low (around 10-15%). All A-type dimers but the asymmetric dimer 1TP9 have the $\beta_1\alpha_1$ turn region, the α_D region, and the variable double-stranded β-sheet region within their dimer interfaces. A-type dimers contain a conserved Phe residue at either the $\beta_1\alpha_1$ turn or the region before α_2 region forms interdimer "ball-and-socket" hydrophobic interactions. "Ball-and-socket" interactions have been observed in other proteins such as glutathione peroxidase (Gpx) (PDB = 1GSU) and λ Cro (PDB = 5CRO).[239,242,243] In Gpx, Phe56 forms interdimer hydrophobic interactions with Leu137, Phe140, and Val98, while in λ Cro Phe58

interacts with Ala33 and Ile30 on the opposite chain.[242,243] In both proteins, mutation of these key Phe residues largely destabilize the dimeric state.[242,243] The Prx5 proteins (4L0U, 1XIY, 1TP9, and 1OC3) each have the conserved 'ball-and-socket' Phe residue within the $\beta_1\alpha_1$ turn, while the conserved Phe in Tpx proteins (3I43 and 1Q98) is in the region preceding α_2 (Figure 24). The interfacial region of 1ERU, the template structure used for the dimer description by Sagar et al., does not have a Phe residue at either of the A-type interfaces but does contain Trp31 within the $\beta_1\alpha_1$ region in the same position as the conserved Phe in Prx5 proteins. Within 1ERU, Trp31 could emulate the A-type dimer 'ball-and-socket' hydrophobic interactions by interacting with Val71/Met74 on the opposite monomer (Figure 26). 1ERU lacks the α_D and extended double β-sheet regions of the other A-type dimers and instead has an interfacial disulfide bond between Cys71 residues to aid dimer stabilization.

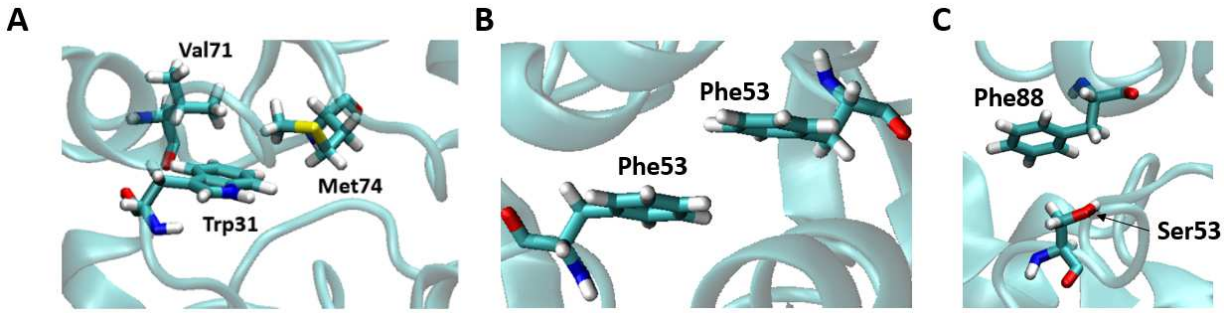

Figure 26. Structures of comparable 'ball-and-socket' interactions within A) 1ERU; B) 1XIY; C) 3I43.

Dio3 (4TR4) does not have a Phe at either of the conserved positions in the Prx5 or Tpx proteins and instead has Thr and His occupying those spots in the sequence alignments (Figure 24). In Dio3, the only Phe located at the surface is Phe258, which shields the substrate in the active site from the solvent.[35] Furthermore, A-type dimerization of Dio3 is improbable from a structural standpoint. By overlaying two monomer structures of Dio3 onto a Prx5 protein (1XIY) and a Tpx protein (3I43), it is evident that the

sterics of the Ω-loop prohibit dimerization at the $\beta_1\alpha_1$ and α_D regions simultaneously (Figure 27). In comparing Dio3 to 1ERU, 1ERU has a Cys-Cys disulfide bond at the dimer interface that aids dimer stability, which Dio3 does not contain. Previous studies that have examined amino acid propensities within protein structures also do not support the A-type dimerization description of Dio3. A recent study evaluated the propensities of amino acids to occur at dimer interface regions and have found Arg, Tyr, and Trp to be the most common residues in these regions and are considered 'hotspots' in Ala-scanning experiments.[244] The Tyr and Trp residues are typically found more towards the center of dimer interfaces, which would not be the case if it is assumed Dio dimerizes in a A-type fashion.[244] In addition, most of the residues within the Ω-loop of Dio3 that make up the proposed β-sheets according to Sagar et al. are residues not typically seen in these secondary structures. Of the residues in the proposed β-sheet region (sequence: EAHPSDGWVTT), only His and Trp are commonly found in β-sheets.[245] Based upon the available sequential and structural data of known A-type dimers and the structure of 1ERU, these observations suggest A-type dimerization of Dio3 is unlikely to occur and that 1ERU is not a viable template for Dio3 dimerization.

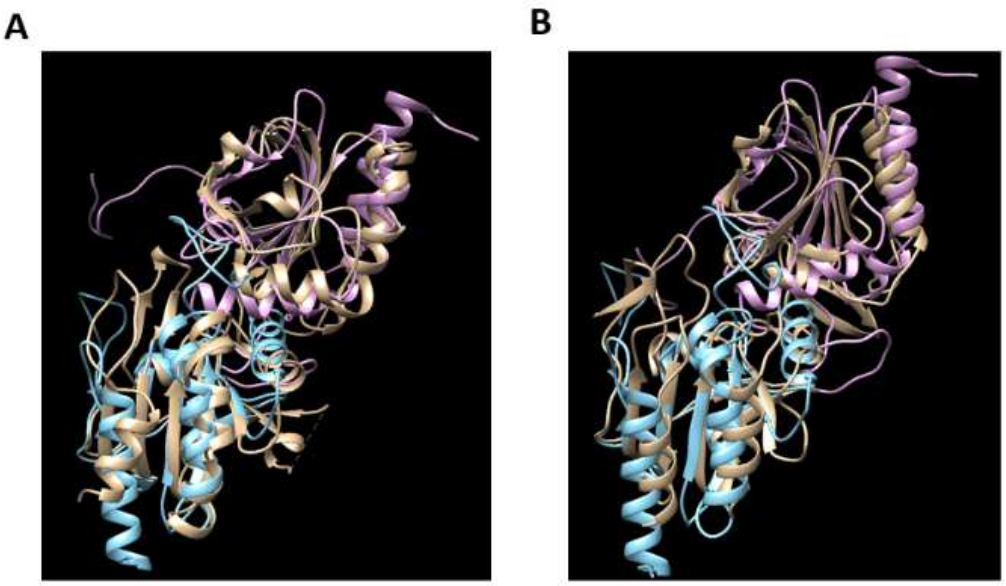

Figure 27. Structural overlays of Dio3 monomers (in blue, pink) on top of dimeric structures of A) 1XIY; B) 3I43 (in tan).

The sequence identity of Dio3 vs. the B-type dimers is around 15-20%, which is higher than the sequence identity of A-type dimers. This level of sequence similarity almost falls in line with the established 'twilight zone' of 20-25%, suggesting that some of the conserved regions of Dio3 and B-type proteins could have evolved from a common ancestral protein.[246] The interface of B-type dimers consists of residues within β_4, α_3, and the $\beta_4\alpha_3$ turn, and vary between Dio3 and B-type proteins (Figure 25). A conserved Gly-Arg dyad sequence is located within the $\alpha_3\beta_4$-turn with 2-Cys peroxiredoxin proteins, 2C0D, 1QQ2, and 4KCE (Figure 25). In addition, a conserved Val-X-Glu triad within the 2-Cys peroxiredoxins is near the beginning of α_3 (Figure 25). Within the 2-Cys peroxiredoxins, this conserved Glu residue forms an intradimer hydrogen bond to a conserved Arg residue positioned three residues down the sequence in 1QQ2 and 4KCE (Figure 25). In the C-terminus, 1QQ2, 2C0D, and 4L0U all contain C_R, which aids association into decameric structures in the oxidized state by forming a disulfide bond to C_P near the A-type interface.[236]

Within Dio3, the slightly shorter β-sheet region of Dio3 is compensated by a more flexible Gly-rich $\alpha_3\beta_4$-turn. Dio3 shares the conserved Gly-Arg dyad with other B-type proteins, however the dyad is in the middle of the turn in Dio3 and followed by another Gly residue (Figure 25). This Arg residue in Dio3 is Arg275 and has been proposed to help bind the T_4 substrate.[35] The Gly-rich turn of Dio3 may be necessary to allow for more flexibility to accommodate the large T_4 substrate. Within α_3, Dio3 shares the Val-X-Glu triad and an Arg residue in roughly the same position with the 2-Cys peroxiredoxin proteins, suggesting Dio3 could display similar stabilizing intramonomer Glu-Arg hydrogen bonding interactions. Finally, Dio3 does not have C_R in the C-terminal region, suggesting A-type association of dimers to form decamers is unlikely to occur. Based upon sequential and structural similarities between Dio3 and B-type proteins, we presume Dio3 dimerizes in a B-type fashion and attempt to construct homodimer of Dio3 based upon the B-type description using protein-protein docking databases.

Protein-protein docking databases are divided into two main categories, template-based modeling and template-free docking.[247] In template-based modeling, a protein complex is constructed based on a known deposited structure in the Protein Data Bank. Template-based modeling assumes protein-protein complexes interact in a similar fashion to known protein structures if the interacting pairs share over 30% sequence identity.[248] Template-free docking databases uses two stages for structure prediction, a sampling stage and a scoring stage. During the sampling stage, thousands of structures are generated and then are subsequently scored and ranked based upon known interfacial interactions in other proteins.[249] For the initial protein-protein docking attempts, monomers of the Dio3 X-ray structure ($Dio3_{(\mathbf{X\text{-}ray})}$) and a structure containing a stable Ω-loop conformation ($Dio3_{(C)}$) that exposes the active site Sec residue were submitted to a template-based server (GalaxyGemini) and a template-free server (HawkDock).[36] For each conformation, GalaxyGemini predicted the same 5 template structures, with only models 3 and 4 producing dimers (Table 2). The dimer templates are from a thioredoxin-like protein from *Aeropyrum pernix* (3HA9) and a Gpx5 protein (2P5Q), both of which have B-type dimerization (Figure 28). HawkDock produced the top ten structures for each conformation based upon MMGBSA energies of the

complexes. Although the dimers generated from the Dio3 X-ray structure have lower MMGBSA interaction energies compared to $Dio3_{(C)}$, none of these dimers display B-type dimerization and therefore were excluded from further analysis (Table 3). From the $Dio3_{(C)}$ structure, only model 6 positions the α_3 and β_4 regions at the interface akin to a B-type dimer (Figure 29). Energetic calculations within HawkDock show formation of the B-type dimer is favorable (ΔG = -34.65 kcal mol^{-1}, Figure 29, Table 3). Although both GalaxyGemini and HawkDock predicted B-type dimers, the produced structures are unrefined, as they do not account for optimal interfacial sidechain orientations. In addition, in both $Dio3_{(X\text{-}ray)}$ and $Dio3_{(C)}$, the β-sheet at the $\alpha_3\beta_4$ interface adopts a crooked conformation. Although there are proteins that have interfacial interactions between crooked β-sheets, such as 4HPM and 1Z4E,[250] initial MD simulations of $Dio3_{(X\text{-}ray)}$ and $Dio3_{(C)}$ dimers with interacting crooked β-sheets show these structures become unstable quickly. To overcome this issue, the β-sheet within monomeric Dio3 needs to be refined before protein-protein docking can be carried out.

Table 2. Oligomer template structural data generated by GalaxyGemini for $Dio3_{(X\text{-}ray)}$ and $Dio3_{(C)}$.

Model	Oligomer Template	No. of Subunits	Structure Similarity
1	3FKF	4	69.72
2	3GL3	4	68.81
3	3HA9	2	65.29
4	2P5Q	2	67.31
5	5Y63	10	63.87

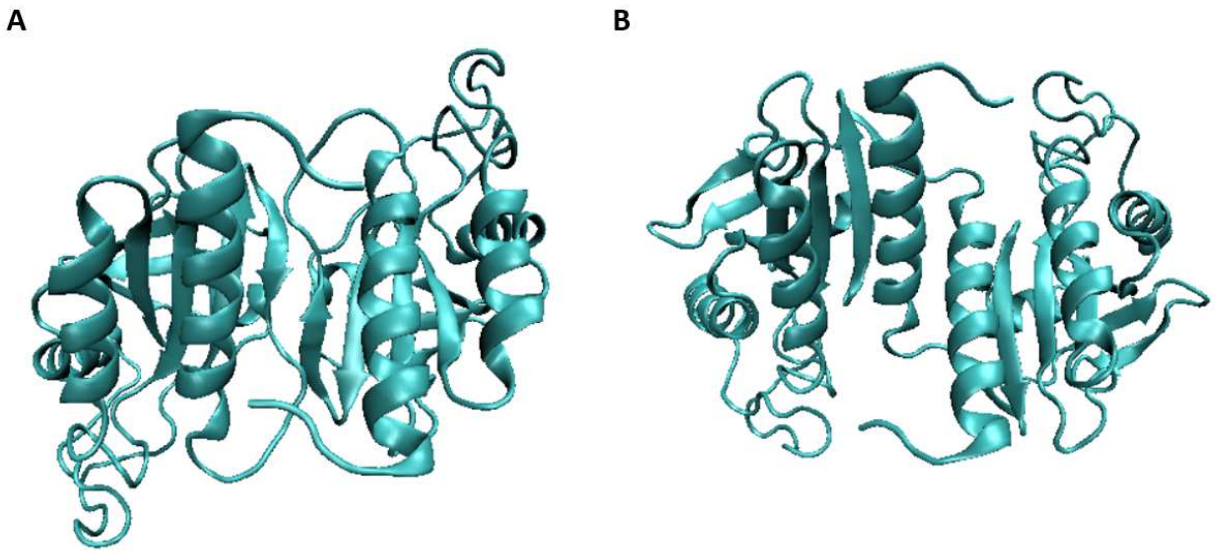

Figure 28. Structures of the template structures generated using the GalaxyGemini server with the structure of Dio3 as the input with templates (A) 3HA9; (B) 2P5Q.

Table 3. Binding energies (in kcal mol^{-1}) of the top 10 models of Dio3$_{(X\text{-}ray)}$ and Dio3$_{(C)}$ predicted by HawkDock.

Model	**Dio3$_{(X\text{-}ray)}$**	**Dio3$_{(C)}$**
1	-25.17	-9.45
2	-33.85	-24.96
3	-35.65	-26.30
4	-22.99	-13.42
5	-53.87	-30.67
6	-31.00	-34.65
7	-48.36	-8.52
8	-20.65	-21.14
9	-26.48	-27.72
10	-33.64	-6.57

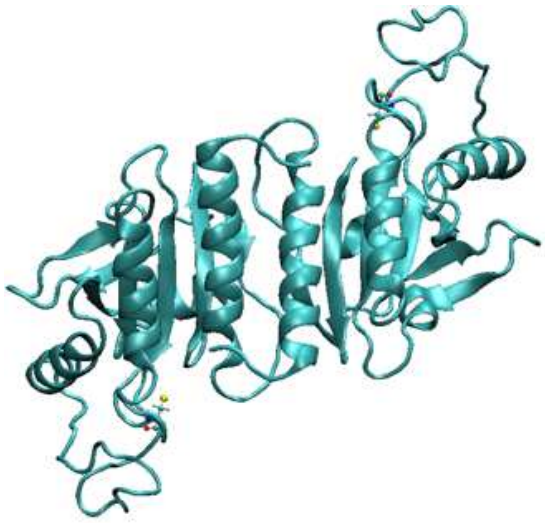

Figure 29. Structure of the B-type (model 6) dimer generated from $Dio3_{(C)}$ using the HawkDock Server.

An equilibrated $Dio3_{(C)}$-T_4 complex from a previous study was used as the starting structure for refinement of the interfacial β-sheet.[36] CHIMERA was used to set the dihedral angles of the residues within the β-sheet (Thr268 to Gln272) to mimic those commonly found in parallel β-sheets and the positions of the β3-β4 turn residues (Ser266 and Gly267) were adjusted slightly (See Methods for Details). The refined monomer was then submitted to the SymmDock server to obtain symmetric dimers. SymmDock is a free web server that utilizes a geometry-based algorithm to produce symmetric multimers with a given order *n*.[230] The details of the files submitted to the SymmDock server are described in the Methods section. SymmDock constructed 58 unique symmetric B-type-like dimers. Most of the generated models contain structural features that could cause the dimers to destabilize quickly during MD simulation. For example, model 2 shows the interfacial β-sheets to be nearly perpendicular to each other, which prevents interfacial β-β interactions from occurring (Figure 30A). On the other hand, although model 11 has closely interacting antiparallel interfacial β-sheets, the lack of interactions between the α-helices on the monomers could induce instability (Figure 30B). Of these dimers, only model 16 produced a structure that resembled a B-type dimer with a thioredoxin-fold, as it positions the $\alpha_3\beta_4$ regions of the

monomers to interact in an anti-parallel fashion (Score = 5750, Figure 30C). Within model 16, close contacts exist between the sidechains of the Arg281 residues in the α-helix and the backbone atoms of Thr268 and Gly273 (Figure 30D and 30E), which need to be adjusted before an MD simulation can be ran on this protein.

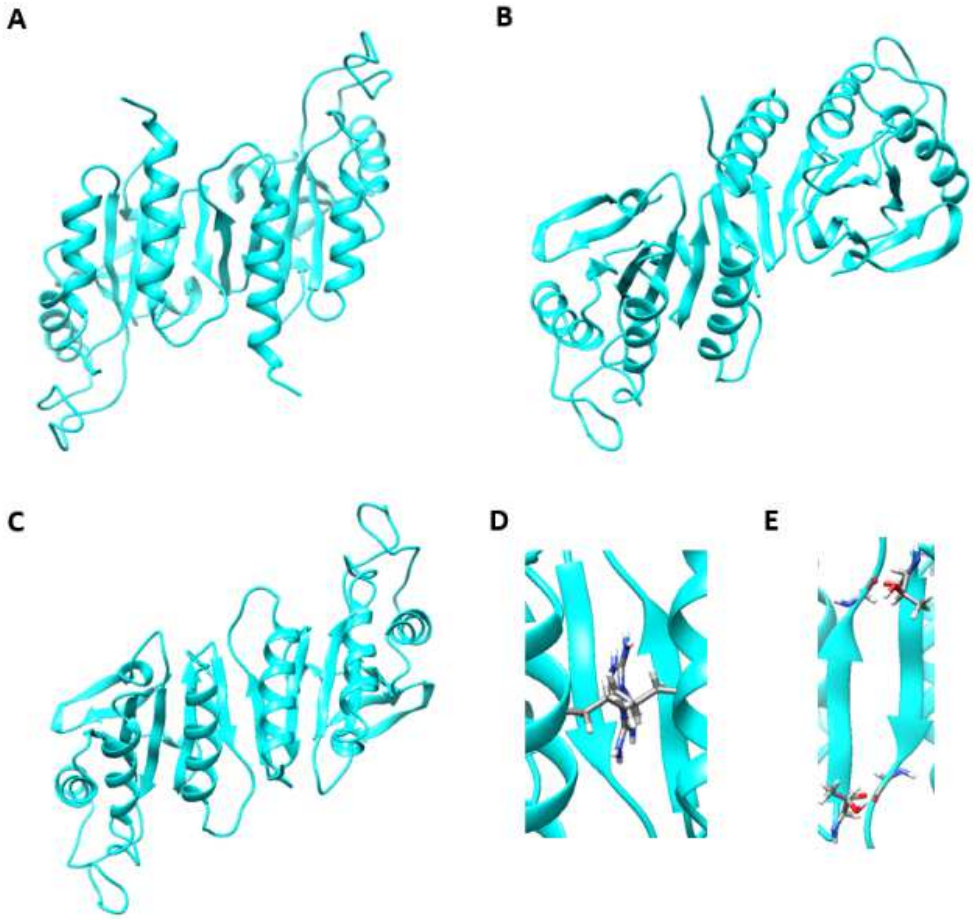

Figure 30. Dimers generated from the SymmDock server. A) Model 2; B) Model 11; C) Model 16. D) Close contacts between Arg281 residues between the α-helices in model 16; E) Close contacts between Thr268 and Gly273 between the turn and β-sheets in model 16.

The SymmDock-generated dimer was submitted to GalaxyRefineComplex to reorient the sidechains at the interface. GalaxyRefineComplex utilizes a sampling method in which multiple short MD simulations are run to allow for repetitive repacking of the side chains within the dimer interface.[251] Comparative studies of models generated by ZDOCK, M-ZDOCK, CAPRI, and CASP experiments show the refining process utilized by GalaxyRefineComplex produced the most favorable structures in most cases.[232,252,253] The refining process emulates protein-protein dimerization by allowing the sidechains between the two monomers to dictate inter-protein orientations and intra-protein backbone conformations.[251] While the other databases listed above can perform repacking of sidechains in interface regions, GalaxyRefineComplex is the only web server that allows for symmetric rearrangement of the interface while simultaneously reducing close contacts.

From the generated SymmDock dimer, GalaxyRefineComplex produced 10 unique structures that repack the sidechains within the dimer interface region. The 10 structures were evaluated based upon the results of the ligand RMSD (l-RMSD) according to the critical assessment of predicted interactions (CAPRI) developed by Lensink et al.; incorrect of l-RMSD > 10 Å, acceptable if l-RMSD = 5-10 Å, medium if l-RMSD = 1-5 Å, or high quality if l-RMSD < 1 Å.[253] While this assessment has been widely accepted as a measure of structure quality, visual inspection of the generated structures is necessary to ensure no unfavorable interactions, such as positively-charged sidechains being close together, are generated. To narrow down the viable structures, only the high-quality structures were considered (models 7, 8, and 10 with l-RMSDs of 0.976, 0.939, and 0.980 respectively, Table 4). The orientations of the sidechains at the interfacial α-helices and β-sheet are all highly similar within the three high-quality structures (Figure 31). In each structure, Arg291 orients inward and forms a close interaction to the carbonyl oxygen of Gln295 on the opposite α-helix (Figure 31A). However, in models 7 and 10, the sidechains of Tyr271 of the β-sheet and Trp288 of the α-helix have close contacts between the sidechains, whereas the sidechains of Tyr271 and Trp288 in model 8 are orientated to allow for potential π-stacking

interactions (Figure 31B). In addition, model 8 has the lowest l-RMSD out all the results and was chosen to be subject to MD simulation.

Table 4. List of results generated from GalaxyRefineComplex and their respective ligand RMSDs.

Model	Ligand RMSD
1	6.337
2	8.194
3	7.745
4	7.191
5	8.194
6	1.018
7	0.976
8	0.939
9	1.066
10	0.980

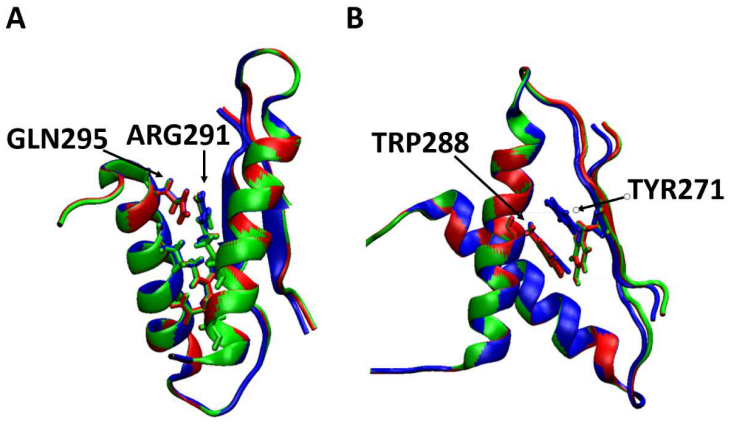

Figure 31. Overlays of the high-quality models generated by GalaxyRefineComplex according to CAPRI. The colors red, blue, and green correspond to models 7, 8 and 10 respectively. A) Orientations of the sidechains of Arg291 and Gln295; B) Orientations of the sidechains of Tyr271 and Trp288.

A 2 μs MD simulation was run on the constructed dimer. From 0-1 μs, the MD simulation was carried out with T_4 substrates bound to the active sites. From 1-2 μs, the two T_4 substrates were removed to verify that the interface maintains its integrity. Energies are calculated using MMGBSA and expressed as ΔG_{holo} and ΔG_{apo} for the T_4-bound (0-1 μs) and T_4-unbound (1-2 μs) parts of the simulation respectively. $\Delta\Delta G$ represents the difference in energies between the *holo* and *apo* parts of the simulation. MMGBSA uses molecular mechanics in tandem with the generalized Born model and the solvent accessibility method to predict free energies of a system.[254] MMGBSA has been shown to have high accuracy in predicting dimerization energies and is able to identify energetic contributions of individual residues through decomposition analysis.[255,256] MMGBSA interaction energies indicate dimerization of Dio3 with T_4 bound is favorable (ΔG_{holo} = -38.62 ± 6.81 kcal mol^{-1}) and is further stabilized when the T_4 residues are removed (ΔG_{apo} = -45.67 ± 12.03 kcal mol^{-1}). The time evolution of interaction energies shows the electrostatic contributions far outweigh the van der Waals (vdW) interactions within the interface region (Figure 32). The trends in interaction energies are consistent with the number of hydrogen bonding and hydrophobic interactions, which remain constant in the MD simulation (Figure 33). Over the course of the 2 μs MD simulation, the protein and its Ω-loops remain stable as evidenced by the RMSD plot (Figure 34A). During the first half of the simulation, the T_4 residues remain bound to the active site and the outer-ring XB interactions to Asp211 in both monomer subunits remain intact. In addition, removal of the two T_4 substrates at 1 μs slightly destabilizes the protein, as one of the Ω-loops deviates from the stable conformation (**C**) at ~1.5 μs due to the loss of the T_4 XB interactions to Asp211 within the Ω-loop (Figure 34A and 34C).[36] Fluctuations within the RMSD plot of the monomer interfaces indicate these regions undergo conformational changes over the course of the 2 μs MD simulation (Figure 34B).

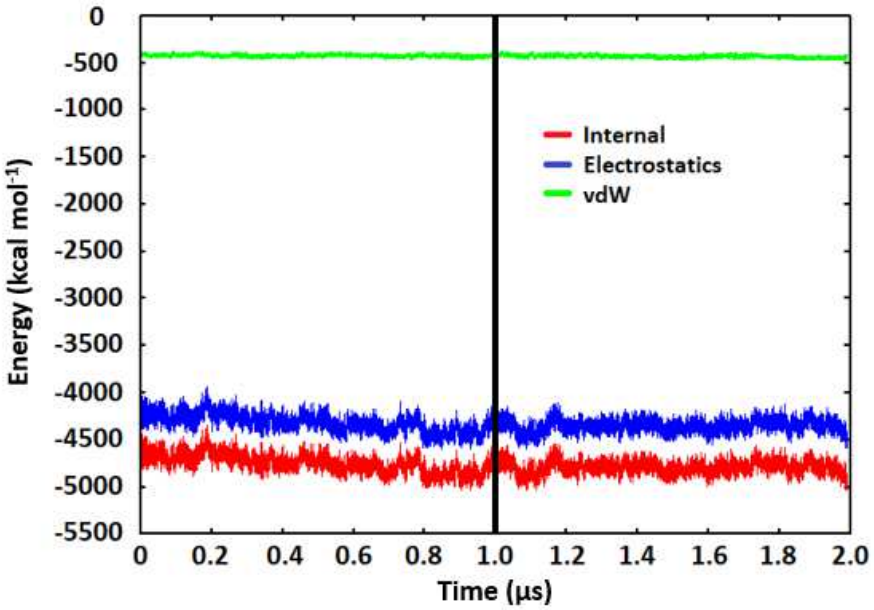

Figure 32. Evolution of interaction energy profiles in the Dio3$_{(C)}$ dimer interface region.

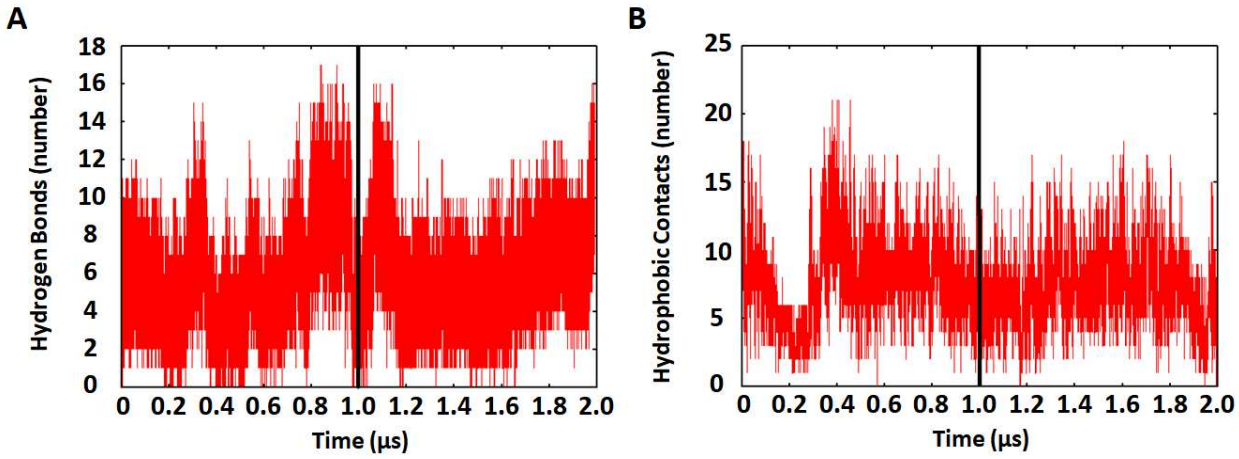

Figure 33. Evolution of interdimer interactions at the Dio3$_{(C)}$ dimer interface region. A) Hydrogen bonds between dimer interfaces; B) Hydrophobic contacts at the dimer interface.

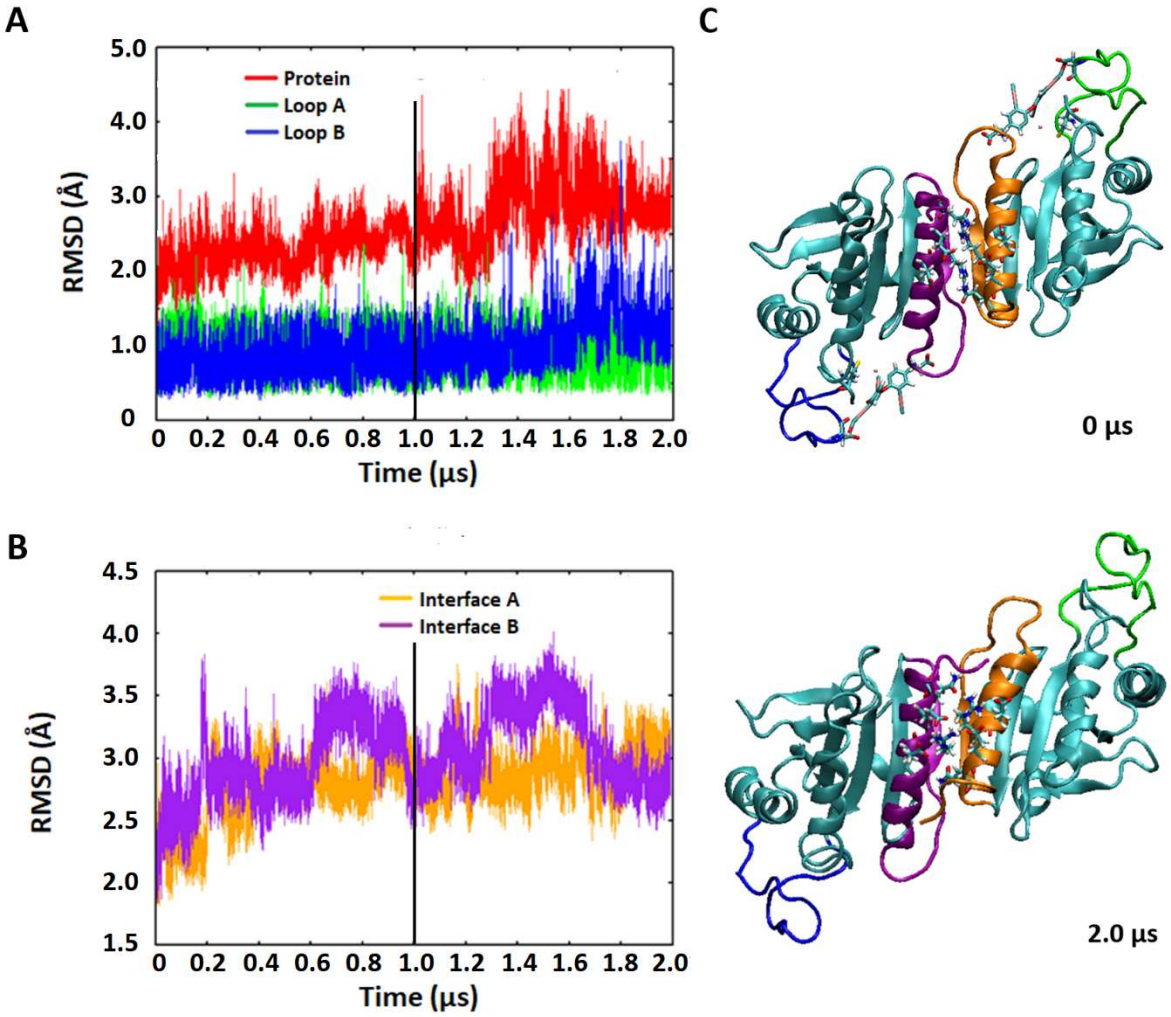

Figure 34. Statistical analysis of the MD simulation of the $Dio3_{(C)}$ dimer after the 2 T_4 residues are removed. A) RMSD plot of the entire protein and its two loops on each monomer subunit; B) RMSD plot of the interfacial residues on both monomer subunits; C) structures of the Dio3 dimer at 0 μs and 2 μs simulation time. The black line indicates the point at which the 2 T_4 residues are removed.

To better understand the key interactions that influence these conformational changes at the interfacial region within the Dio3 dimer, hydrogen bonding analysis was carried out. The hydrogen bonding interactions were calculated using the pairwise energy decomposition analysis in MMPBSA for all possible residue pairings between interfacial residues (residues 267-301). The pairwise residue interaction energies include all hydrogen bonding instances between pairs, meaning that more than one potential hydrogen bonding interaction between the pairs could persist during the simulation.[257] Hydrogen

bonds can form or be lost very rapidly over the course of an MD simulation, which could lead to large variances in per-residue hydrogen bonding energies and also high standard deviations (SDs) of the energy values.[257] The magnitude of the pairwise SDs can identify whether hydrogen bonds are dynamic (if SDs are high) or static (if SDs are low). The data was sorted based upon the types of interactions involved (β-β interactions if interactions occur between interfacial β-sheet residues, etc.).

Between the β-sheets, the strongest and most persistent hydrogen bonding interactions are β-β Met270-Gln272 BB-BB interactions, which anchor the β-sheets together. Even after the two T_4 substrates are removed, the Met270-Gln272 BB-BB interactions are only destabilized by roughly 0.3 kcal mol^{-1} and the SD remains low (ΔG_{holo} = -4.13 ± 0.38 kcal mol^{-1}, ΔG_{apo} = -3.84 ± 0.07 kcal mol^{-1}) (Table 5 and 6). Distance plots between these backbone interactions show three of the BB-BB interactions remain static throughout the course of the MD simulation, with the Met270H-Gln272O interaction only being temporarily lost during the 0.6-0.8 μs and 1.3-1.5 μs intervals (Figure 35). Other intermittent β-β BB-BB interactions between the β-sheets occur during the MD simulation, including Thr268-Gln272, Met270-Tyr271, and Ile269-Gln272. Two of the three interactions, Met270-Tyr271 and Ile269-272, become slightly destabilized upon removal of the 2 T_4 substrates ($\Delta\Delta G$ = +0.19 and +0.26 kcal mol^{-1} respectively), while the interactions between Thr268-Gln272 are more destabilized by the removal of T_4 substrates ($\Delta\Delta G$ = +1.32 kcal mol^{-1}). These three interactions have low SDs and remain relatively static, similar to Met270-Gln272 (Table 5 and 6). Although the sequences of Dio3 and other B-type proteins differ in the β-sheet region, the persistence of BB-BB interactions in the β-sheets in Dio3 is a characteristic shared by all B-type proteins (Table 7). These interactions may be necessary to stabilize the β-sheets within the Dio3 dimer.

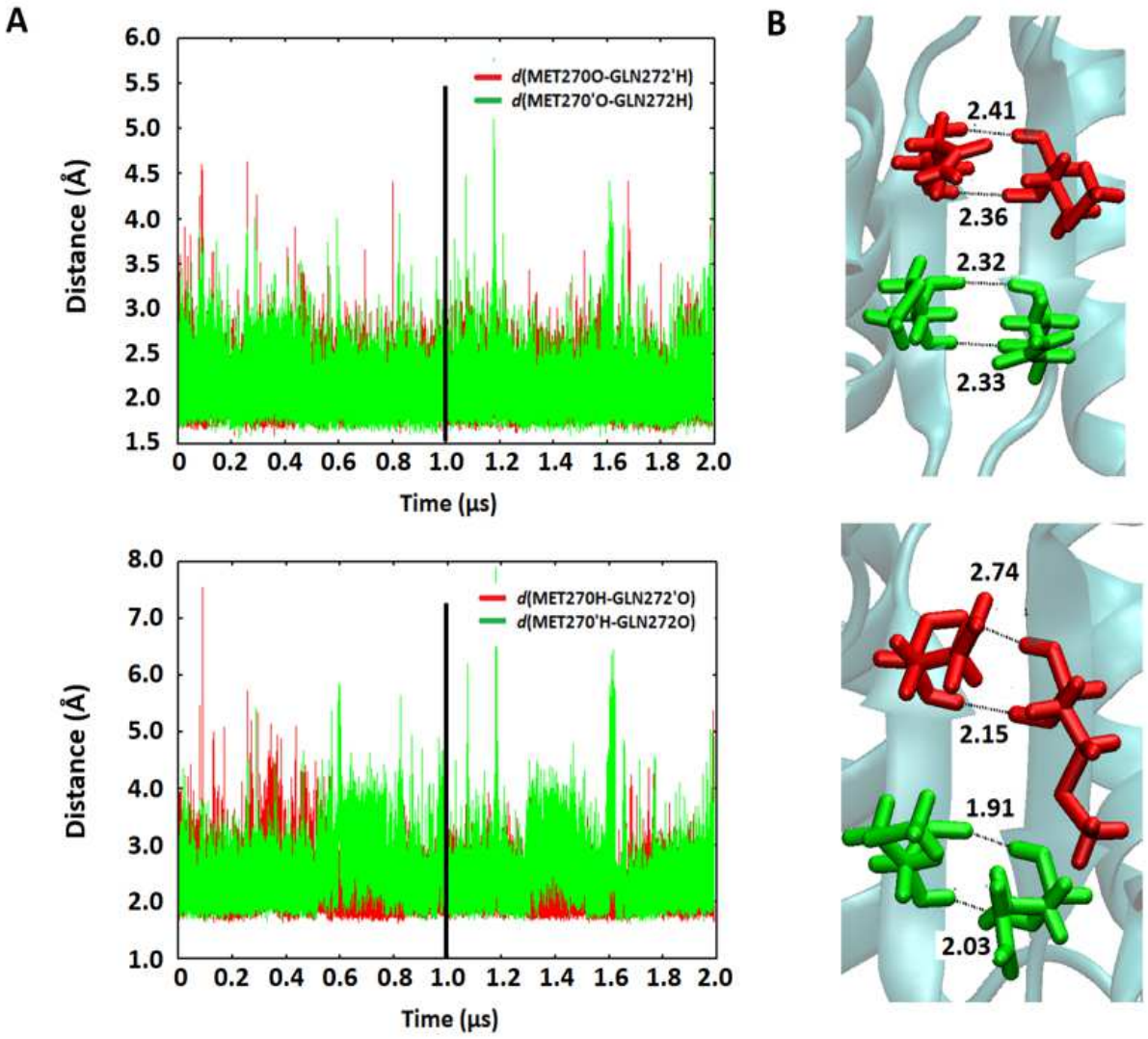

Figure 35. A) Distance plots of the two stable hydrogen bonds between Met270-Gln272 backbone atoms; B) initial and final structures of the Met270-Gln272 hydrogen bonding interactions. The black line indicates the point at which the 2 T_4 residues are removed.

Table 5. Energy of hydrogen bonds along the dimer interface region of Dio3 during the *holo* simulation.

	Interaction	ΔG (kcal mol^{-1})
β-β Interdimer (BB-BB)	Met270-Gln272	-4.13 ± 0.38
	Thr268-Gln272	-1.86 ± 0.65
	Met270-Tyr271	-2.35 ± 0.29
	Ile269-Gln272	-2.17 ± 0.19
α-α Interdimer (SC-SC)	Arg291-Glu294	-1.17 ± 0.44
	Glu294-Gln295	-1.24 ± 0.17
	Arg291-Gln295	-1.87 ± 0.56
α-α Intramonomer (SC-SC)	Arg291-Glu290	-0.23 ± 0.14
	Arg291-Glu294	-2.66 ± 0.59

Table 6. Energy of hydrogen bonds along the dimer interface region of Dio3 during the *apo* simulation.

	Interaction	ΔG (kcal mol^{-1})
β-β Interdimer (BB-BB)	Met270-Gln272	-3.84 ± 0.07
	Thr268-Gln272	-0.54 ± 0.50
	Met270-Tyr271	-2.16 ± 0.30
	Ile269-Gln272	-1.90 ± 0.31
α-α Interdimer (SC-SC)	Arg291-Glu294	-3.96 ± 1.29
	Glu294-Gln295	N/A
	Arg291-Gln295	-1.99 ± 1.00
α-α Intramonomer (SC-SC)	Arg291-Glu290	-2.08 ± 0.83
	Arg291-Glu294	-1.11 ± 0.34

Table 7. List of all notable hydrogen bonds and interactions in the other B-type proteins examined in this study.

Protein	Interdimer H-bonds	Intramonomer H-bonds
2P5R	Tyr151-Arg149 (SC-SC) (turn-β) Thr153-Asp148 (SC-SC) (turn-β) Arg161-Ser158 (SC-SC) (α-α) Ser158-Asp162 (SC-SC) (α-α)	Arg161-Asp162 (SC-SC)** (α-α) Thr154-Tyr151 (BB-BB) (α-turn)
2C0D	Arg154-Asp160 (SC-SC) (β-turn) Arg154-Asp160 (BB-BB) (β-turn) Val158-Gln156 (BB-BB)* (β-β)	Arg154-Asp181 (SC-SC)** (β-α) Asn159-Ile163 (SC-BB) (turn-turn) Asn159-Gly164 (SC-BB) (turn-turn)
4KCE	Asp140-Arg134 (SC-SC) (β-β) Asp140-Arg134 (BB-BB) (β-β) Hip135-Asn139 (SC-SC) (β-β) Ile138-Ser136 (BB-BB)* (β-β) Arg152-Gly144 (SC-BB) (α-turn) Glu139-Asn146 (SC-SC) (α-α)	Arg152-Glu149 (SC-SC)** (α-α) Asn139-Val143 (SC-BB) (β-turn) Asn139-Gly144 (SC-BB) (β-turn) Val143-Asp140 (BB-BB) (turn-β)
4L0U	Val141-Leu139 (BB-BB)* (β-β) Arg155-Glu152 (SC-SC) (α-α) Gln137-Glu152 (SC-SC) (turn-turn)	N/A
1QQ2	Ile142-Ile140 (BB-BB)* (β-β) Asn143-Gln139 (SC-SC) (β-β) Thr141-Gln139 (SC-SC) (β-β) Ser150-Glu153 (SC-SC) (α-α)	Arg138-Asp165 (SC-SC) (β-α) Arg156-Glu153 (SC-SC)** (α-α) Val147-Leu145 (BB-BB) (turn-β) Gly148-Leu145 (BB-BB) (turn-β)

*Key intermonomer BB-BB interaction.

**Key intramonomer SC-SC interaction.

The interactions between the α-helices are slightly less favorable overall compared to the β-sheets (Table 5 and 6). Four residues near the center of the interfacial α-helix share interactions with one another (Arg291, Glu290, Glu294, and Gln295). Arg291 has interdimer SC-SC interactions with Glu294 and Gln295 and accounts the largest portion of the dimerization binding energy between the α-helices (Table 5 and 6). Three of the interactions within the α-helices, including the intramonomer SC-SC Arg291-Glu290, interdimer SC-SC Arg291-Glu290, and interdimer SC-SC Arg291-Gln295 interactions, become more favorable after the two T_4 substrates are removed ($\Delta\Delta G$ = -2.79, -1.85, and -0.12 kcal mol^{-1} respectively). In addition, the interdimer Arg291-Glu294 and Arg291-Gln295 SC-SC interactions become more dynamic after the T_4 substrates are removed (Table 5 and 6). The intramonomer Arg291-294

interactions become destabilized by 1.55 kcal mol^{-1}, while the interdimer Glu290-Gln295 interactions become completely lost after the two T_4 residues are removed.

Intramonomer interactions involving an Arg residue is a characteristic that Dio3 shares with some of the other B-type dimers examined in this study, 1QQ2, 2P5R, and 4KCE (Table 6). Dio3 was overlayed onto each of these structures at Arg291 to compare the orientations of the Arg residue (Figure 36). Of these three structures, the orientations of Arg156 in 1QQ2 and Arg152 in 4KCE slightly overlay with that of Dio3, as they both form SC-SC interactions with Glu153 and Glu149 respectively, which is 3 residues down the helix (Figure 36A and 36C, Table 6). However, Arg156 of Dio3 assumes a more 'bent' conformation to best accommodate the SC-SC interactions with the acidic groups of the nearby Glu residues (Figure 36). Arg161 of 2P5R does not overlay well, as it assumes an extended conformation with the inward-facing Asp162 (Figure 36B, Table 4). However, in these B-type proteins, the propensity for Arg residues within interfacial α-helices to form both interdimer and intramonomer interactions with nearby acidic sidechains (Glu/Asp) in other B-type proteins suggests these interactions are key to holding together the α-helices in the Dio3 dimer. In addition, Arg residues within the other B-type dimers may also share interactions with other nearby acidic residues that are not shown in crystal structures. For example, 4KCE could have interactions with another nearby Glu residue (Glu190) rather than Glu184 in solution.

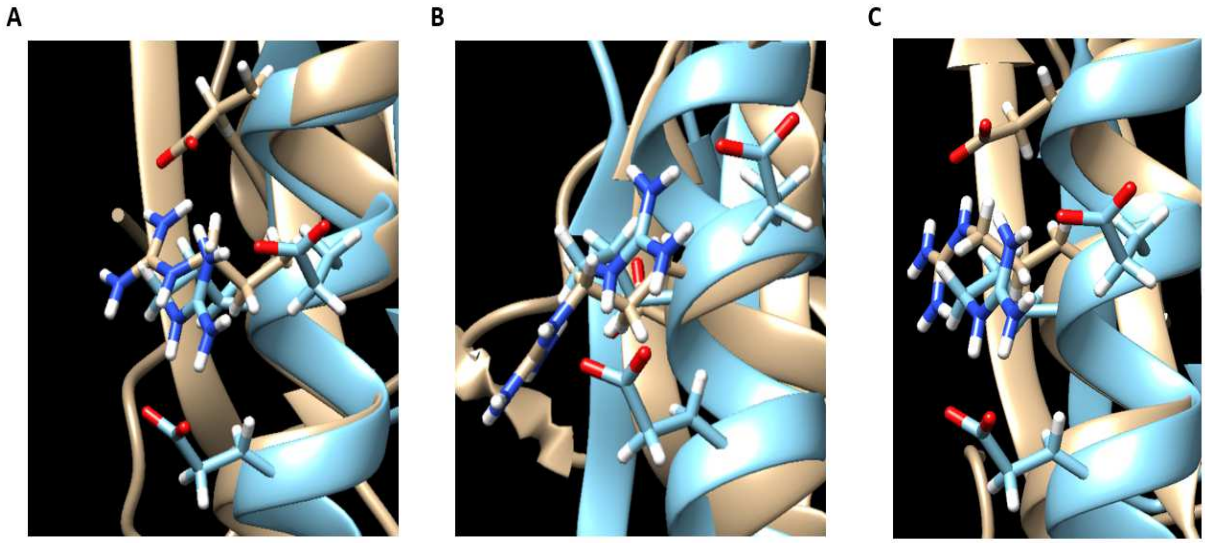

Figure 36. Comparison of the orientation of Arg291 in Dio3 to A) Arg156 of 1QQ2; B) Arg161 of 2P5R; C) Arg187 of 4KCE.

4.3 Conclusion

Conflicting viewpoints regarding dimerization of Dio3 have been ongoing in the literature. The structure of the dimer of the Dio3 catalytic domain was investigated using sequential and structural comparisons to other thioredoxin-fold proteins, protein-protein docking databases, and MD simulations. The conflicting hypotheses in the literature regarding the Dio3 dimer structure could be due to the observance of A-type and B-type dimers formed in Prx proteins. Sequential and structural comparisons of Dio with A-type and B-type proteins show B-type dimerization is preferable. Protein-protein docking databases SymmDock and GalaxyRefineComplex using the 2.0 μs structure of the $Dio3_{(C)}$-T_4 complex in a previous study produced a symmetric B-type dimer that contains a thioredoxin-fold. MD simulations of the constructed dimer show the protein remains stable in both the *apo* and *holo* forms, and removal of the T_4 substrates further stabilized the protein. These models could be employed for future studies regarding the role of dimerization in the deiodination mechanism. MMPBSA/MMGBSA analysis identified key interactions within the $\alpha_3\beta_4$ region of the dimerization interface. BB interactions between Met270-Gln272 are primarily responsible for holding the β-sheets together, while intramonomer and interdimer SC-SC

interactions of Arg291 with Glu residues of Arg291 hold the α-helices together. The interaction energies within the interfacial α-helices and β-sheets are similar in magnitude and are comparable to those of other B-type dimers. Mutation studies involving these residues could be performed to analyze their effects on dimer stability and catalytic function. Although MD simulations of the Dio3 dimer show a stable structure, they do not contain the tether region, which may contribute to overall stability and enzymatic deiodination. From the computational perspective, combining the findings of this study with experimental studies can further discern the full-length structure of Dio3, which will be imperative for treating thyroid-related illnesses.

4.4 Computational Methods

In the Dio3 monomer structure, the CHIMERA suite was used to straighten out the interfacial β-sheet by using the *set attr* function to set the dihedral angles to emulate those commonly found in β-sheets (φ=-120°, ψ=115°).[49,258] The resulting monomer was then saved as a pdb file to be submitted to the SymmDock server.[230] The server requires three input files; the monomer pdb file of the asymmetric unit, a "sites" file and a "constraints" file. The "sites" file specifies the range of residues in which the dimers will interact, while the "constraints" file specifies the distance constraints between pairs of atoms between both monomers within a certain range.[230] To best allow Dio3 to dimerize according to the B-type description, residues within the β-sheet at the interface region were included in the "sites" file (Thr268 to Gln272), and the distance between the midpoints of the β-sheets, Met270, were constrained to be between 0-7 Å. Finally, the symmetry order was set to 2 in only to consider dimer structures. Based upon the submitted structure, SymmDock produced 58 B-type dimers. GalaxyRefineComplex was used to resolve the close contacts at the interface of the best SymmDock-produced dimer by repacking the sidechain residues in a symmetric fashion.[251] GalaxyRefineComplex produced 10 structures as an output, creating three structures are high quality, two that were moderate, and five that were acceptable.

The AMBER 16 suite was used to run MD simulations using PMEDA GPU routines.[259] The *ff99sb* force field was used to represent the proteins used in this study. Parameters for the deprotonated

Sec force field, such as bond distances, charges, and force constants, were derived according to a previous study.[36] To ensure dimer stability, a slower approach was used during the NVT ensemble in which the constraints on the dimer interface are slowly released over time to allow the sidechains within the interface region to properly adjust. This slow approach advanced in the following steps; A) restraining the entire protein at a force constant of 50 kcal mol^{-1} $Å^{-2}$; B) reducing the constraints of the protein down from a force constant of 50 to 25 kcal mol^{-1} $Å^{-2}$; C) removing the constraints of the sidechains of the interfacial α-helices and β-sheets; D) removing the constraints of the interfacial α-helices and β-sheets entirely; E) removing the constraints of the sidechains remaining residues at the interface (i.e., the αβ-turn and C-terminal residues); F) removing the constraints of the remaining residues entirely; G) reducing the constraints of the protein down from a force constant of 25 to 10 kcal mol^{-1} $Å^{-2}$; H) reducing the constraints of the protein down from a force constant of 10 to 5 kcal mol^{-1} $Å^{-2}$; I) full release of the entire protein. Modules within the AmberTools suite were used to evaluate the energetics, the hydrophobic contacts, and key hydrogen bonding interactions within the protein.[70] MMPBSA/MMGBSA calculations were performed to quantify the energetic contributions of the dimer interface interactions throughout the MD simulations.[260]

CHAPTER 5

CONCLUSION

In this dissertation, *in silico* methods were used to model and evaluate XB interactions of known EDCs (PBDEs, PCBs) with a small model of the Dio3 active site and a homodimer of Dio3 was constructed based upon the recently isolated monomeric crystal structure. Small DFT models of halogenated EDCs with the $SeMe^-$ active site model show possible mechanisms of inhibition towards Dio. PBDEs and PCBs could inhibit Dio by forming an X—Se XB interaction to the Sec residue in the active site. XB favorability follows in the order of THs > PBDEs > PCBs, in agreement with larger halogens generally having stronger XB interactions (i.e. I > Br > Cl). THs readily undergo deiodination by deiodinases, with 3-T_1 being the only exception. 3-T_1 also displayed the weakest I—Se of the series in our DFT models. The inability for 3-T_1 to undergo deiodination suggests a possible energy threshold needs to be met for dehalogenation to occur. Some of the highly substituted PBDEs/OH-BDEs have similar interaction energies to THs and could debrominate. On the other hand, PCBs have much less favorable XB interactions, suggesting dechlorination of these compounds is unlikely. The position of the XB interaction (i.e. *ortho*, *meta, para*) plays a role in XB strength. For diphenyl ethers (PBDEs, THs), XB is preferred at the *ortho* and *meta* positions. The preferential dehalogenation positions of PBDEs (*ortho* and *meta*) and PCBs (*meta* and *para*) suggests these halogenated aromatics could target specific Dios that have preferred substrates with similar substitution patterns. Sequential and structural comparisons of Dio3 to known A-type and B-type proteins in tandem with protein-protein docking databases show B-type dimerization is most likely to occur in Dio3. A symmetric B-type dimer structure of Dio3 was constructed by SymmDock and its interfacial residues were refined by GalaxyRefineComplex. MD simulations of the constructed dimer show the protein remains stable in both the *apo* and *holo* forms. BB interactions within the β-sheets and intramonomer and interdimer SC-SC interactions within the α-helices hold the Dio3 dimeric structure together.

Moving forward, the computational findings in this dissertation regarding the small model XB interactions of PBDEs/PCBs and the structural and sequential data of Dio3 will aid endocrinal research. For example, MD simulations of the Dio3-PBDE/PCB complexes could show how these EDCs bind within the active site of Dio and how other external factors, such as ancillary XB interactions to amino acids within the active site or the Ω-loop, could influence substrate binding. Full-scale models and MD simulations of dimeric Dio3 that include the tether region and the membrane region can also be done to help discern if there are key residues within the tether region that help keep the dimeric structure together. Bioinformatic studies of Dio3 can include sequence comparisons to other known thioredoxin-fold proteins not covered in this dissertation to see if any amino acids and/or regions are conserved. Utilizing bioinformatics tools will be helpful for deriving the functions of residues and/or regions within Dio3. Finally, this research could spark interest in biochemists to help expand our understanding of Dio3 by performing *in vivo* experiments to verify the results found in this dissertation. Combining *in silico* and *in vivo* experiments of Dio3 will be vital in designing treatments for TH-related disorders caused by Dio proteins, which will be a crucial milestone for drug design.

REFERENCES

(1) Raju, T. N. The Nobel Chronicles. 1950: Edward Calvin Kendall (1886-1972); Philip Showalter Hench (1896-1965); and Tadeus Reichstein (1897-1996). *Lancet* **1999**, *353* (9161), 1370.

(2) Mondal, S.; Raja, K.; Schweizer, U.; Mugesh, G. Chemistry and Biology in the Biosynthesis and Action of Thyroid Hormones. *Angew. Chem. Int. Edit.* **2016**, *55* (27), 7606–7630.

(3) Bianco, A. C.; Salvatore, D.; Gereben, B.; Berry, M. J.; Larsen, P. R. Biochemistry, Cellular and Molecular Biology, and Physiological Roles of the Iodothyronine Selenodeiodinases. *Endocr. Rev.* **2002**, *23* (1), 38.

(4) Schweizer, U.; Steegborn, C. New Insights into the Structure and Mechanism of Iodothyronine Deiodinases. *J. Mol. Endocrinol.* **2015**, *55* (3), 37–52.

(5) Köhrle, J. The Colorful Diversity of Thyroid Hormone Metabolites. *Eur. Thyroid J.* **2019**, *8* (3), 115–129.

(6) Fekete, C.; Lechan, R. M. Negative Feedback Regulation of Hypophysiotropic Thyrotropin-Releasing Hormone (TRH) Synthesizing Neurons: Role of Neuronal Afferents and Type 2 Deiodinase. *Front. Neuroendocrinol.* **2007**, *28* (2–3), 97–114.

(7) Pilo, A.; Iervasi, G.; Vitek, F.; Ferdeghini, M.; Cazzuola, F.; Bianchi, R. Thyroidal and Peripheral Production of 3,5,3'-Triiodothyronine in Humans by Multicompartmental Analysis. *Am. J. Physiol.-Endoc. M.* **1990**, *258* (4), E715–E726.

(8) Shahid, M. A.; Ashraf, M. A.; Sharma, S. Physiology, Thyroid Hormone. In *StatPearls*; StatPearls Publishing: Treasure Island (FL), 2020.

(9) Núñez, A.; Bedregal, P.; Becerra, C.; Grob L, F. Neurodevelopmental assessment of patients with congenital hypothyroidism. *Rev. Med. Chil.* **2017**, *145* (12), 1579–1587.

(10) Sorisky, A. Subclinical Hypothyroidism – What Is Responsible for Its Association with Cardiovascular Disease? *Eur. Endocrinol.* **2016**, *12* (2), 96–98.

(11) Devereaux, D.; Tewelde, S. Z. Hyperthyroidism and Thyrotoxicosis. *Emerg. Med. Clin. N. Am.* **2014**, *32* (2), 277–292.

(12) Escobar-Morreale, H. F.; Botella-Carretero, J. I.; Gómez-Bueno, M.; Galán, J. M.; Barrios, V.; Sancho, J. Thyroid Hormone Replacement Therapy in Primary Hypothyroidism: A Randomized Trial Comparing L-Thyroxine plus Liothyronine with L-Thyroxine Alone. *Ann. Intern. Med.* **2005**, *142* (6), 412–424.

(13) Jonklaas, J.; Bianco, A. C.; Bauer, A. J.; Burman, K. D.; Cappola, A. R.; Celi, F. S.; Cooper, D. S.; Kim, B. W.; Peeters, R. P.; Rosenthal, M. S.; Sawka, A. M.; American Thyroid Association Task Force on Thyroid Hormone Replacement. Guidelines for the Treatment of Hypothyroidism: Prepared by the American Thyroid Association Task Force on Thyroid Hormone Replacement. *Thyroid* **2014**, *24* (12), 1670–1751.

(14) Eber, O.; Buchinger, W.; Lindner, W.; Rath, P., Monika Lind; Klima, G.; Langsteger, W.; Kõltringer, P. The Effect of D- Versus L- Propranolol in the Treatment of Hyperthyroidism. *Clin. Endocrinol.* **1990**, *32* (3), 363–372.

(15) Metso, S.; Auvinen, A.; Huhtala, H.; Salmi, J.; Oksala, H.; Jaatinen, P. Increased Cancer Incidence after Radioiodine Treatment for Hyperthyroidism. *Cancer* **2007**, *109* (10), 1972–1979.

(16) Ekholm, R. Biosynthesis of Thyroid Hormones. In *International Review of Cytology*; Jeon, K. W., Friedlander, M., Eds.; Academic Press, 1990; Vol. 120, pp 243–288.

(17) Lechan, R. M.; Fekete, C. Feedback Regulation of Thyrotropin-Releasing Hormone (TRH): Mechanisms for the Non-Thyroidal Illness Syndrome. *J. Endocrinol. Invest.* **2004**, *27* (6), 105–119.

(18) Carrasco, N. Iodide Transport in the Thyroid Gland. *Biochim. Biophys. Acta.* **1993**, *1154* (1), 65–82.

(19) Kimura, S.; Ikeda□Saito, M. Human Myeloperoxidase and Thyroid Peroxidase, Two Enzymes with Separate and Distinct Physiological Functions, Are Evolutionarily Related Members of the Same Gene Family. *Pr. Struct. Funct. Bioinformat.* **1988**, *3* (2), 113–120.
(20) Bénard, B.; Brault, J. Production of peroxide in the thyroid. *Union Med. Can.* **1971**, *100* (4), 701–705.
(21) Wu, S.; Green, W. L.; Huang, W.; Hays, M. T.; Chopra, I. J. Alternate Pathways of Thyroid Hormone Metabolism. *Thyroid* **2005**, *15* (8), 943–958.
(22) Wu, S.; Visser, T. *Thyroid Hormone Metabolism Molecular Biology and Alternate Pathways*; CRC Press: Boca Raton (FL), 1994.
(23) Scanlan, T. S.; Suchland, K. L.; Hart, M. E.; Chiellini, G.; Huang, Y.; Kruzich, P. J.; Frascarelli, S.; Crossley, D. A.; Bunzow, J. R.; Ronca-Testoni, S.; Lin, E. T.; Hatton, D.; Zucchi, R.; Grandy, D. K. 3-Iodothyronamine Is an Endogenous and Rapid-Acting Derivative of Thyroid Hormone. *Nat. Med.* **2004**, *10* (6), 638–642.
(24) Wood, W. J. L.; Geraci, T.; Nilsen, A.; DeBarber, A. E.; Scanlan, T. S. Iodothyronamines Are Oxidatively Deaminated to Iodothyroacetic Acids in Vivo. *ChemBioChem* **2009**, *10* (2), 361–365.
(25) Lindemann, L.; Meyer, C. A.; Jeanneau, K.; Bradaia, A.; Ozmen, L.; Bluethmann, H.; Bettler, B.; Wettstein, J. G.; Borroni, E.; Moreau, J.-L.; Hoener, M. C. Trace Amine-Associated Receptor 1 Modulates Dopaminergic Activity. *J. Pharmacol. Exp. Ther.* **2008**, *324* (3), 948–956.
(26) Wolinsky, T. D.; Swanson, C. J.; Smith, K. E.; Zhong, H.; Borowsky, B.; Seeman, P.; Branchek, T.; Gerald, C. P. The Trace Amine 1 Receptor Knockout Mouse: An Animal Model with Relevance to Schizophrenia. *Genes Brain Behav.* **2007**, *6* (7), 628–639.
(27) Lindemann, L.; Hoener, M. C. A Renaissance in Trace Amines Inspired by a Novel GPCR Family. *Trends Pharmacol. Sci.* **2005**, *26* (5), 274–281.
(28) Everts, M. E.; Visser, T. J.; Moerings, E. P.; Docter, R.; van Toor, H.; Tempelaars, A. M.; de Jong, M.; Krenning, E. P.; Hennemann, G. Uptake of Triiodothyroacetic Acid and Its Effect on Thyrotropin Secretion in Cultured Anterior Pituitary Cells. *Endocrinology* **1994**, *135* (6), 2700–2707.
(29) St. Germain, D. L.; Galton, V. A.; Hernandez, A. Defining the Roles of the Iodothyronine Deiodinases: Current Concepts and Challenges. *Endocrinology* **2009**, *150* (3), 1097–1107.
(30) St. Germain, D. L. Selenium, Deiodinases and Endocrine Function. In *Selenium: Its Molecular Biology and Role in Human Health*; Hatfield, D. L., Ed.; Springer US: Boston, MA, 2001; pp 189–202.
(31) Kuiper, G. G. J. M.; Klootwijk, W.; Visser, T. J. Substitution of Cysteine for Selenocysteine in the Catalytic Center of Type III Iodothyronine Deiodinase Reduces Catalytic Efficiency and Alters Substrate Preference. *Endocrinology* **2003**, *144* (6), 2505–2513.
(32) Galton, V. A. The Roles of the Iodothyronine Deiodinases in Mammalian Development. *Thyroid* **2005**, *15* (8), 823–834.
(33) Huang, S. A.; Tu, H. M.; Harney, J. W.; Venihaki, M.; Butte, A. J.; Kozakewich, H. P. W.; Fishman, S. J.; Larsen, P. R. Severe Hypothyroidism Caused by Type 3 Iodothyronine Deiodinase in Infantile Hemangiomas. *New. Eng. J. Med.* **2000**, *343* (3), 185–189.
(34) Weber Pasa, M.; Selbach Scheffel, R.; Borsatto Zanella, A.; Maia, A. L.; Dora, J. M. Consumptive Hypothyroidism: Case Report of Hepatic Hemangioendotheliomas Successfully Treated with Vincristine and Systematic Review of the Syndrome. *Eur. Thyroid J.* **2017**, *6* (6), 321–327.
(35) Schweizer, U.; Schlicker, C.; Braun, D.; Köhrle, J.; Steegborn, C. Crystal Structure of Mammalian Selenocysteine-Dependent Iodothyronine Deiodinase Suggests a Peroxiredoxin-like Catalytic Mechanism. *P. Natl. A. Sci. USA* **2014**, *111* (29), 10526–10531.
(36) Bayse, C. A.; Marsan, E. S.; Garcia, J. R.; Tran-Thompson, A. T. Thyroxine Binding to Type III Iodothyronine Deiodinase. *Sci. Rep.* **2020**, *10* (1), 15401.
(37) Bayse, C. A.; Rafferty, E. R. Is Halogen Bonding the Basis for Iodothyronine Deiodinase Activity? *Inorg. Chem.* **2010**, *49* (12), 5365–5367.

(38) Manna, D.; Mugesh, G. Regioselective Deiodination of Thyroxine by Iodothyronine Deiodinase Mimics: An Unusual Mechanistic Pathway Involving Cooperative Chalcogen and Halogen Bonding. *J. Am. Chem. Soc.* **2012**, *134* (9), 4269–4279.
(39) Marsan, E. S.; Bayse, C. A. Halogen-Bonding Interactions of Polybrominated Diphenyl Ethers and Thyroid Hormone Derivatives: A Potential Mechanism for the Inhibition of Iodothyronine Deiodinase. *Chem. Eur. J.* **2017**, *23* (27), 6625–6633.
(40) Marsan, E. S.; Bayse, C. A. Halogen Bonding Interactions of Polychlorinated Biphenyls and the Potential for Thyroid Disruption. *Chem. Eur. J.* **2020**, *26*, 1–9.
(41) Curtis, S. W.; Terrell, M. L.; Jacobson, M. H.; Cobb, D. O.; Jiang, V. S.; Neblett, M. F.; Gerkowicz, S. A.; Spencer, J. B.; Marder, M. E.; Barr, D. B.; Conneely, K. N.; Smith, A. K.; Marcus, M. Thyroid Hormone Levels Associate with Exposure to Polychlorinated Biphenyls and Polybrominated Biphenyls in Adults Exposed as Children. *Environ. Health* **2019**, *18* (1), 75.
(42) Curtis Jr., I. *USA v. Robert J. Massey*; 2020.
(43) Kato, Y.; Ikushiro, S.; Haraguchi, K.; Yamazaki, T.; Ito, Y.; Suzuki, H.; Kimura, R.; Yamada, S.; Inoue, T.; Degawa, M. A Possible Mechanism for Decrease in Serum Thyroxine Level by Polychlorinated Biphenyls in Wistar and Gunn Rats. *Toxicol. Sci.* **2004**, *81* (2), 309–315.
(44) Schnitzler, J. G.; Celis, N.; Klaren, P. H. M.; Blust, R.; Dirtu, A. C.; Covaci, A.; Das, K. Thyroid Dysfunction in Sea Bass (Dicentrarchus Labrax): Underlying Mechanisms and Effects of Polychlorinated Biphenyls on Thyroid Hormone Physiology and Metabolism. *Aquat. Toxicol.* **2011**, *105* (3), 438–447.
(45) Roberts, S. C.; Bianco, A. C.; Stapleton, H. M. Disruption of Type 2 Iodothyronine Deiodinase Activity in Cultured Human Glial Cells by Polybrominated Diphenyl Ethers. *Chem. Res. Toxicol.* **2015**, *28* (6), 1265–1274.
(46) Sagar, G. D. V.; Gereben, B.; Callebaut, I.; Mornon, J.-P.; Zeöld, A.; Curcio-Morelli, C.; Harney, J. W.; Luongo, C.; Mulcahey, M. A.; Larsen, P. R.; Huang, S. A.; Bianco, A. C. The Thyroid Hormone-Inactivating Deiodinase Functions as a Homodimer. *Mol. Endocrinol.* **2008**, *22* (6), 1382–1393.
(47) Sagar, G. D. V.; Gereben, B.; Callebaut, I.; Mornon, J.-P.; Zeöld, A.; Silva, W. S. da; Luongo, C.; Dentice, M.; Tente, S. M.; Freitas, B. C. G.; Harney, J. W.; Zavacki, A. M.; Bianco, A. C. Ubiquitination-Induced Conformational Change within the Deiodinase Dimer Is a Switch Regulating Enzyme Activity. *Mol. Cell. Biol.* **2007**, *27* (13), 4774–4783.
(48) Humphrey, W.; Dalke, A.; Schulten, K. VMD: Visual Molecular Dynamics. *J. Mol. Graphics* **1996**, *14* (1), 33–38.
(49) Pettersen, E. F.; Goddard, T. D.; Huang, C. C.; Couch, G. S.; Greenblatt, D. M.; Meng, E. C.; Ferrin, T. E. UCSF Chimera--a Visualization System for Exploratory Research and Analysis. *J. Comput. Chem.* **2004**, *25* (13), 1605–1612.
(50) The PyMOL Molecular Graphics System, Version 2.0 Schrödinger, LLC.
(51) Ekins, S.; Mestres, J.; Testa, B. In Silico Pharmacology for Drug Discovery: Applications to Targets and Beyond. *Br. J. Pharmacol.* **2007**, *152* (1), 21–37.
(52) Saeidnia, S.; Manayi, A.; Abdollahi, M. The Pros and Cons of the In-Silico Pharmaco-Toxicology in Drug Discovery and Development. *Int. J. Pharmacol.* **2013**, *9* (3), 176–181.
(53) Hohenberg, P.; Kohn, W. Inhomogeneous Electron Gas. *Phys. Rev.* **1964**, *136* (3B), B864–B871.
(54) Thomas, L. H. The Calculation of Atomic Fields. *Math. Proc. Cambridge* **1927**, *23* (5), 542–548.
(55) Reed, A. E.; Curtiss, L. A.; Weinhold, F. Intermolecular Interactions from a Natural Bond Orbital, Donor-Acceptor Viewpoint. *Chem. Rev.* **1988**, *88* (6), 899–926.
(56) Rives, A. B.; Weinhold, F. Natural Hybrid Orbitals: Ab Initio SCF and CI Results for CO and NiCO. *Int. J. Quantum Chem.* **1980**, *18* (S14), 201–209.
(57) Frisch, M.; Trucks, G.; Schlegel, H.; Scuseria, G.; Robb, M.; Cheeseman, J.; Scalmani, G.; Barone, V.; Mennucci, B.; Petersson, G.; Nakatsuji, H.; Caricato, M.; Li, X.; Hratchian, H.; Izmaylov, A.; Bloino, J.; Zheng, G.; Sonnenberg, J.; Hada, M.; Ehara, M.; Toyota, K.; Fukuda, R.; Hasegawa, J.; Ishida, M.; Nakajima, T.; Honda, Y.; Kitao, O.; Nakai, H.; Vreven, T.;

Montgomery, J.; Peralta, J.; Ogliaro, F.; Bearpark, M.; Heyd, J.; Brothers, E.; Kudin, K.; Staroverov, V.; Kobayashi, R.; Normand, J.; Raghavachari, K.; Rendell, A.; Burant, J.; Iyengar, S.; Tomasi, J.; Cossi, M.; Rega, N.; Millam, J.; Klene, M.; Knox, J.; Cross, J.; Bakken, V.; Adamo, C.; Jaramillo, J.; Gomperts, R.; Stratmann, R.; Yazyev, O.; Austin, A.; Cammi, R.; Pomelli, C.; Ochterski, J.; Martin, R.; Morokuma, K.; Zakrzewski, V.; Voth, G.; Salvador, P.; Dannenberg, J.; Dapprich, S.; Daniels, A.; Farkas; Foresman, J.; Ortiz, J.; Cioslowski, J.; Fox, D. Gaussian 09, Revision B.01. *Gaussian 09, Revision B.01, Gaussian, Inc., Wallingford CT* **2009**.

(58) Zhao, Y.; Truhlar, D. G. The M06 Suite of Density Functionals for Main Group Thermochemistry, Thermochemical Kinetics, Noncovalent Interactions, Excited States, and Transition Elements: Two New Functionals and Systematic Testing of Four M06-Class Functionals and 12 Other Functionals. *Theor. Chem. Acc.* **2008**, *120* (1), 215–241.

(59) McCammon, J. A.; Gelin, B. R.; Karplus, M. Dynamics of Folded Proteins. *Nature* **1977**, *267* (5612), 585–590.

(60) Jones, J. E.; Chapman, S. On the Determination of Molecular Fields. —II. From the Equation of State of a Gas. *P. R. Soc. Lond. A.-Conta.* **1924**, *106* (738), 463–477.

(61) Durrant, J. D.; McCammon, J. A. Molecular Dynamics Simulations and Drug Discovery. *BMC Biology* **2011**, *9* (1), 71.

(62) Foloppe, N.; Jr, A. D. M. All-Atom Empirical Force Field for Nucleic Acids: I. Parameter Optimization Based on Small Molecule and Condensed Phase Macromolecular Target Data. *J. Comput. Chem.* **2000**, *21* (2), 86–104.

(63) Brooks, B. R.; Bruccoleri, R. E.; Olafson, B. D.; States, D. J.; Swaminathan, S.; Karplus, M. CHARMM: A Program for Macromolecular Energy, Minimization, and Dynamics Calculations. *J. Comput. Chem.* **1983**, *4* (2), 187–217.

(64) Christen, M.; Hünenberger, P. H.; Bakowies, D.; Baron, R.; Bürgi, R.; Geerke, D. P.; Heinz, T. N.; Kastenholz, M. A.; Kräutler, V.; Oostenbrink, C.; Peter, C.; Trzesniak, D.; Gunsteren, W. F. van. The GROMOS Software for Biomolecular Simulation: GROMOS05. *J. Comput. Chem.* **2005**, *26* (16), 1719–1751.

(65) Oostenbrink, C.; Villa, A.; Mark, A. E.; van Gunsteren, W. F. A Biomolecular Force Field Based on the Free Enthalpy of Hydration and Solvation: The GROMOS Force-Field Parameter Sets 53A5 and 53A6. *J. Comput. Chem.* **2004**, *25* (13), 1656–1676.

(66) Cornell, W. D.; Cieplak, P.; Bayly, C. I.; Gould, I. R.; Merz, K. M.; Ferguson, D. M.; Spellmeyer, D. C.; Fox, T.; Caldwell, J. W.; Kollman, P. A. A Second Generation Force Field for the Simulation of Proteins, Nucleic Acids, and Organic Molecules. *J. Am. Chem. Soc.* **1995**, *117* (19), 5179–5197.

(67) Wang, J.; Wolf, R. M.; Caldwell, J. W.; Kollman, P. A.; Case, D. A. Development and Testing of a General Amber Force Field. *J. Comput. Chem.* **2004**, *25* (9), 1157–1174.

(68) Duan, Y.; Wu, C.; Chowdhury, S.; Lee, M. C.; Xiong, G.; Zhang, W.; Yang, R.; Cieplak, P.; Luo, R.; Lee, T.; Caldwell, J.; Wang, J.; Kollman, P. A Point-Charge Force Field for Molecular Mechanics Simulations of Proteins Based on Condensed-Phase Quantum Mechanical Calculations. *J. Comput. Chem.* **2003**, *24* (16), 1999–2012.

(69) Kollman, P. A. Advances and Continuing Challenges in Achieving Realistic and Predictive Simulations of the Properties of Organic and Biological Molecules. *Acc. Chem. Res.* **1996**, *29* (10), 461–469.

(70) Roe, D. R.; Cheatham, T. E. PTRAJ and CPPTRAJ: Software for Processing and Analysis of Molecular Dynamics Trajectory Data. *J. Chem. Theory Comput.* **2013**, *9* (7), 3084–3095.

(71) Gentile, F.; Lauro R., D.; Salvatore, G. *Biosynthesis and Secretion of Thyroid Hormones*; W.B. Saunders Company: Philadelphia, PA, 1995.

(72) Brent, G. A. Mechanisms of Thyroid Hormone Action. *J. Endocrinol. Invest.* **2012**, *122* (9), 3035–3043.

(73) Rubio, I. G.; Medeiros-Neto, G. Mutations of the Thyroglobulin Gene and Its Relevance to Thyroid Disorders. *Curr. Opin. Endocrinol.* **2009**, *16* (5), 373–378.

(74) Zimmermann, M. B. Iodine Deficiency. *Endocr. Rev.* **2009**, *30* (4), 376–408.
(75) Parmentier, M.; Libert, F.; Maenhaut, C.; Lefort, A.; Gerard, C.; Perret, J.; Van Sande, J.; Dumont, J.; Vassart, G. Molecular Cloning of the Thyrotropin Receptor. *Science* **1989**, *246* (4937), 1620–1622.
(76) Kunisue, T.; Fisher, J. W.; Kannan, K. Determination of Six Thyroid Hormones in the Brain and Thyroid Gland Using Isotope-Dilution Liquid Chromatography/Tandem Mass Spectrometry. *Anal. Chem.* **2011**, *83* (1), 417–424.
(77) Guyton, A. C.; Hall, J. E. *Guyton and Hall Textbook of Medical Physiology - 12th Edition*; Saunders/Elsevier: Philadelphia, PA, 2011.
(78) Bianco, A. C.; Kim, B. W. Deiodinases: Implications of the Local Control of Thyroid Hormone Action. *J. Clin. Invest.* **2006**, *116* (10), 2571–2579.
(79) Köhrle, J. Iodothyronine Deiodinases. *Meth. Enzymol.* **2002**, *347*, 125–167.
(80) Orozco, A.; Navarrete-Ramírez, P.; Olvera, A.; García-G, C. 3,5-Diiodothyronine (T_2) Is on a Role. A New Hormone in Search of Recognition. *Gen. Comp. Endocr.* **2014**, *203*, 174–180.
(81) Padron, A. S.; Neto, R. A. L.; Pantaleão, T. U.; de Souza dos Santos, M. C.; Araujo, R. L.; de Andrade, B. M.; da Silva Leandro, M.; de Castro, J. P. S. W.; Ferreira, A. C. F.; de Carvalho, D. P. Administration of 3,5-Diiodothyronine (3,5-T2) Causes Central Hypothyroidism and Stimulates Thyroid-Sensitive Tissues. *J. Endocrinol.* **2014**, *221* (3), 415–427.
(82) Zhang, J.; Li, Y.; Gupta, A. A.; Nam, K.; Andersson, P. L. Identification and Molecular Interaction Studies of Thyroid Hormone Receptor Disruptors among Household Dust Contaminants. *Chem. Res. Toxicol.* **2016**, *29* (8), 1345–1354.
(83) Dratman, M. B.; Gordon, J. T. Thyroid Hormones As Neurotransmitters. *Thyroid* **1996**, *6* (6), 639–647.
(84) Kirkegaard, C.; Faber, J. The Role of Thyroid Hormones in Depression. *Eur. J. Endocrinol.* **1998**, *138* (1), 1–9.
(85) Szinnai, G. Genetics of Normal and Abnormal Thyroid Development in Humans. *Best Pract. Res. Clin. Endocrinol. Metab.* **2014**, *28* (2), 133–150.
(86) Ji, K.; Choi, K.; Giesy, J. P.; Musarrat, J.; Takeda, S. Genotoxicity of Several Polybrominated Diphenyl Ethers (PBDEs) and Hydroxylated PBDEs, and Their Mechanisms of Toxicity. *Environ. Sci. Technol.* **2011**, *45* (11), 5003–5008.
(87) Préau, L.; Fini, J. B.; Morvan-Dubois, G.; Demeneix, B. Thyroid Hormone Signaling during Early Neurogenesis and Its Significance as a Vulnerable Window for Endocrine Disruption. *Biochim. Biophys. Acta* **2015**, *1849* (2), 112–121.
(88) Kojima, H.; Takeuchi, S.; Uramaru, N.; Sugihara, K.; Yoshida, T.; Kitamura, S. Nuclear Hormone Receptor Activity of Polybrominated Diphenyl Ethers and Their Hydroxylated and Methoxylated Metabolites in Transactivation Assays Using Chinese Hamster Ovary Cells. *Environ. Health Perspect.* **2009**, *117* (8), 1210–1218.
(89) Stapleton, H. M.; Kelly, S. M.; Pei, R.; Letcher, R. J.; Gunsch, C. Metabolism of Polybrominated Diphenyl Ethers (PBDEs) by Human Hepatocytes in Vitro. *Environ. Health Perspect.* **2009**, *117* (2), 197–202.
(90) Alaee, M.; Arias, P.; Sjödin, A.; Bergman, A. An Overview of Commercially Used Brominated Flame Retardants, Their Applications, Their Use Patterns in Different Countries/Regions and Possible Modes of Release. *Environ. Int.* **2003**, *29* (6), 683–689.
(91) Stapleton, H. M.; Sjödin, A.; Jones, R. S.; Niehüser, S.; Zhang, Y.; Patterson, D. G. Serum Levels of Polybrominated Diphenyl Ethers (PBDEs) in Foam Recyclers and Carpet Installers Working in the United States. *Environ. Sci. Technol.* **2008**, *42* (9), 3453–3458.
(92) Mazdai, A.; Dodder, N. G.; Abernathy, M. P.; Hites, R. A.; Bigsby, R. M. Polybrominated Diphenyl Ethers in Maternal and Fetal Blood Samples. *Environ. Health Perspect.* **2003**, *111* (9), 1249–1252.
(93) Costa, L. G.; Giordano, G. Developmental Neurotoxicity of Polybrominated Diphenyl Ether (PBDE) Flame Retardants. *Neurotoxicology* **2007**, *28* (6), 1047–1067.

(94) Meerts, I. A. T. M.; van Zanden, J. J.; Luijks, E. A. C.; van Leeuwen-Bol, I.; Marsh, G.; Jakobsson, E.; Bergman, Å.; Brouwer, A. Potent Competitive Interactions of Some Brominated Flame Retardants and Related Compounds with Human Transthyretin in Vitro. *Toxicol. Sci.* **2000**, *56* (1), 95–104.
(95) Hamers, T.; Kamstra, J. H.; Sonneveld, E.; Murk, A. J.; Kester, M. H. A.; Andersson, P. L.; Legler, J.; Brouwer, A. In Vitro Profiling of the Endocrine-Disrupting Potency of Brominated Flame Retardants. *Toxicol. Sci.* **2006**, *92* (1), 157–173.
(96) Roberts, S. C.; Noyes, P. D.; Gallagher, E. P.; Stapleton, H. M. Species-Specific Differences and Structure−Activity Relationships in the Debromination of PBDE Congeners in Three Fish Species. *Environ. Sci. Technol.* **2011**, *45* (5), 1999–2005.
(97) *Report of the Persistent Organic Pollutants Review Committee*; United Nations, 2006.
(98) Siddiqi, M. A.; Laessig, R. H.; Reed, K. D. Polybrominated Diphenyl Ethers (PBDEs): New Pollutants–Old Diseases. *Clin. Med. Res.* **2003**, *1* (4), 281–290.
(99) Darnerud, P. O.; Eriksen, G. S.; Jóhannesson, T.; Larsen, P. B.; Viluksela, M. Polybrominated Diphenyl Ethers: Occurrence, Dietary Exposure, and Toxicology. *Environ. Health Perspect.* **2001**, *109* (1), 49–68.
(100) Kierkegaard, A.; Balk, L.; Tjärnlund, U.; de Wit, C. A.; Jansson, B. Dietary Uptake and Biological Effects of Decabromodiphenyl Ether in Rainbow Trout (Oncorhynchus Mykiss). *Environ. Sci. Technol.* **1999**, *33* (10), 1612–1617.
(101) Kem, I. *Phase-out of PBDEs and PBBs: Report on a Governmental Commission.*; 2/99; Solna, Sweden, 1999.
(102) Politzer, P.; Lane, P.; Concha, M. C.; Ma, Y.; Murray, J. S. An Overview of Halogen Bonding. *J. Mol. Model.* **2007**, *13* (2), 305–311.
(103) Cavallo, G.; Metrangolo, P.; Milani, R.; Pilati, T.; Priimagi, A.; Resnati, G.; Terraneo, G. The Halogen Bond. *Chem. Rev.* **2016**, *116* (4), 2478–2601.
(104) Clark, T.; Hennemann, M.; Murray, J. S.; Politzer, P. Halogen Bonding: The σ-Hole. *J. Mol. Model.* **2007**, *13* (2), 291–296.
(105) Manca, G.; Ienco, A.; Mealli, C. Factors Controlling Asymmetrization of the Simplest Linear I_3^- and I_4^{2-} Polyiodides with Implications for the Nature of Halogen Bonding. *Cryst. Growth Des.* **2012**, *12* (4), 1762–1771.
(106) Wolters, L. P.; Bickelhaupt, F. M. Halogen Bonding versus Hydrogen Bonding: A Molecular Orbital Perspective. *ChemistryOpen* **2012**, *1* (2), 96–105.
(107) Sorimachi, K.; Cahnmann, H. J. Formation and Metabolism of 3',5'-Diiodothyronine and 3,5-Diiodothyronine by Cultured Monkey Hepatocarcinoma Cells. *Horm. Metab. Res.* **1979**, *11* (3), 233—237.
(108) Manna, D.; Mondal, S.; Mugesh, G. Halogen Bonding Controls the Regioselectivity of the Deiodination of Thyroid Hormones and Their Sulfate Analogues. *Chem. Eur. J.* **2015**, *21* (6), 2409–2416.
(109) Manna, D.; Mugesh, G. A Chemical Model for the Inner-Ring Deiodination of Thyroxine by Iodothyronine Deiodinase. *Angew. Chem. Int. Edit.* **2010**, *49* (48), 9246–9249.
(110) Wang, W.; Hobza, P. Origin of the X−Hal (Hal = Cl, Br) Bond-Length Change in the Halogen-Bonded Complexes. *J. Phys. Chem. A* **2008**, *112* (17), 4114–4119.
(111) Mondal, S.; Mugesh, G. Regioselective Deiodination of Iodothyronamines, Endogenous Thyroid Hormone Derivatives, by Deiodinase Mimics. *Chem. Eur. J.* **2014**, *20* (35), 11120–11128.
(112) Renko, K.; Hoefig, C. S.; Hiller, F.; Schomburg, L.; Köhrle, J. Identification of Iopanoic Acid as Substrate of Type 1 Deiodinase by a Novel Nonradioactive Iodide-Release Assay. *Endocrinology* **2012**, *153* (5), 2506.
(113) Felicetta, J. V.; Green, W. L.; Nelp, W. B. Inhibition of Hepatic Binding of Thyroxine by Cholecystographic Agents. *J. Clin. Invest.* **1980**, *65* (5), 1032–1040.

(114) Yu, H.; Wondrousch, D.; Li, F.; Chen, J.; Lin, H.; Ji, L. In Silico Investigation of the Thyroid Hormone Activity of Hydroxylated Polybrominated Diphenyl Ethers. *Chem. Res. Toxicol.* **2015**, *28* (8), 1538–1545.
(115) Noyes, P. D.; Hinton, D. E.; Stapleton, H. M. Accumulation and Debromination of Decabromodiphenyl Ether (BDE-209) in Juvenile Fathead Minnows (Pimephales Promelas) Induces Thyroid Disruption and Liver Alterations. *Toxicol. Sci.* **2011**, *122* (2), 265–274.
(116) Ren, X.-M.; Guo, L.-H. Molecular Toxicology of Polybrominated Diphenyl Ethers: Nuclear Hormone Receptor Mediated Pathways. *Environ. Sci.-Proc. Imp.* **2013**, *15* (4), 702–708.
(117) Butt, C. M.; Stapleton, H. M. Inhibition of Thyroid Hormone Sulfotransferase Activity by Brominated Flame Retardants and Halogenated Phenolics. *Chem. Res. Toxicol.* **2013**, *26* (11), 1692–1702.
(118) Butt, C. M.; Wang, D.; Stapleton, H. M. Halogenated Phenolic Contaminants Inhibit the In Vitro Activity of the Thyroid-Regulating Deiodinases in Human Liver. *Toxicol. Sci.* **2011**, *124* (2), 339–347.
(119) Adamo, C.; Heitzmann, M.; Meilleur, F.; Rega, N.; Scalmani, G.; Grand, A.; Cadet, J.; Barone, V. Interplay of Intrinsic and Environmental Effects on the Magnetic Properties of Free Radicals Issuing from H-Atom Addition to Cytosine. *J. Am. Chem. Soc.* **2001**, *123* (29), 7113–7117.
(120) Dunning, T. H. Gaussian Basis Sets for Use in Correlated Molecular Calculations. I. The Atoms Boron through Neon and Hydrogen. *J. Chem. Phys.* **1989**, *90* (2), 1007–1023.
(121) Hurley, M. M.; Pacios, L. F.; Christiansen, P. A.; Ross, R. B.; Ermler, W. C. Ab Initio Relativistic Effective Potentials with Spin□orbit Operators. II. K through Kr. *J. Chem. Phys.* **1986**, *84* (12), 6840–6853.
(122) Hay, P. J.; Wadt, W. R. Ab Initio Effective Core Potentials for Molecular Calculations. Potentials for K to Au Including the Outermost Core Orbitals. *J. Chem. Phys.* **1985**, *82* (1), 299–310.
(123) Rossberg, M.; Lendle, W.; Pfleiderer, G.; Tögel, A.; Dreher, E.-L.; Langer, E.; Rassaerts, H.; Kleinschmidt, P.; Strack, H.; Cook, R.; Beck, U.; Lipper, K.-A.; Torkelson, T. R.; Löser, E.; Beutel, K. K.; Mann, T. Chlorinated Hydrocarbons. In *Ullmann's Encyclopedia of Industrial Chemistry*; Wiley-VCH Verlag GmbH & Co. KGaA, 2000.
(124) Mughal, B. B.; Fini, J.-B.; Demeneix, B. A. Thyroid-Disrupting Chemicals and Brain Development: An Update. *Endocrin. Connect.* **2018**, *7* (4), R160–R186.
(125) van den Berg, M.; Kypke, K.; Kotz, A.; Tritscher, A.; Lee, S. Y.; Magulova, K.; Fiedler, H.; Malisch, R. WHO/UNEP Global Surveys of PCDDs, PCDFs, PCBs and DDTs in Human Milk and Benefit–Risk Evaluation of Breastfeeding. *Arch. Toxicol.* **2017**, *91* (1), 83–96.
(126) Brouwer, A.; Morse, D. C.; Lans, M. C.; Gerlienke Schuur, A.; Murk, A. J.; Klasson-Wehler, E.; Bergman, Å.; Visser, T. J. Interactions of Persistent Environmental Organohalogens With the Thyroid Hormone System: Mechanisms and Possible Consequences for Animal and Human Health. *Toxicol. Ind. Health* **1998**, *14* (1–2), 59–84.
(127) Granby, K.; Rainieri, S.; Rasmussen, R. R.; Kotterman, M. J. J.; Sloth, J. J.; Cederberg, T. L.; Barranco, A.; Marques, A.; Larsen, B. K. The Influence of Microplastics and Halogenated Contaminants in Feed on Toxicokinetics and Gene Expression in European Seabass (Dicentrarchus Labrax). *Environ. Research* **2018**, *164*, 430–443.
(128) Hale, R. C. Are the Risks from Microplastics Truly Trivial? *Environ. Sci. Technol.* **2018**, *52* (3), 931–931.
(129) Pearce, E. N.; Braverman, L. E. Environmental Pollutants and the Thyroid. *Best Pract. Res. Cl. En.* **2009**, *23* (6), 801–813.
(130) Oliveira, K. J.; Chiamolera, M. I.; Giannocco G.; Pazos-Moura, C. C.; Ortiga-Carvalho, T. M. Thyroid Function Disruptors: From Nature to Chemicals. *J. Mol. Endocrinol.* **2019**, *62* (1), R1–R19.
(131) Zoeller, R. T. Environmental Chemicals as Thyroid Hormone Analogues: New Studies Indicate That Thyroid Hormone Receptors Are Targets of Industrial Chemicals? *Mol. Cell. Endocrinol.* **2005**, *242* (1), 10–15.

(132) Guo, L.-C.; Yu, S.; Wu, D.; Huang, J.; Liu, T.; Xiao, J.; Huang, W.; Gao, Y.; Li, X.; Zeng, W.; Rutherford, S.; Ma, W.; Zhang, Y.; Lin, L. Disruption of Thyroid Hormone Regulated Proteins and Gene Expression by Polychlorinated Biphenyls, Polybrominated Diphenyl Ethers and New Flame Retardants in Residents of an e-Waste Region. *Environ. Pollut.* **2019**, 112925.

(133) Verner, M.-A.; Plusquellec, P.; Desjardins, J. L.; Cartier, C.; Haddad, S.; Ayotte, P.; Dewailly, É.; Muckle, G. Prenatal and Early-Life Polychlorinated Biphenyl (PCB) Levels and Behavior in Inuit Preschoolers. *Environ. Int.* **2015**, *78*, 90–94.

(134) Schantz, S. L.; Widholm, J. J.; Rice, D. C. Effects of PCB Exposure on Neuropsychological Function in Children. *Environ. Health Perspect.* **2003**, *111* (3), 357–576.

(135) Ethier, A.-A.; Muckle, G.; Jacobson, S. W.; Ayotte, P.; Jacobson, J. L.; Saint-Amour, D. Assessing New Dimensions of Attentional Functions in Children Prenatally Exposed to Environmental Contaminants Using an Adapted Posner Paradigm. *Neurotoxicol. Teratol.* **2015**, *51*, 27–34.

(136) Šovčíková, E.; Wimmerová, S.; Strémy, M.; Kotianová, J.; Loffredo, C. A.; Murínová, Ľ. P.; Chovancová, J.; Čonka, K.; Lancz, K.; Trnovec, T. Simple Reaction Time in 8–9-Year Old Children Environmentally Exposed to PCBs. *Neurotoxicol.* **2015**, *51*, 138–144.

(137) Berghuis, S. A.; Soechitram, S. D.; Sauer, P. J. J.; Bos, A. F. Prenatal Exposure to Polychlorinated Biphenyls and Their Hydroxylated Metabolites Is Associated with Neurological Functioning in 3-Month-Old Infants. *Toxicol. Sci.* **2014**, *142* (2), 455–462.

(138) Chauhan, K. R.; Kodavanti, P. R. S.; McKinney, J. D. Assessing the Role of Ortho-Substitution on Polychlorinated Biphenyl Binding to Transthyretin, a Thyroxine Transport Protein. *Toxicol. App. Pharmacol.* **2000**, *162* (1), 10–21.

(139) Cheslack-Postava, K.; Rantakokko, P. V.; Hinkka-Yli-Salomäki, S.; Surcel, H.-M.; McKeague, I. W.; Kiviranta, H. A.; Sourander, A.; Brown, A. S. Maternal Serum Persistent Organic Pollutants in the Finnish Prenatal Study of Autism: A Pilot Study. *Neurotoxicol. Teratol.* **2013**, *38*, 1–5.

(140) Lyall, K.; Croen, L. A.; Sjödin, A.; Yoshida, C. K.; Zerbo, O.; Kharrazi, M.; Windham, G. C. Polychlorinated Biphenyl and Organochlorine Pesticide Concentrations in Maternal Mid-Pregnancy Serum Samples: Association with Autism Spectrum Disorder and Intellectual Disability. *Environ. Health Perspect.* **2017**, *125* (3), 474–480.

(141) Neugebauer, J.; Wittsiepe, J.; Kasper-Sonnenberg, M.; Schöneck, N.; Schölmerich, A.; Wilhelm, M. The Influence of Low Level Pre- and Perinatal Exposure to PCDD/Fs, PCBs, and Lead on Attention Performance and Attention-Related Behavior among German School-Aged Children: Results from the Duisburg Birth Cohort Study. *Int. J. Hyg. Envir. Heal.* **2015**, *218* (1), 153–162.

(142) Verner, M.-A.; Hart, J. E.; Sagiv, S. K.; Bellinger, D. C.; Altshul, L. M.; Korrick, S. A. Measured Prenatal and Estimated Postnatal Levels of Polychlorinated Biphenyls (PCBs) and ADHD-Related Behaviors in 8-Year-Old Children. *Environ. Health Perspect.* **2015**, *123* (9), 888–894.

(143) Mennigen, J. A.; Thompson, L. M.; Bell, M.; Tellez Santos, M.; Gore, A. C. Transgenerational Effects of Polychlorinated Biphenyls: 1. Development and Physiology across 3 Generations of Rats. *Environ. Health* **2018**, *17*, 18.

(144) Hens, B.; Hens, L. Persistent Threats by Persistent Pollutants: Chemical Nature, Concerns and Future Policy Regarding PCBs—What Are We Heading For? *Toxics.* **2018**, *6* (1), 1.

(145) McFarland, V. A.; Clarke, J. U. Environmental Occurrence, Abundance, and Potential Toxicity of Polychlorinated Biphenyl Congeners: Considerations for a Congener-Specific Analysis. *Environ. Health Perspect.* **1989**, *81*, 225–239.

(146) Chevrier J.; Eskenazi B.; Holland N.; Bradman A.; Barr D.B. Effects of Exposure to Polychlorinated Biphenyls and Organochlorine Pesticides on Thyroid Function during Pregnancy. *Am. J. Epidemiol.* **2008**, *168*, 298–310.

(147) Al-Salman, F.; Plant, N. Non-Coplanar Polychlorinated Biphenyls (PCBs) Are Direct Agonists for the Human Pregnane-X Receptor and Constitutive Androstane Receptor and Activate Target Gene Expression in a Tissue-Specific Manner. *Toxicol. App. Pharmacol.* **2012**, *263* (1), 7–13.

(148) Safe, S.; Hutzinger, O. Polychlorinated Biphenyls (PCBs) and Polybrominated Biphenyls (PBBs): Biochemistry, Toxicology, and Mechanism of Action. *CRC Cr. Rev. Toxicol.* **1984**, *13* (4), 319–395.
(149) Safe, S.; Bandiera, S.; Sawyer, T.; Robertson, L.; Safe, L.; Parkinson, A.; Thomas, P. E.; Ryan, D. E.; Reik, L. M.; Levin, W.; Denomme, M. A.; Fujita, T. PCBs: Structure–Function Relationships and Mechanism of Action. *Environ. Health Perspect.* **1985**, *60*, 47–56.
(150) Pavuk, M.; Schecter, A. J.; Akhtar, F. Z.; Michalek, J. E. Serum 2,3,7,8-Tetrachlorodibenzo-p-Dioxin (TCDD) Levels and Thyroid Function in Air Force Veterans of the Vietnam War. *Ann. Epidemol.* **2003**, *13* (5), 335–343.
(151) Council, N. R. *A Risk-Management Strategy for PCB-Contaminated Sediments*; The National Academies Press: Washington, DC, 2001.
(152) Gordon, A.; Surks, M. I.; Oppenheimer, J. H. Thyroxine Stimulation of Amino Acid Incorporation Into Mitochondrial Protein: Differences Between In Vivo and In Vitro Effects. *Acta Endocrinol.* **1973**, *72* (4), 684–696.
(153) McKinney, J.; Fannin, R.; Jordan, S.; Chae, K.; Rickenbacher, U.; Pedersen, L. Polychlorinated Biphenyls and Related Compound Interactions with Specific Binding Sites for Thyroxine in Rat Liver Nuclear Extracts. *J. Med. Chem.* **1987**, *30* (1), 79–86.
(154) Lans, M. C.; Klasson-Wehler, E.; Willemsen, M.; Meussen, E.; Safe, S.; Brouwer, A. Structure-Dependent, Competitive Interaction of Hydroxy-Polychlorobiphenyls, -Dibenzo-p-Dioxins and -Dibenzofurans with Human Transthyretin. *Chem.-Biol. Interact.* **1993**, *88* (1), 7–21.
(155) Lans, M. C.; Spiertz, C.; Brouwer, A.; Koeman, J. H. Different Competition of Thyroxine Binding to Transthyretin and Thyroxine-Binding Globulin by Hydroxy-PCBs, PCDDs and PCDFs. *Eur. J. Pharm.-Environ.* **1994**, *270* (2), 129–136.
(156) Schuur, A. G.; van Leeuwen-Bol, I.; Jong, W. M. C.; Bergman, Å.; Coughtrie, M. W. H.; Brouwer, A.; Visser, T. J. In Vitro Inhibition of Thyroid Hormone Sulfation by Polychlorobiphenylols: Isozyme Specificity and Inhibition Kinetics. *Toxicol. Sci.* **1998**, *45* (2), 188–194.
(157) Schuur, A. G.; Legger, F. F.; van Meeteren, M. E.; Moonen, M. J.; van Leeuwen-Bol, I.; Bergman, A.; Visser, T. J.; Brouwer, A. In Vitro Inhibition of Thyroid Hormone Sulfation by Hydroxylated Metabolites of Halogenated Aromatic Hydrocarbons. *Chem. Res. Toxicol.* **1998**, *11* (9), 1075–1081.
(158) Luo, Y.-L.; Luo, X.-J.; Ye, M.-X.; Lin, L.; Zeng, Y.-H.; Mai, B.-X. Species-Specific Debromination of Polybromodiphenyl Ethers Determined by Deiodinase Activity in Fish. *Environ. Pollut.* **2019**, *246*, 710–716.
(159) Soechitram, S. D.; Berghuis, S. A.; Visser, T. J.; Sauer, P. J. J. Polychlorinated Biphenyl Exposure and Deiodinase Activity in Young Infants. *Sci. Total Environ.* **2017**, *574*, 1117–1124.
(160) Viluksela, M.; Raasmaja, A.; Lebofsky, M.; Stahl, B. U.; Rozman, K. K. Tissue-Specific Effects of 2,3,7,8-Tetrachlorodibenzo-p-Dioxin (TCDD) on the Activity of 5′-Deiodinases I and II in Rats. *Toxicol. Lett.* **2004**, *147* (2), 133–142.
(161) Eltom, S. E.; Babish, J. G.; Ferguson, D. C. The Interaction of L-Triiodothyronine and 2,3,7,8-Tetrachlorodibenzo-p-Dioxin on Ah-Receptor-Mediated Hepatic Phase I and Phase II Enzymes and Iodothyronine 5'-Deiodinase in Thyroidectomized Rats. *Toxicol. Lett.* **1992**, *61* (2), 125–139.
(162) Buckman, A. H.; Fisk, A. T.; Parrott, J. L.; Solomon, K. R.; Brown, S. B. PCBs Can Diminish the Influence of Temperature on Thyroid Indices in Rainbow Trout (Oncorhynchus Mykiss). *Aquat. Toxicol.* **2007**, *84* (3), 366–378.
(163) Janz, D. M.; Bellward, G. D. In Ovo2,3,7,8-Tetrachlorodibenzo-p-Dioxin Exposure in Three Avian Species: 1. Effects on Thyroid Hormones and Growth during the Perinatal Period. *Toxicol. App. Pharmacol.* **1996**, *139* (2), 281–291.
(164) Beck, V.; Roelens, S. A.; Darras, V. M. Exposure to PCB 77 Induces Tissue-Dependent Changes in Iodothyronine Deiodinase Activity Patterns in the Embryonic Chicken. *Gen. Compar. Endocrinol.* **2006**, *148* (3), 327–335.

(165) Gould, J. C.; Cooper, K. R.; Scanes, C. G. Effects of Polychlorinated Biphenyls on Thyroid Hormones and Liver Type I Monodeiodinase in the Chick Embryo. *Ecotox. Environ. Safe.* **1999**, *43* (2), 195–203.
(166) Couderc, M.; Marchand, J.; Zalouk-Vergnoux, A.; Kamari, A.; Moreau, B.; Blanchet-Letrouvé, I.; Le Bizec, B.; Mouneyrac, C.; Poirier, L. Thyroid Endocrine Status of Wild European Eels (Anguilla Anguilla) in the Loire (France). Relationships with Organic Contaminant Body Burdens. *Sci. Total Environ.* **2016**, *550*, 391–405.
(167) Jarque, S.; Piña, B. Deiodinases and Thyroid Metabolism Disruption in Teleost Fish. *Environ. Res.* **2014**, *135*, 361–375.
(168) Gaum, P. M.; Lang, J.; Esser, A.; Schettgen, T.; Neulen, J.; Kraus, T.; Gube, M. Exposure to Polychlorinated Biphenyls and the Thyroid Gland – Examining and Discussing Possible Longitudinal Health Effects in Humans. *Environ. Research* **2016**, *148*, 112–121.
(169) Tebourbi, O.; Hallègue, D.; Yacoubi, M. T.; Sakly, M.; Rhouma, K. B. Subacute Toxicity of p,P′-DDT on Rat Thyroid: Hormonal and Histopathological Changes. *Environ. Toxicol. Phar.* **2010**, *29* (3), 271–279.
(170) Hood, A.; Klaassen, C. D. Effects of Microsomal Enzyme Inducers on Outer-Ring Deiodinase Activity toward Thyroid Hormones in Various Rat Tissues. *Toxicol. App. Pharmacol.* **2000**, *163* (3), 240–248.
(171) Raasmaja, A.; Viluksela, M.; Rozman, K. K. Decreased Liver Type I 5′-Deiodinase and Increased Brown Adipose Tissue Type II 5′-Deiodinase Activity in 2,3,7,8-Tetrachlorodibenzo-p-Dioxin (TCDD)-Treated Long-Evans Rats. *Toxicology* **1996**, *114* (3), 199–205.
(172) Manna, D.; Mugesh, G. Deiodination of Thyroid Hormones by Iodothyronine Deiodinase Mimics: Does an Increase in the Reactivity Alter the Regioselectivity? *J. Am. Chem. Soc.* **2011**, *133* (26), 9980–9983.
(173) Mondal, S.; Mugesh, G. Novel Thyroid Hormone Analogues, Enzyme Inhibitors and Mimetics, and Their Action. *Mol. Cell. Endocrinol.* **2017**, *458*, 91–104.
(174) Metrangolo, P.; Neukirch, H.; Pilati, T.; Resnati, G. Halogen Bonding Based Recognition Processes: A World Parallel to Hydrogen Bonding. *Acc. Chem. Res.* **2005**, *38* (5), 386–395.
(175) Pierangelo, M.; Giuseppe, R. Halogen Bonding: A Paradigm in Supramolecular Chemistry. *Chem. Eur. J.* **2001**, *7* (12), 2511–2519.
(176) Varadwaj, P. R.; Varadwaj, A.; Marques, H. M. Halogen Bonding: A Halogen-Centered Noncovalent Interaction Yet to Be Understood. *Inorganics* **2019**, *7* (3), 40.
(177) Politzer, P.; Murray, J. S.; Clark, T.; Resnati, G. The σ-Hole Revisited. *Phys. Chem. Chem. Phys.* **2017**, *19* (48), 32166–32178.
(178) Murray, J. S.; Lane, P.; Politzer, P. Expansion of the σ-Hole Concept. *J. Mol. Model.* **2009**, *15* (6), 723–729.
(179) Bayse, C. A. Halogen Bonding from the Bonding Perspective with Considerations for Mechanisms of Thyroid Hormone Activation and Inhibition. *New J. Chem.* **2018**, *42* (13), 10623–10632.
(180) Palusiak, M. On the Nature of Halogen Bond – The Kohn–Sham Molecular Orbital Approach. *J. Mol. Struc.-Theochem.* **2010**, *945* (1), 89–92.
(181) Stone, A. J. Are Halogen Bonded Structures Electrostatically Driven? *J. Am. Chem. Soc.* **2013**, *135* (18), 7005–7009.
(182) Donald, K. J.; Wittmaack, B. K.; Crigger, C. Tuning σ-Holes: Charge Redistribution in the Heavy (Group 14) Analogues of Simple and Mixed Halomethanes Can Impose Strong Propensities for Halogen Bonding. *J. Phys. Chem. A* **2010**, *114* (26), 7213–7222.
(183) Varadwaj, A.; Marques, H. M.; Varadwaj, P. R. Is the Fluorine in Molecules Dispersive? Is Molecular Electrostatic Potential a Valid Property to Explore Fluorine-Centered Non-Covalent Interactions? *Molecules* **2019**, *24* (3), 379.
(184) Huber, S. M.; Jimenez-Izal, E.; Ugalde, J. M.; Infante, I. Unexpected Trends in Halogen-Bond Based Noncovalent Adducts. *Chem. Commun.* **2012**, *48* (62), 7708–7710.

(185) Thirman, J.; Engelage, E.; Huber, S. M.; Head-Gordon, M. Characterizing the Interplay of Pauli Repulsion, Electrostatics, Dispersion and Charge Transfer in Halogen Bonding with Energy Decomposition Analysis. *Phys. Chem. Chem. Phys.* **2018**, *20* (2), 905–915.
(186) Angarov, V.; Kozuch, S. On the σ, π and δ Hole Interactions: A Molecular Orbital Overview. *New J. Chem.* **2018**, *42* (2), 1413–1422.
(187) Jiao, Y.; Weinhold, F. What Is the Nature of Supramolecular Bonding? Comprehensive NBO/NRT Picture of Halogen and Pnicogen Bonding in RPH2···IF/FI Complexes (R = CH3, OH, CF3, CN, NO2). *Molecules* **2019**, *24* (11), 2090.
(188) Pimentel, G. C. The Bonding of Trihalide and Bifluoride Ions by the Molecular Orbital Method. *J. Chem. Phys.* **1951**, *19* (4), 446–448.
(189) Hach, R. J.; Rundle, R. E. The Structure of Tetramethylammonium Pentaiodide1,1a. *J. Am. Chem. Soc.* **1951**, *73* (9), 4321–4324.
(190) Morse, D. C.; Wehler, E. K.; Wesseling, W.; Koeman, J. H.; Brouwer, A. Alterations in Rat Brain Thyroid Hormone Status Following Pre- and Postnatal Exposure to Polychlorinated Biphenyls (Aroclor 1254). *Toxicol. App. Pharmacol.* **1996**, *136* (2), 269–279.
(191) Coimbra, A. M.; Reis-Henriques, M. A.; Darras, V. M. Circulating Thyroid Hormone Levels and Iodothyronine Deiodinase Activities in Nile Tilapia (Oreochromis Niloticus) Following Dietary Exposure to Endosulfan and Aroclor 1254. *Comp. Biochem. Phys. C.* **2005**, *141* (1), 8–14.
(192) Peeters, R. P.; Visser, T. J. Metabolism of Thyroid Hormone. In *Endotext*; Feingold, K. R., Anawalt, B., Boyce, A., Chrousos, G., Dungan, K., Grossman, A., Hershman, J. M., Kaltsas, G., Koch, C., Kopp, P., Korbonits, M., McLachlan, R., Morley, J. E., New, M., Perreault, L., Purnell, J., Rebar, R., Singer, F., Trence, D. L., Vinik, A., Wilson, D. P., Eds.; MDText.com, Inc.: South Dartmouth (MA), 2000.
(193) Gutteridge, A.; Thornton, J. Conformational Change in Substrate Binding, Catalysis and Product Release: An Open and Shut Case? *FEBS Lett.* **2004**, *567* (1), 67–73.
(194) Kovermann, M.; Grundström, C.; Sauer-Eriksson, A. E.; Sauer, U. H.; Wolf-Watz, M. Structural Basis for Ligand Binding to an Enzyme by a Conformational Selection Pathway. *P. Natl. A. Sci. USA* **2017**, *114* (24), 6298–6303.
(195) Schweizer, U.; Towell, H.; Vit, A.; Rodriguez-Ruiz, A.; Steegborn, C. Structural Aspects of Thyroid Hormone Binding to Proteins and Competitive Interactions with Natural and Synthetic Compounds. *Mol. Cell. Endocrinol.* **2017**, *458*, 57–67.
(196) Mondal, S.; Mugesh, G. Structure Elucidation and Characterization of Different Thyroxine Polymorphs. *Angew. Chem. Int. Edit.* **2015**, *54* (37), 10833–10837.
(197) Mizukami, Y. Exploratory Ab Initio MO Calculations on the Structures of Polychlorinated Biphenyls(PCBs): A Possible Way to Make a Coplanar PCB Stable at Coplanar Conformation. *J. Mol. Struc.-Theochem.* **1999**, *488* (1), 11–19.
(198) Purkey, H. E.; Palaninathan, S. K.; Kent, K. C.; Smith, C.; Safe, S. H.; Sacchettini, J. C.; Kelly, J. W. Hydroxylated Polychlorinated Biphenyls Selectively Bind Transthyretin in Blood and Inhibit Amyloidogenesis: Rationalizing Rodent PCB Toxicity. *Chem. Biol.* **2004**, *11* (12), 1719–1728.
(199) Arulmozhiraja, S.; Selvin, P. C.; Fujii, T. Structures, Potential Energy Curves, and Torsional Barrier Heights for Selected Polychlorinated Biphenyls: A Density Functional Theory Study. *J. Phys. Chem. A* **2002**, *106* (9), 1765–1769.
(200) Almenningen, A.; Bastiansen, O.; Fernholt, L.; Gundersen, S.; Kloster-Jensen, E.; Cyvin, B. N.; Cyvin, S. J.; Samdal, S.; Skancke, A. Structure and Barrier to Internal Rotation of Biphenyl Derivatives in the Gaseous State: Part 2. Structure of 3,3′-Dibromo-, 3,5,4′ -Tribronio- and 3,5,3′5′ -Tetrabromobiphenyl. *J. Mol. Struct.* **1985**, *128* (1), 77–93.
(201) Bastiansen, O.; Samdal, S. Structure and Barrier of Internal Rotation of Biphenyl Derivatives in the Gaseous State: Part 4. Barrier of Internal Rotation in Biphenyl, Perdeuterated Biphenyl and Seven Non-Ortho-Substituted Halogen Derivatives. *J. Mol. Struct.* **1985**, *128* (1), 115–125.

(202) Schurig, V.; Reich, S. Determination of the Rotational Barriers of Atropisomeric Polychlorinated Biphenyls (PCBs) by a Novel Stopped-Flow Multidimensional Gas Chromatographic Technique. *Chirality* **1998**, *10* (4), 316–320.
(203) Harju, M. T.; Haglund, P. Determination of the Rotational Energy Barriers of Atropisomeric Polychlorinated Biphenyls. *Fresen. J. Anal. Chem.* **1999**, *364* (3), 219–223.
(204) Masson, E. Torsional Barriers of Substituted Biphenyls Calculated Using Density Functional Theory: A Benchmarking Study. *Org. Biomol. Chem.* **2013**, *11* (17), 2859–2871.
(205) McKinney, J. D.; Waller, C. L. Polychlorinated Biphenyls as Hormonally Active Structural Analogues. *Environ. Health Perspect.* **1994**, *102* (3), 290–297.
(206) Katarzyńska, D.; Hrabia, A.; Kowalik, K.; Sechman, A. Comparison of the in Vitro Effects of TCDD, PCB 126 and PCB 153 on Thyroid-Restricted Gene Expression and Thyroid Hormone Secretion by the Chicken Thyroid Gland. *Environ. Toxicol. Phar.* **2015**, *39* (2), 496–503.
(207) Yang, H.; Chen, H.; Guo, H.; Li, W.; Tang, J.; Xu, B.; Sun, M.; Ding, G.; Jiang, L.; Cui, D.; Zheng, X.; Duan, Y. Molecular Mechanisms of 2, 3′, 4, 4′, 5-Pentachlorobiphenyl-Induced Thyroid Dysfunction in FRTL-5 Cells. *Plos One* **2015**, *10* (3), e0120133.
(208) Guo, H.; Yang, H.; Chen, H.; Li, W.; Tang, J.; Cheng, P.; Xie, Y.; Liu, Y.; Ding, G.; Cui, D.; Zheng, X.; Duan, Y. Molecular Mechanisms of Human Thyrocyte Dysfunction Induced by Low Concentrations of Polychlorinated Biphenyl 118 through the Akt/FoxO3a/NIS Pathway. *J. App. Toxicol.* **2015**, *35* (9), 992–998.
(209) Zhou, Z.-L.; Liu, H.-L.; Wu, J. W.; Tsao, C.-W.; Chen, W.-H.; Liu, K.-T.; Ho, Y. Computer-Aided Discovery of Potential Inhibitors for Transthyretin-Related Amyloidosis. *J. Chin. Chem. Soc.* **2014**, *61* (2), 263–273.
(210) Germain, D. L. St.; Galton, V. A. The Deiodinase Family of Selenoproteins. *Thyroid* **1997**, *7* (4), 655–668.
(211) Labunskyy, V. M.; Hatfield, D. L.; Gladyshev, V. N. Selenoproteins: Molecular Pathways and Physiological Roles. *Physiol. Rev.* **2014**, *94* (3), 739–777.
(212) Moghadaszadeh, B.; Beggs, A. H. Selenoproteins and Their Impact on Human Health Through Diverse Physiological Pathways. *Physiology* **2006**, *21*, 307–315.
(213) Yang, R.; Liu, Y.; Zhou, Z. Selenium and Selenoproteins, from Structure, Function to Food Resource and Nutrition. *Food Sci. Technol. Res.* **2017**, *23* (3), 363–373.
(214) Martin, J. L. Thioredoxin —a Fold for All Reasons. *Structure* **1995**, *3* (3), 245–250.
(215) Ren, G.; Stephan, D.; Xu, Z.; Zheng, Y.; Tang, D.; Harrison, R. S.; Kurz, M.; Jarrott, R.; Shouldice, S. R.; Hiniker, A.; Martin, J. L.; Heras, B.; Bardwell, J. C. A. Properties of the Thioredoxin Fold Superfamily Are Modulated by a Single Amino Acid Residue. *J. Biol. Chem.* **2009**, *284* (15), 10150–10159.
(216) Collet, J.-F.; Messens, J. Structure, Function, and Mechanism of Thioredoxin Proteins. *Antioxid. Redox Signal.* **2010**, *13* (8), 1205–1216.
(217) Atkinson, H. J.; Babbitt, P. C. An Atlas of the Thioredoxin Fold Class Reveals the Complexity of Function-Enabling Adaptations. *PLOS Comput. Biol.* **2009**, *5* (10), e1000541.
(218) Callebaut, I.; Curcio-Morelli, C.; Mornon, J. P.; Gereben, B.; Buettner, C.; Huang, S.; Castro, B.; Fonseca, T. L.; Harney, J. W.; Larsen, P. R.; Bianco, A. C. The Iodothyronine Selenodeiodinases Are Thioredoxin-Fold Family Proteins Containing a Glycoside Hydrolase Clan GH-A-like Structure. *J. Biol. Chem.* **2003**, *278* (38), 36887–36896.
(219) Luongo, C.; Dentice, M.; Salvatore, D. Deiodinases and Their Intricate Role in Thyroid Hormone Homeostasis. *Nat. Rev. Endocrinol.* **2019**, *15* (8), 479–488.
(220) Dentice, M.; Salvatore, D. Deiodinases: The Balance of Thyroid Hormone: Local Impact of Thyroid Hormone Inactivation. *J. Endocrinol.* **2011**, *209* (3), 273–282.
(221) Larsen, P. R.; Zavacki, A. M. The Role of the Iodothyronine Deiodinases in the Physiology and Pathophysiology of Thyroid Hormone Action. *Eur. Thyroid J.* **2012**, *1* (4), 232–242.
(222) Köhrle, J. Local Activation and Inactivation of Thyroid Hormones: The Deiodinase Family. *Mol. Cell. Endocrinol.* **1999**, *151* (1–2), 103–119.

(223) Köhrle, J. The Selenoenzyme Family of Deiodinase Isozymes Controls Local Thyroid Hormone Availability. *Rev. Endocr. Metab. Disord.* **2000**, *1* (1–2), 49–58.
(224) Rijntjes, E.; Scholz, P. M.; Mugesh, G.; Köhrle, J. Se- and S-Based Thiouracil and Methimazole Analogues Exert Different Inhibitory Mechanisms on Type 1 and Type 2 Deiodinases. *Eur. Thyroid J.* **2013**, *2* (4), 252–258.
(225) Mol, K. A.; Van Der Geyten, S.; Darras, V. M.; Visser, T. J.; Kühn, E. R. Characterization of Iodothyronine Outer Ring and Inner Ring Deiodinase Activities in the Blue Tilapia, Oreochromis Aureus. *Endocrinology* **1997**, *138* (5), 1787–1793.
(226) Fetrow, J. S. Omega Loops; Nonregular Secondary Structures Significant in Protein Function and Stability. *FASEB J.* **1995**, *9* (9), 708–717.
(227) Banerjee, S.; Pieper, U.; Kapadia, G.; Pannell, L. K.; Herzberg, O. Role of the Omega-Loop in the Activity, Substrate Specificity, and Structure of Class A Beta-Lactamase. *Biochemistry* **1998**, *37* (10), 3286–3296.
(228) Jorgensen, W. L.; Schyman, P. Treatment of Halogen Bonding in the OPLS-AA Force Field; Application to Potent Anti-HIV Agents. *J. Chem. Theory Comput.* **2012**, *8* (10), 3895–3801.
(229) Carpenter, E. P.; Beis, K.; Cameron, A. D.; Iwata, S. Overcoming the Challenges of Membrane Protein Crystallography. *Curr. Opin. Struct. Biol.* **2008**, *18* (5), 581–586.
(230) Schneidman-Duhovny, D.; Inbar, Y.; Nussinov, R.; Wolfson, H. J. PatchDock and SymmDock: Servers for Rigid and Symmetric Docking. *Nucleic Acids Res.* **2005**, *33* (Web Server issue), W363-367.
(231) Kozakov, D.; Hall, D. R.; Xia, B.; Porter, K. A.; Padhorny, D.; Yueh, C.; Beglov, D.; Vajda, S. The ClusPro Web Server for Protein–Protein Docking. *Nat. Protoc.* **2017**, *12* (2), 255–278.
(232) Chen, R.; Li, L.; Weng, Z. ZDOCK: An Initial-Stage Protein-Docking Algorithm. *Proteins* **2003**, *52* (1), 80–87.
(233) de Vries, S. J.; Schindler, C. E. M.; Chauvot de Beauchêne, I.; Zacharias, M. A Web Interface for Easy Flexible Protein-Protein Docking with ATTRACT. *Biophys. J.* **2015**, *108* (3), 462–465.
(234) Hirotsu, S.; Abe, Y.; Okada, K.; Nagahara, N.; Hori, H.; Nishino, T.; Hakoshima, T. Crystal Structure of a Multifunctional 2-Cys Peroxiredoxin Heme-Binding Protein 23 KDa/Proliferation-Associated Gene Product. *Proc. Natl. Acad. Sci. U.S.A.* **1999**, *96* (22), 12333–12338.
(235) Copley, S. D.; Novak, W. R. P.; Babbitt, P. C. Divergence of Function in the Thioredoxin Fold Suprafamily: Evidence for Evolution of Peroxiredoxins from a Thioredoxin-like Ancestor. *Biochemistry* **2004**, *43* (44), 13981–13995.
(236) Hall, A.; Nelson, K.; Poole, L. B.; Karplus, P. A. Structure-Based Insights into the Catalytic Power and Conformational Dexterity of Peroxiredoxins. *Antioxid. Redox Signal.* **2011**, *15* (3), 795–815.
(237) Winterbourn, C. C. Reconciling the Chemistry and Biology of Reactive Oxygen Species. *Nat. Chem. Biol.* **2008**, *4* (5), 278–286.
(238) Fomenko, D. E.; Gladyshev, V. N. Identity and Functions of CxxC-Derived Motifs. *Biochemistry* **2003**, *42* (38), 11214–11225.
(239) Gretes, M. C.; Karplus, P. A. Observed Octameric Assembly of a Plasmodium Yoelii Peroxiredoxin Can Be Explained by the Replacement of Native "Ball-and-Socket" Interacting Residues by an Affinity Tag. *Protein Sci.* **2013**, *22* (10), 1445–1452.
(240) Sarma, G. N.; Nickel, C.; Rahlfs, S.; Fischer, M.; Becker, K.; Karplus, P. A. Crystal Structure of a Novel Plasmodium Falciparum 1-Cys Peroxiredoxin. *J. Mol. Biol.* **2005**, *346* (4), 1021–1034.
(241) Sievers, F.; Wilm, A.; Dineen, D.; Gibson, T. J.; Karplus, K.; Li, W.; Lopez, R.; McWilliam, H.; Remmert, M.; Söding, J.; Thompson, J. D.; Higgins, D. G. Fast, Scalable Generation of High-Quality Protein Multiple Sequence Alignments Using Clustal Omega. *Mol Syst Biol* **2011**, *7*, 539.
(242) Thompson, L. C.; Walters, J.; Burke, J.; Parsons, J. F.; Armstrong, R. N.; Dirr, H. W. Double Mutation at the Subunit Interface of Glutathione Transferase RGSTM1-1 Results in a Stable, Folded Monomer. *Biochemistry* **2006**, *45* (7), 2267–2273.
(243) LeFevre, K. R.; Cordes, M. H. J. Retroevolution of λ Cro toward a Stable Monomer. *P. Natl. A. Sci. USA* **2003**, *100* (5), 2345.

(244) Hu, Z.; Ma, B.; Wolfson, H.; Nussinov, R. Conservation of Polar Residues as Hot Spots at Protein Interfaces. *Proteins* **2000**, *39* (4), 331–342.
(245) Fujiwara, K.; Toda, H.; Ikeguchi, M. Dependence of α-Helical and β-Sheet Amino Acid Propensities on the Overall Protein Fold Type. *BMC Struct. Biol.* **2012**, *12* (1), 18.
(246) Chung, S. Y.; Subbiah, S. A Structural Explanation for the Twilight Zone of Protein Sequence Homology. *Structure* **1996**, *4* (10), 1123–1127.
(247) Vreven, T.; Hwang, H.; Pierce, B. G.; Weng, Z. Evaluating Template-Based and Template-Free Protein–Protein Complex Structure Prediction. *Brief Bioinform.* **2014**, *15* (2), 169–176.
(248) Aloy, P.; Ceulemans, H.; Stark, A.; Russell, R. B. The Relationship between Sequence and Interaction Divergence in Proteins. *J. Mol. Biol.* **2003**, *332* (5), 989–998.
(249) Weng, G.; Wang, E.; Wang, Z.; Liu, H.; Zhu, F.; Li, D.; Hou, T. HawkDock: A Web Server to Predict and Analyze the Protein–Protein Complex Based on Computational Docking and MM/GBSA. *Nucleic Acids Res.* **2019**, *47* (W1), W322–W330.
(250) Bogan, A. A.; Thorn, K. S. Anatomy of Hot Spots in Protein Interfaces. *J. Mol. Biol.* **1998**, *280* (1), 1–9.
(251) Heo, L.; Lee, H.; Seok, C. GalaxyRefineComplex: Refinement of Protein-Protein Complex Model Structures Driven by Interface Repacking. *Sci. Rep.* **2016**, *6*, 32153.
(252) Pierce, B.; Tong, W.; Weng, Z. M-ZDOCK: A Grid-Based Approach for Cn Symmetric Multimer Docking. *Bioinformatics* **2005**, *21* (8), 1472–1478.
(253) Lensink, M. F.; Velankar, S.; Kryshtafovych, A.; Huang, S.-Y.; Schneidman-Duhovny, D.; Sali, A.; Segura, J.; Fernandez-Fuentes, N.; Viswanath, S.; Elber, R.; Grudinin, S.; Popov, P.; Neveu, E.; Lee, H.; Baek, M.; Park, S.; Heo, L.; Rie Lee, G.; Seok, C.; Qin, S.; Zhou, H.-X.; Ritchie, D. W.; Maigret, B.; Devignes, M.-D.; Ghoorah, A.; Torchala, M.; Chaleil, R. A. G.; Bates, P. A.; Ben-Zeev, E.; Eisenstein, M.; Negi, S. S.; Weng, Z.; Vreven, T.; Pierce, B. G.; Borrman, T. M.; Yu, J.; Ochsenbein, F.; Guerois, R.; Vangone, A.; Rodrigues, J. P. G. L. M.; van Zundert, G.; Nellen, M.; Xue, L.; Karaca, E.; Melquiond, A. S. J.; Visscher, K.; Kastritis, P. L.; Bonvin, A. M. J. J.; Xu, X.; Qiu, L.; Yan, C.; Li, J.; Ma, Z.; Cheng, J.; Zou, X.; Shen, Y.; Peterson, L. X.; Kim, H.-R.; Roy, A.; Han, X.; Esquivel-Rodriguez, J.; Kihara, D.; Yu, X.; Bruce, N. J.; Fuller, J. C.; Wade, R. C.; Anishchenko, I.; Kundrotas, P. J.; Vakser, I. A.; Imai, K.; Yamada, K.; Oda, T.; Nakamura, T.; Tomii, K.; Pallara, C.; Romero-Durana, M.; Jiménez-García, B.; Moal, I. H.; Férnandez-Recio, J.; Joung, J. Y.; Kim, J. Y.; Joo, K.; Lee, J.; Kozakov, D.; Vajda, S.; Mottarella, S.; Hall, D. R.; Beglov, D.; Mamonov, A.; Xia, B.; Bohnuud, T.; Del Carpio, C. A.; Ichiishi, E.; Marze, N.; Kuroda, D.; Roy Burman, S. S.; Gray, J. J.; Chermak, E.; Cavallo, L.; Oliva, R.; Tovchigrechko, A.; Wodak, S. J. Prediction of Homoprotein and Heteroprotein Complexes by Protein Docking and Template-Based Modeling: A CASP-CAPRI Experiment. *Proteins* **2016**, *84*, 323–348.
(254) Hou, T.; Wang, J.; Li, Y.; Wang, W. Assessing the Performance of the MM/PBSA and MM/GBSA Methods: I. The Accuracy of Binding Free Energy Calculations Based on Molecular Dynamics Simulations. *J. Chem. Inf. Model.* **2011**, *51* (1), 69–82.
(255) Wang, E.; Sun, H.; Wang, J.; Wang, Z.; Liu, H.; Zhang, J. Z. H.; Hou, T. End-Point Binding Free Energy Calculation with MM/PBSA and MM/GBSA: Strategies and Applications in Drug Design. *Chem. Rev.* **2019**, *119* (16), 9478–9508.
(256) Zoete, V.; Irving, M. B.; Michielin, O. MM-GBSA Binding Free Energy Decomposition and T Cell Receptor Engineering. *J. Mol. Recognit.* **2010**, *23* (2), 142–152.
(257) Ayoub, A. T.; Craddock, T. J. A.; Klobukowski, M.; Tuszynski, J. Analysis of the Strength of Interfacial Hydrogen Bonds between Tubulin Dimers Using Quantum Theory of Atoms in Molecules. *Biophys. J.* **2014**, *107* (3), 740–750.
(258) Baker, E. N.; Hubbard, R. E. Hydrogen Bonding in Globular Proteins. *Prog. Biophys. Mol. Bio.* **1984**, *44* (2), 97–179.
(259) Case, D. A.; Betz, R. M.; Cerutti, D. S.; Cheatham, T. E.; Darden, T. A.; Duke, R. E.; Giese, T. J.; Gohlke, H.; Goetz, A. W.; Homeyer, N.; Izadi, S.; Janowski, P.; Kaus, J.; Kovalenko, A.; Lee, T.

S.; LeGrand, S.; Li, P.; Lin, C.; Luchko, T.; Luo, R.; Madej, B.; Mermelstein, D.; Merz, K. M.; Monard, G.; Nguyen, H.; Nguyen, I.; Omelyan, A.; Onufriev, A.; Roe, D. R.; Roitberg, A.; Sagui, C.; Simmerling, C. L.; Botello-Smith, W. M.; Swails, J.; Walker, R. C.; Wang, J.; Wolf, R. M.; Wu, X.; Xiao, L.; Kollman, P. A. AMBER 16.

(260) Miller, B. R.; McGee, T. D.; Swails, J. M.; Homeyer, N.; Gohlke, H.; Roitberg, A. E. MMPBSA.Py: An Efficient Program for End-State Free Energy Calculations. *J. Chem. Theory Comput.* **2012**, *8* (9), 3314–3321.

APPENDIX A

COMPLETE TABLE OF PBDE DATA

Compound	*d*(Br--Se), Å	*d*(C-Br) with bound $SeMe^-$, Å	*d*(C-Br) (no $SeMe^-$), Å	Δ*d*(C-Br), Å	ΔE + ZPE, kcal mol^{-1}	$\Delta E_{D\rightarrow A}$, kcal mol^{-1}
XB-o'-3a-HO-BDE-7	2.919	2.018	1.904	0.114	-13.38	26.60
XB-p'-3a-HO-BDE-7	2.972	1.999	1.911	0.088	-13.46	21.74
XB-o-3-HO-BDE-47	2.834	2.073	1.906	0.167	-22.23	38.66
XB-p-3-HO-BDE-47	2.902	2.039	1.915	0.124	-21.65	29.38
XB-o'-3-HO-BDE-47	2.876	2.036	1.902	0.134	-16.84	30.88
XB-p'-3-HO-BDE-47	2.948	2.006	1.910	0.096	-16.05	23.34
XB-o-4-HO-BDE-42	2.818	2.069	1.896	0.173	-16.75	40.71
XB-m-4-HO-BDE-42	2.852	2.060	1.907	0.153	-22.53	37.23
XB-o'-4-HO-BDE-42	2.883	2.034	1.903	0.131	-16.05	30.16
XB-p'-4-HO-BDE-42	2.951	2.004	1.911	0.093	-15.16	23.15
XB-p-2a-HO-BDE-28	3.017	1.988	1.912	0.076	-11.62	19.15
XB-o'-2a-HO-BDE-28	2.969	2.000	1.907	0.093	-15.49	22.70
XB-p'-2a-HO-BDE-28	2.986	1.995	1.911	0.084	-12.93	20.96
XB-p'-4a-HO-BDE-49	2.950	2.005	1.911	0.094	-14.63	23.20
XB-o'-4a-HO-BDE-49	2.901	2.029	1.903	0.126	-15.69	28.76
XB-o-4a-HO-BDE-49	2.881	2.032	1.901	0.131	-17.75	29.94
XB-m-4a-HO-BDE-49	2.923	2.015	1.901	0.114	-14.99	26.79
XB-p'-6a-HO-BDE-99	2.880	2.034	1.902	0.132	-15.88	31.64
XB-o'-6a-HO-BDE-99	2.902	2.022	1.900	0.122	-15.05	28.80
XB-m'-6a-HO-BDE-99	2.889	2.028	1.903	0.125	-16.55	30.56
XB-o-6a-HO-BDE-99	2.852	2.046	1.901	0.145	-17.80	32.87
XB-p-6a-HO-BDE-99	2.923	2.014	1.909	0.105	-17.97	24.97
XB-p-6-HO-BDE-82	2.860	2.047	1.904	0.143	-17.78	33.20

XB-m-6-HO-BDE-82	2.811	2.072	1.897	0.175	-16.96	42.89
XB-o'-6-HO-BDE-82	2.616	2.276	1.899	0.377	-21.84	N/A
XB-o-6-HO-BDE-82	2.803	2.077	1.896	0.181	-17.16	42.20
XB-m'-6-HO-BDE-82	2.910	2.023	1.907	0.116	-15.59	28.02
XB-p'-4-HO-BDE-90	2.939	2.008	1.909	0.099	-16.78	23.93
XB-m-4-HO-BDE-90	2.859	2.055	1.913	0.142	-24.67	33.96
XB-m*-4-HO-BDE-90	2.786	2.088	1.896	0.192	-20.53	45.74
XB-o-4-HO-BDE-90	2.779	2.092	1.895	0.197	-20.39	47.31
XB-o'-4-HO-BDE-90	2.862	2.043	1.901	0.142	-17.98	31.76
XB-p-6-HO-BDE-140	2.854	2.047	1.904	0.143	-19.16	33.48
XB-o-6-HO-BDE-140	2.782	2.090	1.895	0.195	-18.66	45.74
XB-m-6-HO-BDE-140	2.798	2.079	1.896	0.183	-18.41	45.05
XB-o'-6-HO-BDE-140	2.684	2.193	1.901	0.292	-24.47	68.73
XB-p'-6-HO-BDE-140	2.911	2.020	1.908	0.112	-17.81	26.10
XB-p-6-HO-BDE-85	2.855	2.049	1.904	0.145	-18.47	33.69
XB-m-6-HO-BDE-85	2.806	2.075	1.897	0.178	-17.69	43.66
XB-o-6-HO-BDE-85	2.798	2.080	1.896	0.184	-17.93	43.00
XB-o'-6-HO-BDE-85	2.762	2.121	1.906	0.215	-21.22	48.19
XB-p'-6-HO-BDE-85	2.969	2.000	1.911	0.089	-14.34	21.88
XB-o'-5a-HO-BDE-99	2.848	2.047	1.900	0.147	-22.26	34.03
XB-p'-5a-HO-BDE-99	2.842	2.047	1.902	0.145	-20.64	35.82
XB-o-5a-HO-BDE-99	2.861	2.047	1.901	0.146	-17.26	33.13
XB-p-5a-HO-BDE-99	2.908	2.023	1.901	0.122	-15.65	28.05
XB-p'-6-HO-BDE-157	2.821	2.063	1.896	0.167	-17.34	41.82
XB-m'-6-HO-BDE-157	2.858	2.047	1.904	0.143	-18.29	33.63
XB-m'-6-HO-BDE-157	2.862	2.042	1.905	0.137	-17.48	32.44
XB-o-6-HO-BDE-157	2.753	2.111	1.896	0.215	-21.88	50.05

XB-m-6-HO-BDE-157	2.774	2.093	1.896	0.197	-21.04	49.71
XB-p-6-HO-BDE-157	2.832	2.057	1.903	0.154	-21.77	36.07
XB-p-6-HO-BDE-87	2.856	2.049	1.904	0.145	-18.42	33.64
XB-m-6-HO-BDE-87	2.806	2.074	1.896	0.178	-17.61	43.73
XB-o-6-HO-BDE-87	2.795	2.082	1.896	0.186	-17.81	43.36
XB-o'-6-HO-BDE-87	2.753	2.111	1.905	0.206	-20.50	45.62
XB-m'-6-HO-BDE-87	2.982	1.992	1.910	0.082	-13.92	21.08
XB-p'-4a-HO-BDE-17	2.960	2.002	1.912	0.090	-13.91	22.54
XB-o'-4a-HO-BDE-17	2.897	2.027	1.904	0.123	-14.45	28.69
XB-o-4a-HO-BDE-17	2.926	2.016	1.903	0.113	-13.25	25.79
XB-p-5-HO-BDE-47	2.900	2.037	1.913	0.124	-21.65	29.63
XB-o-5-HO-BDE-47	2.870	2.043	1.903	0.140	-16.53	31.85
XB-o'-5-HO-BDE-47	2.878	2.035	1.901	0.134	-16.62	30.59
XB-p'-5-HO-BDE-47	2.935	2.009	1.909	0.100	-14.15	24.21
XB-p-6-HO-BDE-47	2.941	2.013	1.909	0.104	-17.57	24.65
XB-o-6-HO-BDE-47	2.863	2.042	1.901	0.141	-16.97	31.62
XB-o'-6-HO-BDE-47	2.778	2.109	1.903	0.206	-17.51	44.77
XB-p'-6-HO-BDE-47	2.929	2.013	1.911	0.102	-12.44	21.12
XB-p-3a-HO-BDE-154	2.818	2.080	1.906	0.174	-23.90	41.55
XB-m-3a-HO-BDE-154	2.849	2.045	1.901	0.144	-19.79	33.91
XB-o-3a-HO-BDE-154	2.804	2.098	1.896	0.202	-25.46	44.57
XB-o'-3a-HO-BDE-154	2.807	2.072	1.901	0.171	-25.04	39.12
XB-p'-3a-HO-BDE-154	2.885	2.028	1.908	0.120	-23.68	28.29
XB-p'-3a-HO-BDE-28	2.956	2.003	1.915	0.088	-15.12	22.79
XB-o'-3a-HO-BDE-28	2.903	2.024	1.903	0.121	-15.36	28.18
XB-p-3a-HO-BDE-28	2.955	2.017	1.910	0.107	-18.24	24.85
XB-m-BDE-99	2.852	2.041	1.902	0.139	-19.59	34.29
XB-p'-BDE-99	2.935	2.009	1.909	0.100	-16.89	24.25

XB-o-BDE-99	2.840	2.051	1.900	0.151	-19.50	35.12
XB-p-BDE-99	2.846	2.046	1.902	0.144	-19.90	35.07
XB-o'-BDE-99	2.858	2.044	1.901	0.143	-18.29	32.93
XB-o-BDE-47	2.869	2.039	1.903	0.136	-17.54	31.64
XB-p-BDE-47	2.943	2.007	1.911	0.096	-16.62	23.03
XB-p-BDE-153	2.839	2.049	1.900	0.149	-20.64	35.91
XB-o-BDE-153	2.826	2.059	1.899	0.160	-20.69	37.04
XB-m-BDE-153	2.843	2.046	1.899	0.147	-20.39	35.70
XB-o-BDE-209	2.813	2.068	1.894	0.174	-28.22	40.87
XB-m-BDE-209	2.816	2.060	1.895	0.165	-26.78	39.19
XB-p-BDE-209	2.815	2.062	1.897	0.165	-26.59	39.69

APPENDIX B

COMPLETE LIST OF PCBs WITH THEIR CORRESPONDING STRUCTURES

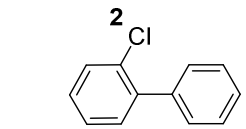

PCB-1

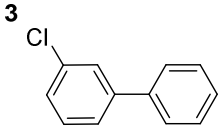

PCB-2

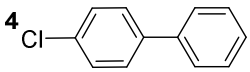

PCB-3

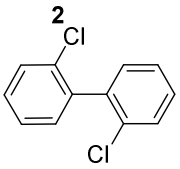

PCB-4

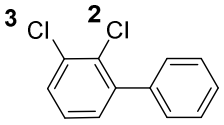

PCB-5

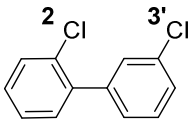

PCB-6

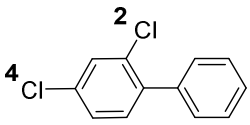

PCB-7

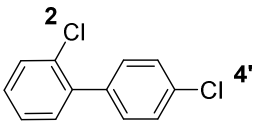

PCB-8

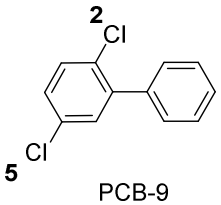

PCB-9

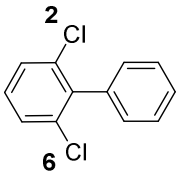

PCB-10

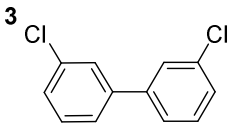

PCB-11

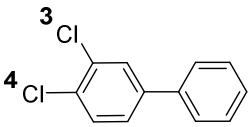

PCB-12

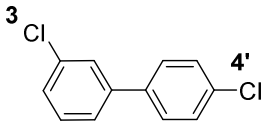

PCB-13

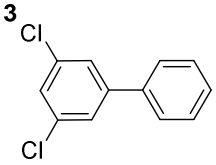

PCB-14

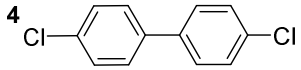

PCB-15

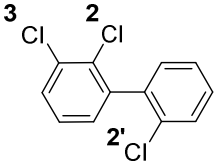

PCB-16

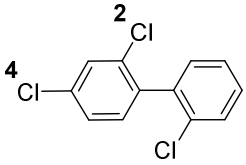

PCB-17

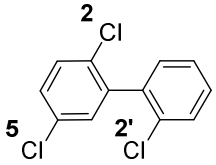

PCB-18

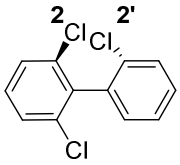

PCB-19

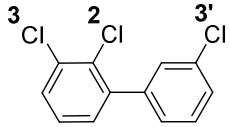

PCB-20

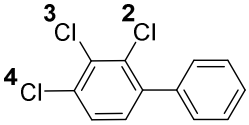

PCB-21

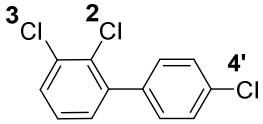

PCB-22

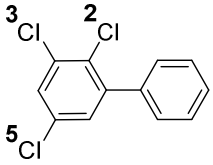

PCB-23

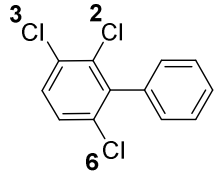

PCB-24

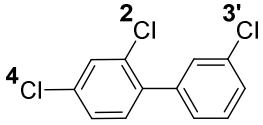

PCB-25

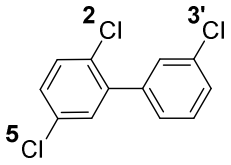

PCB-26

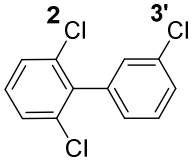

PCB-27

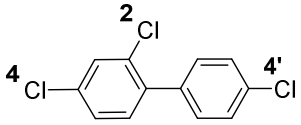

PCB-28

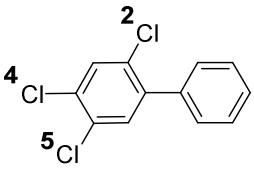

PCB-29

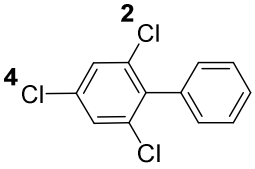

PCB-30

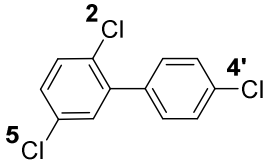

PCB-31

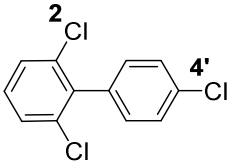

PCB-32

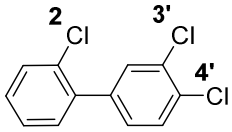

PCB-33

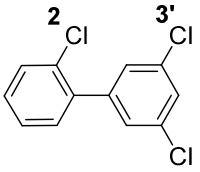

PCB-34

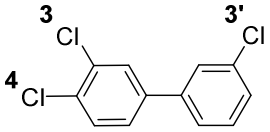

PCB-35

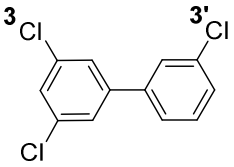

PCB-36

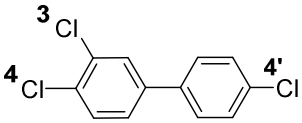

PCB-37

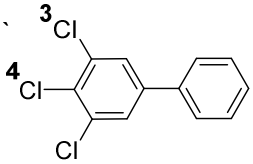

PCB-38

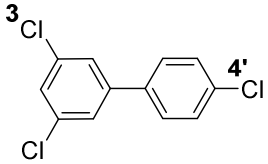

PCB-39

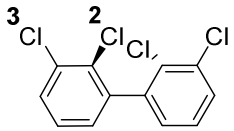

PCB-40

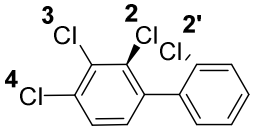

PCB-41

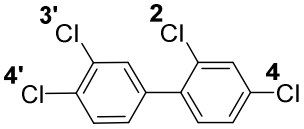

PCB-42

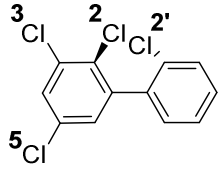

PCB-43

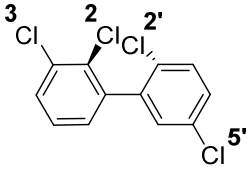

PCB-44

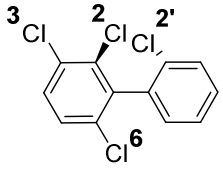

PCB-45

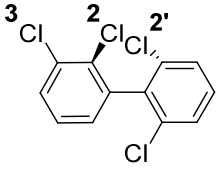

PCB-46

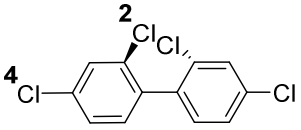

PCB-47

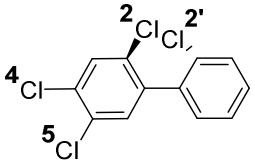

PCB-48

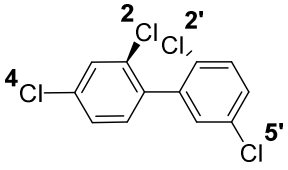

PCB-49

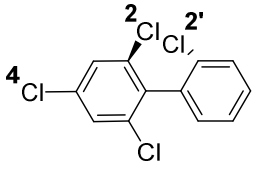

PCB-50

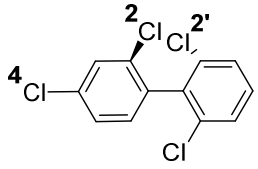

PCB-51

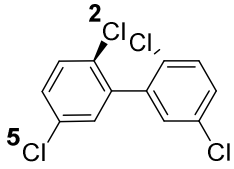

PCB-52

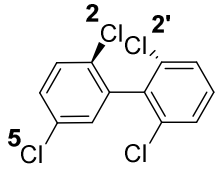

PCB-53

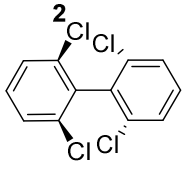

PCB-54

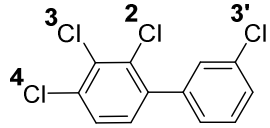

PCB-55

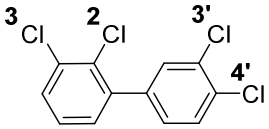

PCB-56

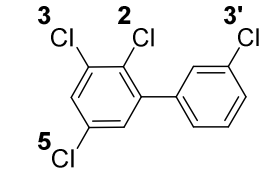
PCB-57

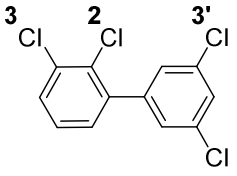
PCB-58

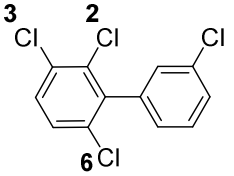
PCB-59

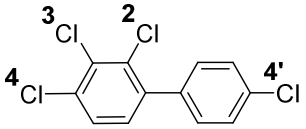
PCB-60

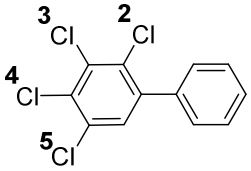
PCB-61

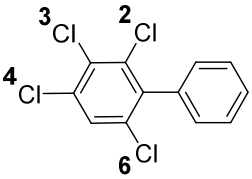
PCB-62

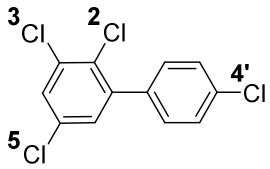
PCB-63

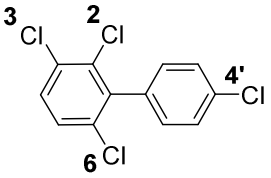
PCB-64

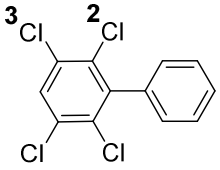
PCB-65

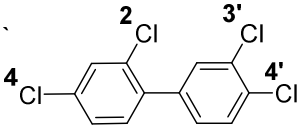
PCB-66

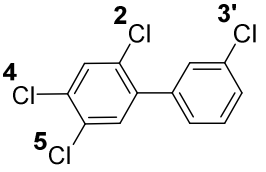
PCB-67

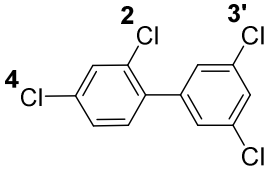
PCB-68

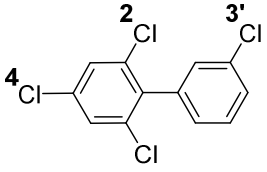
PCB-69

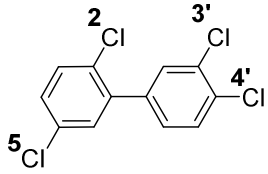
PCB-70

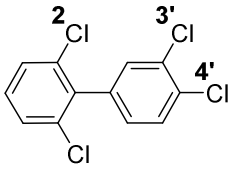
PCB-71

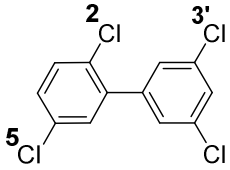
PCB-72

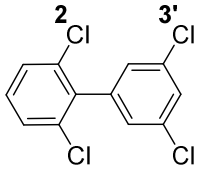
PCB-73

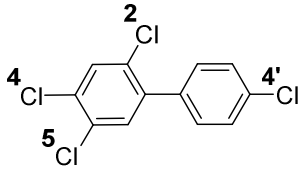
PCB-74

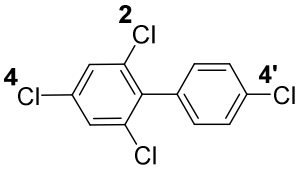
PCB-75

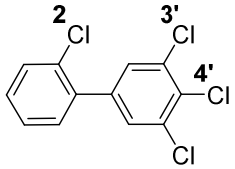
PCB-76

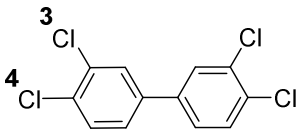
PCB-77

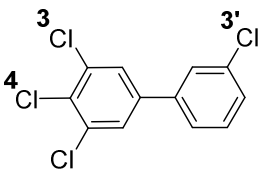
PCB-78

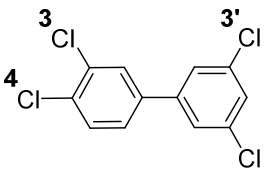
PCB-79

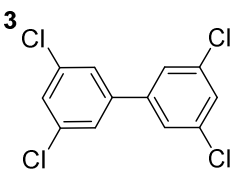
PCB-80

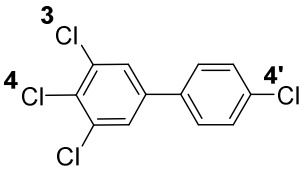
PCB-81

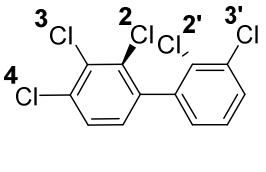
PCB-82

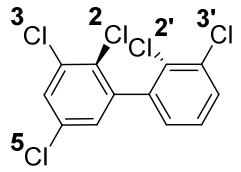
PCB-83

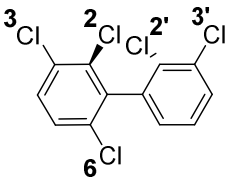
PCB-84

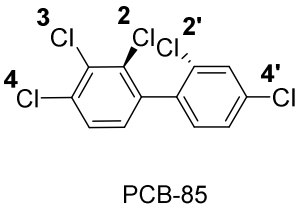

PCB-85

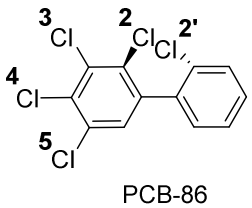

PCB-86

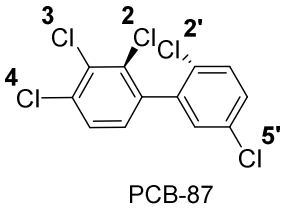

PCB-87

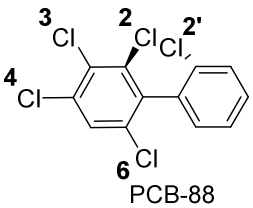

PCB-88

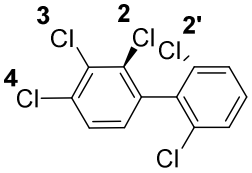

PCB-89

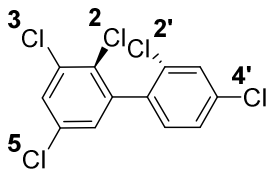

PCB-90

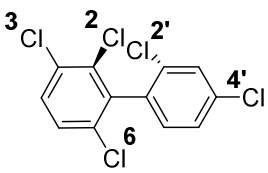

PCB-91

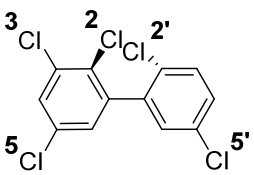

PCB-92

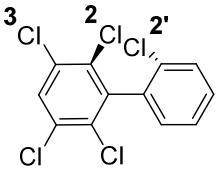

PCB-93

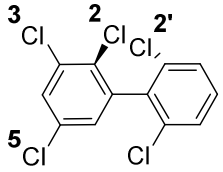

PCB-94

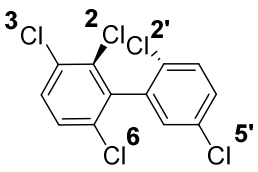

PCB-95

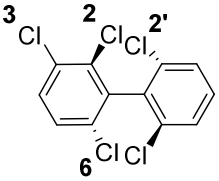

PCB-96

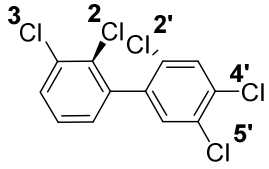

PCB-97

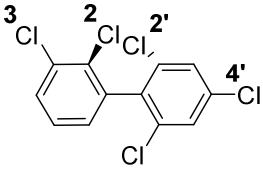

PCB-98

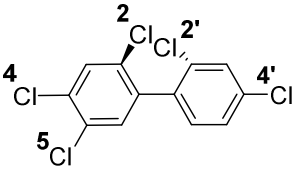

PCB-99

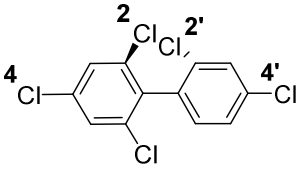

PCB-100

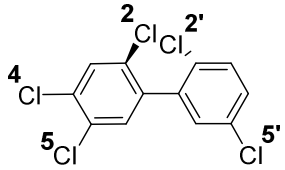

PCB-101

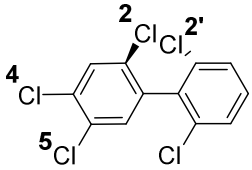

PCB-102

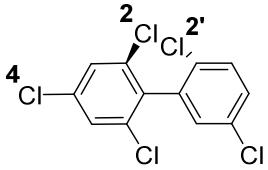

PCB-103

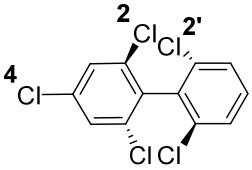

PCB-104

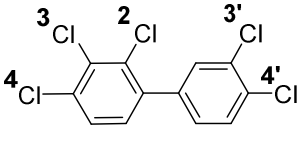

PCB-105

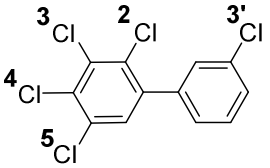

PCB-106

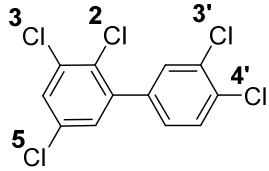

PCB-107

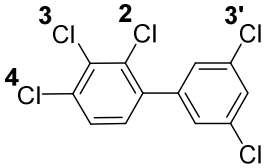

PCB-108

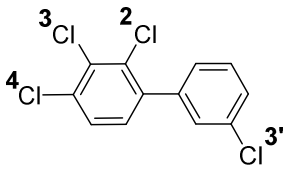

PCB-109

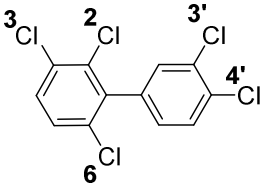

PCB-110

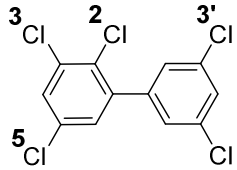

PCB-111

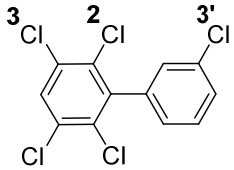

PCB-112

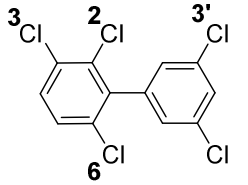
PCB-113

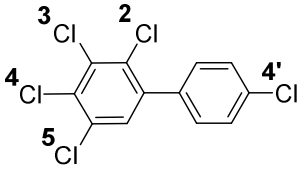
PCB-114

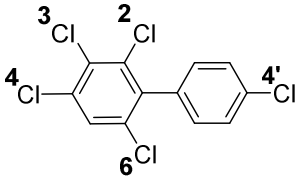
PCB-115

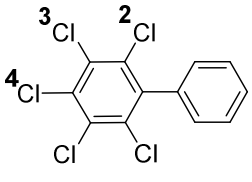
PCB-116

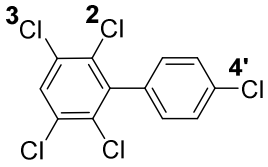
PCB-117

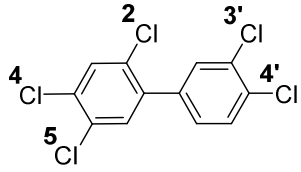
PCB-118

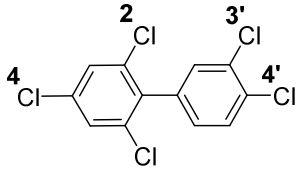
PCB-119

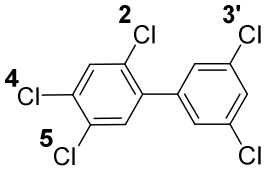
PCB-120

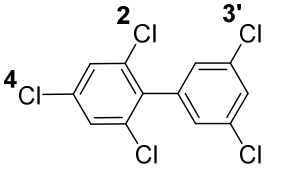
PCB-121

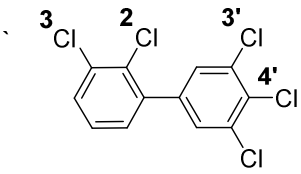
PCB-122

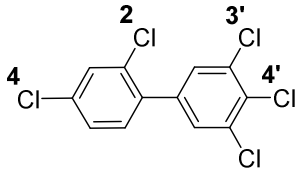
PCB-123

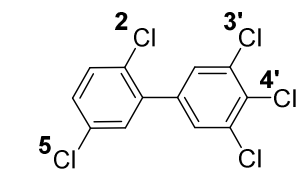
PCB-124

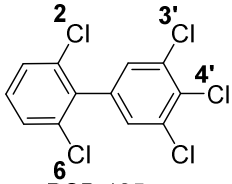
PCB-125

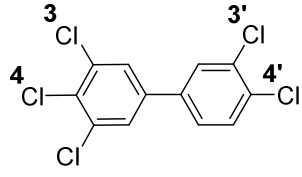
PCB-126

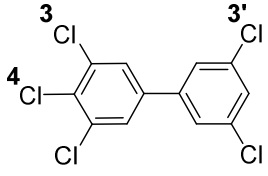
PCB-127

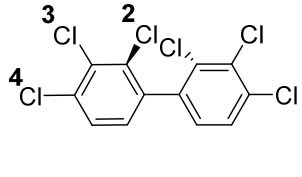
PCB-128

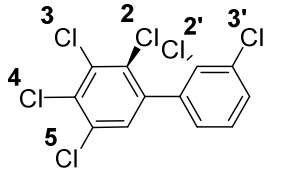
PCB-129

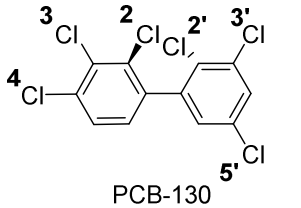
PCB-130

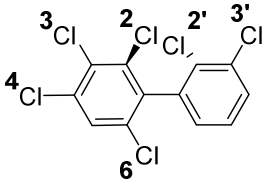
PCB-131

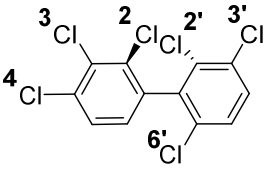
PCB-132

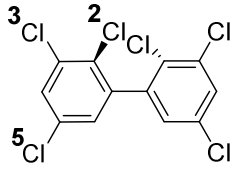
PCB-133

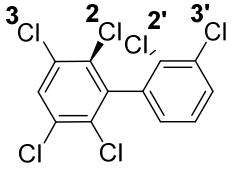
PCB-134

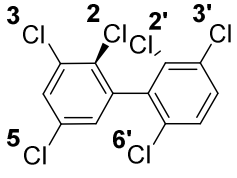
PCB-135

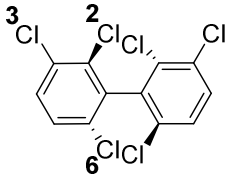
PCB-136

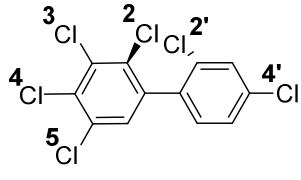
PCB-137

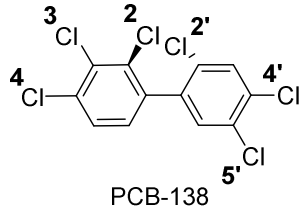
PCB-138

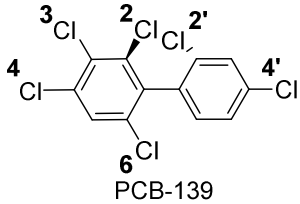
PCB-139

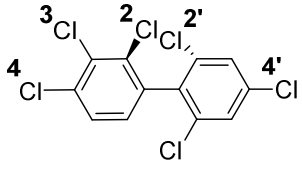
PCB-140

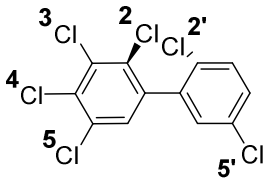
PCB-141

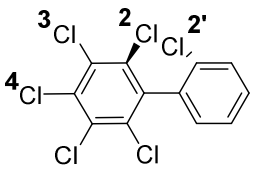
PCB-142

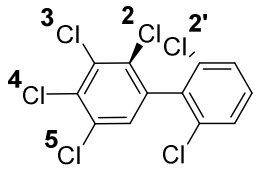
PCB-143

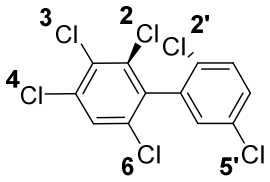
PCB-144

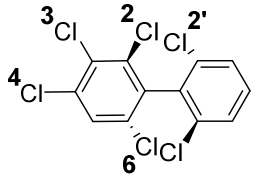
PCB-145

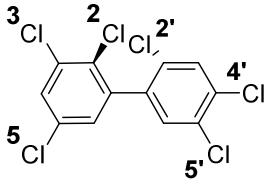
PCB-146

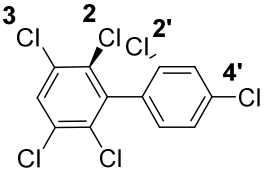
PCB-147

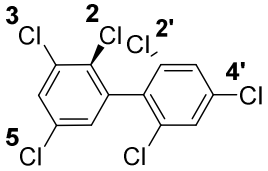
PCB-148

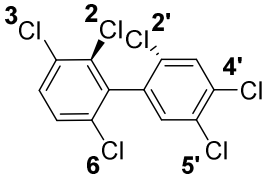
PCB-149

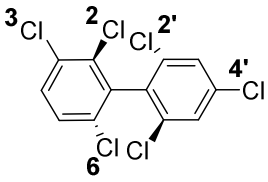
PCB-150

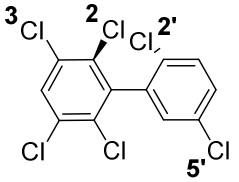
PCB-151

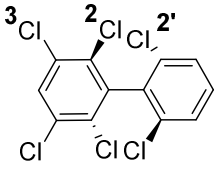
PCB-152

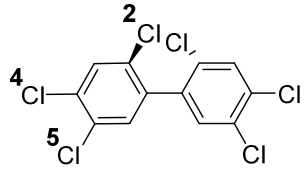
PCB-153

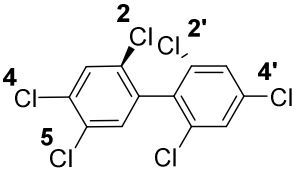
PCB-154

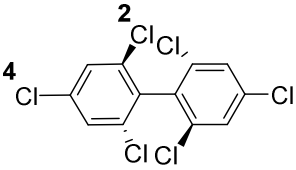
PCB-155

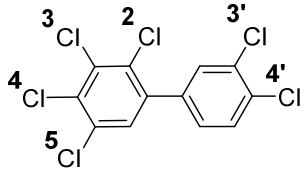
PCB-156

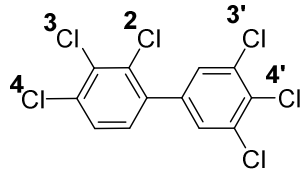
PCB-157

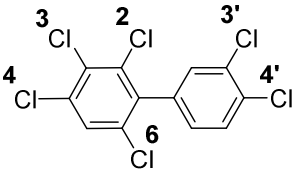
PCB-158

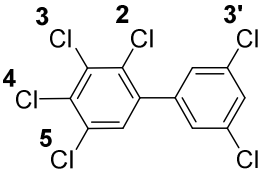
PCB-159

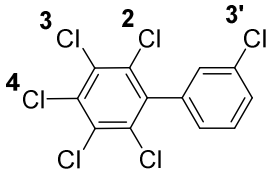
PCB-160

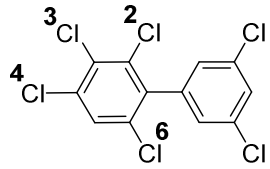
PCB-161

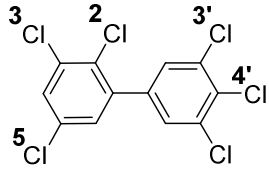
PCB-162

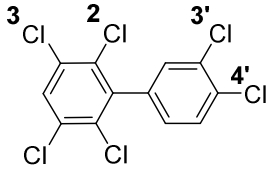
PCB-163

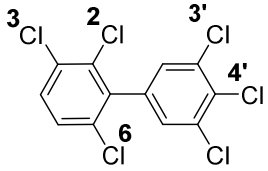
PCB-164

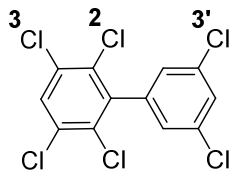
PCB-165

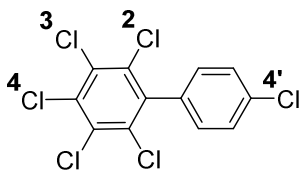
PCB-166

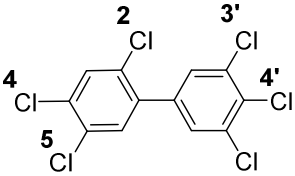
PCB-167

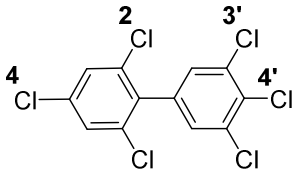
PCB-168

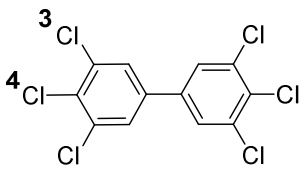
PCB-169

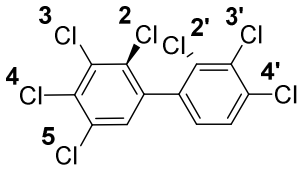
PCB-170

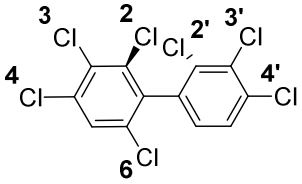
PCB-171

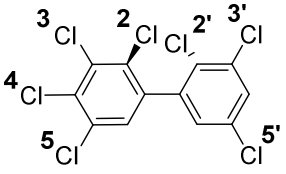
PCB-172

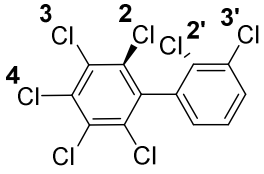
PCB-173

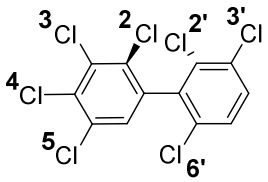
PCB-174

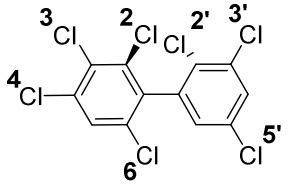
PCB-175

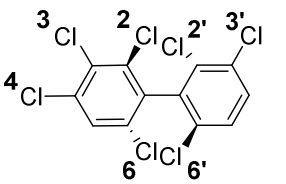
PCB-176

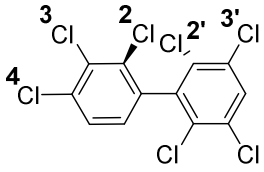
PCB-177

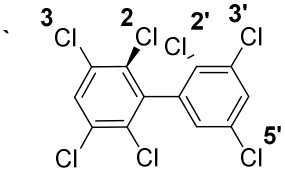
PCB-178

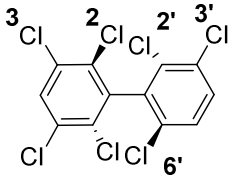
PCB-179

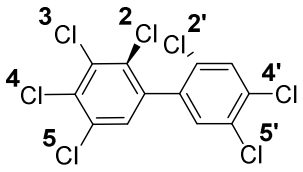
PCB-180

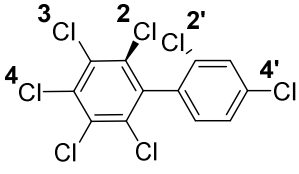
PCB-181

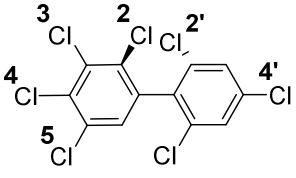
PCB-182

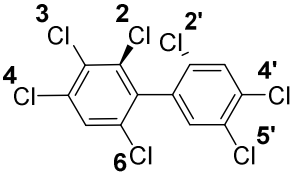
PCB-183

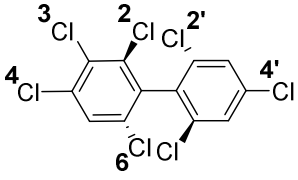
PCB-184

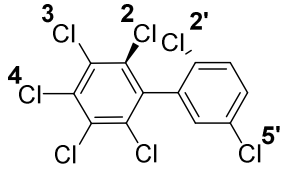
PCB-185

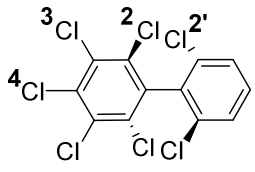
PCB-186

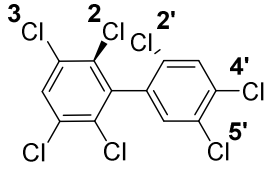
PCB-187

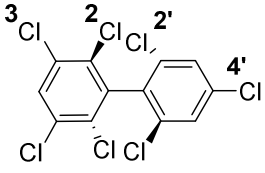
PCB-188

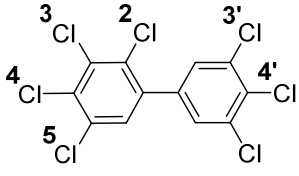
PCB-189

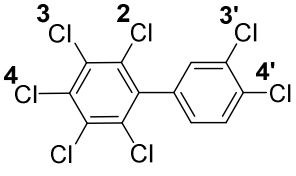
PCB-190

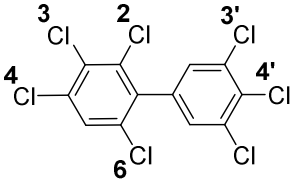
PCB-191

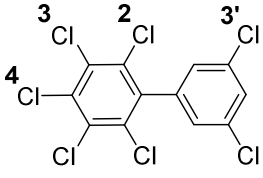
PCB-192

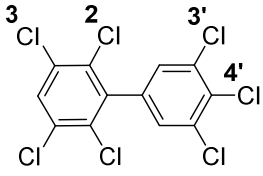
PCB-193

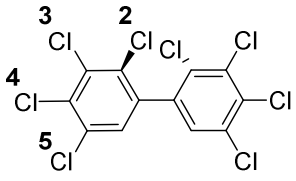
PCB-194

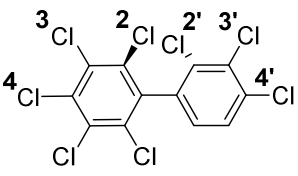
PCB-195

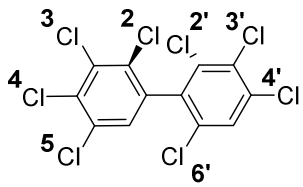
PCB-196

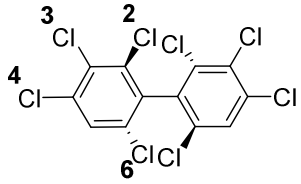
PCB-197

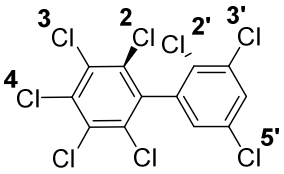
PCB-198

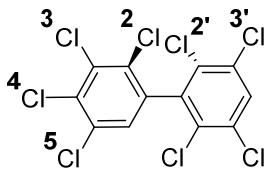
PCB-199

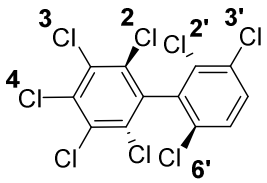
PCB-200

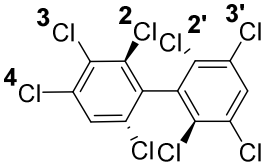
PCB-201

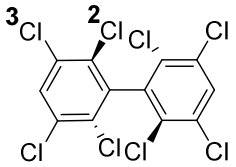
PCB-202

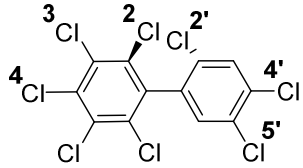
PCB-203

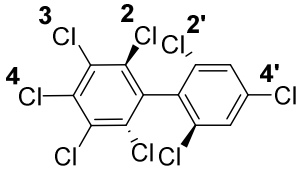
PCB-204

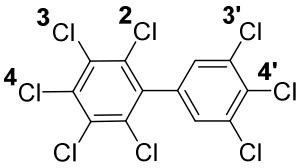
PCB-205

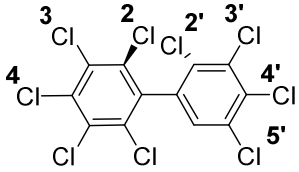
PCB-206

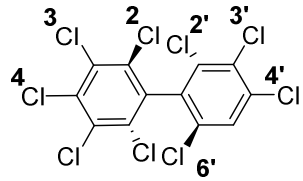
PCB-207

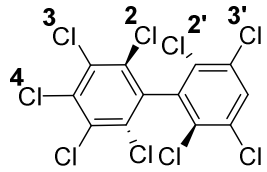
PCB-208

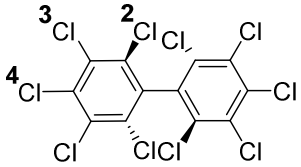
PCB-209

APPENDIX C

COMPLETE TABLE OF PCB DATA

Compound	*d*(Cl—Se), Å	Δ*d*(C-Cl), Å	ΔE + ZPE, kcal mol^{-1}	$\Delta E_{D\rightarrow A}$, kcal mol^{-1}	%X
XB-3-PCB-2	3.468	-0.010	-2.02	2.79	45.14
XB-4-PCB-3	3.441	-0.010	-2.28	3.16	45.19
XB-3-PCB-5	3.509	-0.008	-3.31	2.13	46.24
XB-2-PCB-6	3.391	-0.007	-1.81	4.07	45.13
XB-3'-PCB-6	3.428	-0.008	-2.45	3.49	45.20
XB-4-PCB-7	3.366	-0.007	-4.06	4.05	45.59
XB-4'-PCB-8	3.470	-0.012	-2.45	2.71	45.24
XB-5-PCB-9	3.381	-0.007	-3.96	3.91	45.51
XB-2-PCB-10	3.438	-0.005	-4.01	3.49	45.58
XB-3-PCB-11	3.515	-0.012	-3.22	2.06	45.30
XB-4-PCB-12	3.514	-0.010	-3.91	2.02	46.37
XB-3-PCB-13	3.414	-0.009	-3.44	3.53	45.24
XB-4'-PCB-13	3.406	-0.009	-6.24	3.77	45.32
XB-3-PCB-14	3.350	-0.006	-5.84	4.53	45.54
XB-4-PCB-15	3.411	-0.010	-3.73	3.47	45.30
XB-2-PCB-16	3.347	-0.001	-2.16	4.94	46.46
XB-3-PCB-16	3.551	-0.009	-3.43	1.79	46.33
XB-4-PCB-17	3.337	-0.006	-4.48	3.97	45.32
XB-2'-PCB-18	3.450	-0.010	-5.12	3.20	45.28
XB-2-PCB-18	3.493	-0.014	-4.09	2.34	45.52
XB-5-PCB-18	3.374	-0.008	-4.75	4.00	45.60
XB-2-PCB-19	3.379	-0.004	-4.62	3.90	45.62
XB-2'-PCB-19	3.482	-0.008	-4.47	2.93	45.30
XB-2-PCB-20	3.304	0.001	-3.55	4.71	46.37
XB-3'-PCB-20	3.505	-0.012	-2.74	2.16	45.34

XB-3-PCB-20	3.487	-0.008	-4.50	2.26	46.36
XB-3-PCB-21	3.255	0.007	-3.68	5.68	47.31
XB-4-PCB-21	3.443	-0.007	-5.37	2.67	46.56
XB-3-PCB-22	3.478	-0.007	-4.73	2.39	46.34
XB-4'-PCB-22	3.410	-0.009	-3.46	3.75	45.32
XB-2-PCB-23	3.339	0.002	-6.34	4.50	46.56
XB-3-PCB-23	3.301	0.000	-5.68	4.32	46.59
XB-5-PCB-23	3.320	-0.004	-5.68	4.04	45.84
XB-3-PCB-24	3.482	-0.007	-5.59	2.27	46.56
XB-3'-PCB-25	3.518	-0.013	-3.08	2.03	45.34
XB-4-PCB-25	3.371	-0.009	-5.47	3.76	45.69
XB-2-PCB-26	3.437	-0.008	-4.86	2.85	45.56
XB-3'-PCB-26	3.418	-0.010	-3.24	3.39	45.35
XB-5-PCB-26	3.370	-0.008	-5.52	3.90	45.62
XB-3'-PCB-27	3.451	-0.010	-2.01	2.97	45.29
XB-4'-PCB-28	3.402	-0.009	-3.54	3.85	45.33
XB-4-PCB-28	3.357	-0.008	-5.27	4.00	45.69
XB-4-PCB-29	3.298	-0.001	-5.64	4.32	46.70
XB-5-PCB-29	3.553	-0.009	-5.95	1.57	46.62
XB-2-PCB-30	3.349	-0.001	-6.34	3.91	45.85
XB-4-PCB-30	3.284	-0.001	-6.01	4.76	45.94
XB-2-PCB-31	3.411	-0.005	-7.33	3.34	45.47
XB-4'-PCB-31	3.412	-0.009	-3.48	3.45	45.35
XB-5-PCB-31	3.360	-0.007	-5.60	4.18	45.61
XB-2-PCB-32	3.441	-0.008	-5.24	2.81	45.52
XB-4'-PCB-32	3.421	-0.009	-2.37	3.46	45.27
XB-2-PCB-33	3.446	-0.009	-4.11	2.76	45.23
XB-3'-PCB-33	3.355	-0.003	-2.65	4.60	46.41
XB-4'-PCB-33	3.517	-0.010	-4.05	1.98	46.39
XB-5'-PCB-34	3.355	-0.005	-4.57	4.48	45.64

XB-3'-PCB-35	3.378	-0.007	-4.26	4.04	45.37
XB-3-PCB-35	3.326	0.000	-3.89	4.33	46.44
XB-4-PCB-35	3.501	-0.009	-5.03	2.09	46.46
XB-3'-PCB-36	3.411	-0.010	-4.46	3.35	45.40
XB-3-PCB-36	3.314	-0.004	-5.28	4.26	45.65
XB-4-PCB-37	3.465	-0.009	-5.35	2.45	46.46
XB-3-PCB-38	3.538	-0.008	-6.20	1.67	46.52
XB-4-PCB-38	3.248	0.007	-4.51	6.22	47.41
XB-3-PCB-39	3.315	-0.005	-5.83	4.27	45.64
XB-4'-PCB-39	3.356	-0.009	-5.03	4.41	45.43
XB-3-PCB-40	3.452	-0.008	-4.67	2.65	46.41
XB-3-PCB-41	3.257	0.007	-3.53	5.68	47.38
XB-4-PCB-41	3.451	-0.007	-5.26	2.56	46.58
XB-2-PCB-42	3.302	0.000	-3.62	4.64	46.50
XB-3-PCB-42	3.472	-0.008	-4.62	2.44	46.41
XB-4'-PCB-42	3.374	-0.008	-5.27	3.73	45.69
XB-2'-PCB-43	3.396	-0.006	-3.73	3.65	45.44
XB-3-PCB-43	3.309	-0.001	-5.27	4.06	46.67
XB-5-PCB-43	3.312	-0.005	-5.83	4.16	45.89
XB-2'-PCB-45	3.456	-0.007	-5.63	2.52	45.37
XB-3-PCB-45	3.434	-0.006	-5.53	2.81	46.63
XB-6-PCB-45	3.358	-0.005	-6.29	3.91	45.86
XB-2-PCB-46	3.329	0.000	-3.31	4.40	46.44
XB-3-PCB-46	3.499	-0.009	-3.66	2.18	46.38
XB-2-PCB-47	3.318	-0.004	-4.99	3.96	45.75
XB-4-PCB-47	3.319	-0.006	-5.81	4.18	45.71
XB-2'-PCB-48	3.357	-0.006	-3.96	3.53	45.41
XB-4-PCB-48	3.287	0.000	-5.52	4.52	46.72
XB-5-PCB-48	3.307	-0.001	-5.82	4.18	46.67
XB-2-PCB-49	3.318	-0.003	-5.01	3.97	45.77

XB-4-PCB-49	3.366	-0.007	-5.35	3.86	45.72
XB-2'-PCB-49	3.371	-0.005	-5.15	3.89	45.73
XB-5'-PCB-49	3.388	-0.007	-5.53	3.58	45.67
XB-2'-PCB-50	3.390	-0.007	-3.59	3.99	45.35
XB-4-PCB-50	3.304	-0.003	-6.43	4.37	45.97
XB-2-PCB-51	3.339	-0.004	-4.49	3.90	45.69
XB-4-PCB-51	3.355	-0.007	-4.45	4.18	45.65
XB-2-PCB-52	3.359	0.004	-5.36	3.33	45.74
XB-5-PCB-52	3.354	-0.007	-5.49	4.26	45.68
XB-2'-PCB-53	3.388	-0.005	-5.06	3.56	45.70
XB-2-PCB-53	3.354	-0.004	-4.45	3.61	45.66
XB-5-PCB-53	3.385	-0.007	-4.18	3.73	45.63
XB-2-PCB-54	3.358	-0.006	-4.09	3.62	45.63
XB-2-PCB-55	3.243	0.005	-5.56	5.16	45.28
XB-3'-PCB-55	3.490	-0.012	-3.74	2.26	44.97
XB-3-PCB-55	3.238	0.008	-5.43	6.01	46.89
XB-4-PCB-55	3.454	-0.007	-6.93	2.49	46.39
XB-2-PCB-56	3.253	0.001	-4.45	5.28	46.39
XB-3'-PCB-56	3.331	0.000	-3.71	4.26	46.50
XB-3-PCB-56	3.464	-0.009	-5.63	2.45	46.42
XB-4'-PCB-56	3.505	-0.009	-5.15	2.07	46.45
XB-2-PCB-57	3.245	0.005	-5.67	5.14	46.67
XB-3'-PCB-57	3.419	-0.010	-4.01	3.25	45.44
XB-3-PCB-57	3.339	-0.004	-6.70	3.49	46.69
XB-5-PCB-57	3.295	-0.003	-6.95	4.64	45.94
XB-2-PCB-58	3.374	-0.009	-8.93	4.85	46.43
XB-3'-PCB-58	3.337	-0.007	-4.89	3.78	45.69
XB-3-PCB-58	3.382	-0.005	-6.00	3.47	46.46
XB-3'-PCB-59	3.432	-0.009	-3.23	3.13	45.37
XB-3-PCB-59	3.406	-0.006	-6.88	3.09	46.66

XB-3-PCB-60	3.229	0.005	-5.61	6.23	47.31
XB-4'-PCB-60	3.390	-0.006	-4.28	3.96	45.51
XB-4-PCB-60	3.416	-0.004	-6.88	2.92	46.77
XB-3-PCB-61	3.224	0.012	-5.83	6.27	47.49
XB-4-PCB-61	3.218	0.012	-6.14	6.44	47.57
XB-5-PCB-61	3.252	0.003	-7.18	5.26	46.78
XB-3-PCB-62	3.220	0.011	-6.16	6.41	47.56
XB-4-PCB-62	3.256	0.003	-6.94	4.93	46.86
XB-6-PCB-62	3.268	0.002	-7.18	4.80	46.11
XB-3-PCB-63	3.258	0.002	-7.03	5.25	46.68
XB-5-PCB-63	3.279	-0.003	-7.07	4.81	45.93
XB-3-PCB-64	3.443	-0.008	-7.18	2.63	46.64
XB-6-PCB-64	3.327	-0.005	-6.83	3.84	45.83
XB-4'-PCB-64	3.411	-0.009	-3.00	3.72	45.35
XB-2-PCB-65	3.237	0.007	-6.70	4.91	46.88
XB-3-PCB-65	3.249	0.005	-7.08	5.17	46.85
XB-2-PCB-66	3.281	-0.002	-5.97	4.49	45.63
XB-3'-PCB-66	3.329	-0.001	-4.03	4.28	46.50
XB-4'-PCB-66	3.484	-0.009	-5.36	2.24	46.47
XB-4-PCB-66	3.341	-0.007	-6.56	3.56	45.76
XB-2-PCB-67	3.266	0.000	-6.61	4.78	45.88
XB-4-PCB-67	3.321	-0.002	-6.74	3.79	46.78
XB-5-PCB-67	3.281	0.002	-6.44	5.05	46.71
XB-3'-PCB-67	3.445	-0.010	-4.25	2.86	45.42
XB-2-PCB-68	3.268	-0.001	-6.61	4.75	45.67
XB-3'-PCB-68	3.301	-0.004	-5.40	4.61	45.71
XB-4-PCB-68	3.321	-0.006	-6.92	3.94	45.79
XB-5'-PCB-68	3.321	-0.004	-5.76	4.17	45.75
XB-2-PCB-69	3.278	0.001	-7.89	4.48	45.97
XB-3'-PCB-69	3.431	-0.009	-3.38	3.14	45.40

XB-4-PCB-69	3.291	-0.002	-7.09	4.59	46.03
XB-2-PCB-70	3.385	-0.006	-6.26	3.41	45.60
XB-3'-PCB-70	3.325	0.000	-4.05	4.44	46.50
XB-4'-PCB-70	3.467	-0.009	-5.01	2.41	46.49
XB-5-PCB-70	3.341	-0.005	-6.51	3.74	45.70
XB-2-PCB-71	3.423	-0.007	-6.68	2.90	45.63
XB-3'-PCB-71	3.446	-0.007	-3.66	2.64	46.46
XB-4'-PCB-71	3.479	-0.009	-3.92	2.36	46.41
XB-2-PCB-72	3.298	-0.003	-6.73	4.22	45.63
XB-5-PCB-72	3.361	-0.007	-6.40	3.93	45.75
XB-3'-PCB-72	3.313	-0.004	-5.62	4.20	45.75
XB-2-PCB-73	3.422	-0.006	-6.49	3.02	45.66
XB-3'-PCB-73	3.321	-0.005	-4.49	4.45	45.70
XB-4'-PCB-74	3.392	-0.010	-4.40	3.68	45.52
XB-4-PCB-74	3.275	0.001	-6.82	4.64	46.78
XB-5-PCB-74	3.323	-0.003	-6.92	3.67	46.70
XB-4'-PCB-75	3.407	-0.008	-3.28	3.80	45.36
XB-4-PCB-75	3.253	-0.001	-7.75	5.27	46.04
XB-2-PCB-76	3.351	-0.005	-5.31	3.43	45.29
XB-3'-PCB-76	3.260	0.003	-6.30	5.25	46.61
XB-4'-PCB-76	3.258	0.008	-4.05	5.72	47.44
XB-3-PCB-77	3.285	0.001	-5.08	4.49	46.51
XB-4-PCB-77	3.279	-0.001	-5.62	5.28	46.53
XB-3'-PCB-78	3.416	-0.010	-5.16	3.15	45.46
XB-3-PCB-78	3.293	0.000	-6.63	4.15	46.61
XB-4-PCB-78	3.223	0.009	-5.65	6.60	47.50
XB-3'-PCB-79	3.301	-0.004	-6.41	4.40	45.73
XB-3-PCB-79	3.547	-0.010	-6.10	1.59	46.53
XB-4-PCB-79	3.445	-0.008	-6.16	2.59	46.55
XB-3-PCB-80	3.299	-0.004	-6.71	4.42	45.78

XB-3-PCB-81	3.631	-0.009	-7.45	1.13	46.61
XB-4-PCB-81	3.240	0.010	-5.39	6.01	47.49
XB-4'-PCB-81	3.361	-0.008	-5.62	4.09	45.48
XB-2'-PCB-82	3.361	-0.001	-7.35	3.71	46.52
XB-3'-PCB-82	3.418	-0.007	-5.46	3.01	46.47
XB-3-PCB-82	3.232	0.009	-5.06	6.11	47.46
XB-4-PCB-82	3.433	-0.006	-6.74	2.69	46.64
XB-2'-PCB-83	3.351	-0.001	-7.21	3.79	46.57
XB-3'-PCB-83	3.453	-0.008	-5.53	2.55	46.49
XB-3-PCB-83	3.316	-0.003	-6.33	3.85	46.74
XB-5-PCB-83	3.292	-0.002	-6.78	4.41	45.98
XB-2'-PCB-84	3.391	0.000	-6.82	3.42	46.50
XB-3'-PCB-84	3.498	-0.008	-4.34	2.15	46.45
XB-2-PCB-84	3.392	0.000	-6.82	3.41	46.73
XB-3-PCB-84	3.319	-0.002	-6.46	3.86	46.69
XB-2-PCB-85	3.236	0.006	-6.02	5.37	46.69
XB-3-PCB-85	3.228	0.008	-5.43	6.19	47.46
XB-2'-PCB-85	3.378	0.001	-8.57	3.62	45.79
XB-4'-PCB-85	3.327	-0.006	-6.11	3.99	45.75
XB-4-PCB-85	3.388	-0.005	-6.89	3.24	46.66
XB-2'-PCB-86	3.422	-0.007	-7.04	2.77	45.47
XB-3-PCB-86	3.205	0.014	-5.82	6.81	47.57
XB-4-PCB-86	3.213	0.011	-6.33	6.52	47.59
XB-5-PCB-86	3.269	0.001	-7.49	4.57	46.82
XB-3-PCB-87	3.230	0.010	-5.67	6.16	47.47
XB-4-PCB-87	3.423	-0.006	-6.72	2.82	46.66
XB-5'-PCB-87	3.348	-0.006	-6.56	4.25	45.72
XB-2'-PCB-88	3.364	-0.006	-4.34	3.41	45.40
XB-3-PCB-88	3.222	0.011	-6.06	6.26	47.62
XB-4-PCB-88	3.217	0.007	-7.55	5.90	46.89

XB-2-PCB-89	3.270	0.004	-5.28	4.80	46.64
XB-3-PCB-89	3.241	0.008	-4.17	5.93	47.43
XB-4-PCB-89	3.272	0.001	-5.67	4.93	46.61
XB-3-PCB-90	3.279	0.000	-6.79	4.57	46.73
XB-4'-PCB-90	3.353	-0.007	-6.37	4.01	45.79
XB-5-PCB-90	3.276	-0.001	-7.39	4.66	45.99
XB-2'-PCB-90	3.362	-0.004	-8.50	3.37	45.82
XB-3-PCB-91	3.405	-0.004	-6.75	3.08	46.71
XB-4'-PCB-91	3.328	-0.005	-5.33	3.92	45.73
XB-6-PCB-91	3.319	0.001	-8.82	4.31	45.97
XB-2'-PCB-92	3.374	-0.006	-8.30	3.23	45.79
XB-2-PCB-92	3.254	0.004	-6.12	5.04	46.80
XB-3-PCB-92	3.290	0.001	-6.71	4.31	46.76
XB-5'-PCB-92	3.356	-0.007	-6.20	4.02	45.76
XB-5-PCB-92	3.289	-0.003	-6.87	4.42	46.00
XB-2'-PCB-93	3.433	-0.008	-6.96	2.70	45.39
XB-3-PCB-93	3.242	0.005	-7.40	5.28	46.90
XB-2'-PCB-94	3.328	-0.004	-6.26	3.56	45.73
XB-2-PCB-94	3.278	0.004	-5.80	4.84	46.74
XB-3-PCB-94	3.294	0.001	-5.70	4.32	46.73
XB-5-PCB-94	3.300	-0.003	-5.84	4.29	45.97
XB-2'-PCB-95	3.324	-0.002	-5.47	4.00	45.72
XB-2-PCB-95	3.244	0.005	-5.82	5.14	46.75
XB-3-PCB-95	3.343	-0.002	-6.72	3.46	46.73
XB-5'-PCB-95	3.338	-0.005	-4.97	4.01	45.73
XB-6-PCB-95	3.304	0.000	-7.01	3.91	45.98
XB-2'-PCB-96	3.333	-0.003	-5.57	3.77	45.70
XB-2-PCB-96	3.259	0.006	-5.57	5.26	46.74
XB-3-PCB-96	3.453	-0.007	-5.69	2.55	46.68
XB-6-PCB-96	3.284	-0.001	-6.33	4.85	45.93

XB-2-PCB-97	3.261	0.003	-5.08	5.23	46.55
XB-3-PCB-97	3.399	-0.006	-5.82	3.24	46.48
XB-4'-PCB-97	3.278	0.001	-6.61	4.64	46.74
XB-5'-PCB-97	3.282	0.002	-6.83	4.63	46.78
XB-3-PCB-98	3.457	-0.009	-4.81	2.56	46.45
XB-2'-PCB-98	3.335	0.000	-8.87	4.11	46.02
XB-4'-PCB-98	3.258	0.000	-7.35	5.19	46.05
XB-2-PCB-99	3.278	0.001	-6.95	4.64	46.04
XB-2'-PCB-99	3.278	-0.001	-6.17	4.58	45.81
XB-4'-PCB-99	3.342	-0.007	-6.38	3.57	45.78
XB-5-PCB-99	3.257	0.004	-6.48	5.22	46.76
XB-4-PCB-99	3.268	0.001	-6.83	4.77	46.79
XB-2'-PCB-100	3.295	-0.003	-5.82	4.43	45.73
XB-4-PCB-100	3.266	-0.001	-7.32	4.80	46.06
XB-4'-PCB-100	3.362	-0.007	-5.70	3.92	45.73
XB-2'-PCB-101	3.340	-0.004	-6.28	3.43	45.78
XB-2-PCB-101	3.278	0.000	-6.66	4.61	46.06
XB-4-PCB-101	3.275	0.001	-6.68	4.60	46.80
XB-5'-PCB-101	3.326	-0.006	-6.33	3.93	45.75
XB-5-PCB-101	3.254	0.003	-6.24	5.22	46.77
XB-2-PCB-102	3.287	0.001	-6.39	4.63	46.00
XB-4-PCB-102	3.287	0.000	-5.55	4.44	46.73
XB-5-PCB-102	3.298	0.002	-5.29	4.68	46.74
XB-2'-PCB-102	3.446	-0.005	-6.42	2.66	45.69
XB-2'-PCB-103	3.323	-0.003	-6.01	4.02	45.72
XB-2-PCB-103	3.263	0.004	-7.54	4.71	46.07
XB-4-PCB-103	3.261	-0.001	-7.40	4.99	46.05
XB-5'-PCB-103	3.382	-0.006	-5.50	3.61	45.74
XB-2'-PCB-104	3.327	-0.003	-5.50	3.91	45.68
XB-2-PCB-104	3.270	0.001	-6.36	4.93	46.00

XB-4-PCB-104	3.294	-0.001	-6.04	4.61	46.01
XB-2-PCB-105	3.316	-0.006	-10.89	2.94	46.60
XB-3-PCB-105	3.221	0.011	-6.45	6.44	47.46
XB-4-PCB-105	3.375	-0.005	-7.75	2.90	46.70
XB-3'-PCB-105	3.311	0.000	-4.58	4.55	46.55
XB-4'-PCB-105	3.487	-0.009	-5.87	2.18	46.52
XB-2-PCB-106	3.199	0.007	-7.25	5.79	46.82
XB-3'-PCB-106	3.396	-0.009	-4.58	3.62	45.48
XB-3-PCB-106	3.187	0.014	-7.39	7.15	47.58
XB-4-PCB-106	3.198	0.013	-7.52	6.88	47.64
XB-5-PCB-106	3.431	-0.008	-8.68	2.47	46.86
XB-3'-PCB-107	3.299	0.002	-5.01	4.79	46.59
XB-3-PCB-107	3.236	0.004	-7.85	5.45	46.75
XB-5-PCB-107	3.261	-0.001	-8.19	5.05	46.02
XB-4'-PCB-107	3.474	-0.010	-5.96	2.31	46.54
XB-3'-PCB-108	3.300	-0.004	-5.89	4.41	45.80
XB-3-PCB-108	3.210	0.011	-6.49	6.64	47.49
XB-4-PCB-108	3.270	0.000	-7.78	4.65	46.73
XB-3'-PCB-109	3.379	-0.008	-4.10	3.93	45.45
XB-3-PCB-109	3.202	0.013	-7.37	6.91	47.66
XB-4-PCB-109	3.233	0.005	-8.47	5.36	46.95
XB-3'-PCB-110	3.534	-0.008	-4.54	1.76	46.53
XB-4'-PCB-110	3.455	-0.009	-4.57	2.55	46.49
XB-2-PCB-110	3.223	0.007	-6.33	5.24	46.73
XB-3-PCB-110	3.364	-0.004	-7.65	3.10	46.72
XB-6-PCB-110	3.318	-0.011	-7.58	3.82	45.90
XB-3'-PCB-111	3.316	-0.004	-6.19	4.12	45.81
XB-3-PCB-111	3.259	0.003	-8.18	4.92	46.78
XB-5'-PCB-111	3.299	-0.002	-6.59	4.50	45.84
XB-5-PCB-111	3.281	-0.002	-8.18	4.53	46.06

XB-3-PCB-112	3.239	0.006	-8.36	5.12	46.94
XB-3'-PCB-112	3.442	-0.010	-3.88	2.88	45.45
XB-2-PCB-112	3.241	0.004	-9.02	4.73	46.95
XB-2-PCB-113	3.200	0.006	-6.61	5.20	46.77
XB-3'-PCB-113	3.329	-0.005	-5.18	3.97	45.77
XB-3-PCB-113	3.325	-0.002	-7.86	3.69	46.75
XB-6-PCB-113	3.292	0.000	-9.17	4.49	45.98
XB-3-PCB-114	3.023	-0.007	-7.81	7.29	47.56
XB-4-PCB-114	3.198	0.014	-7.67	6.94	47.64
XB-5-PCB-114	3.270	0.002	-8.67	4.47	46.86
XB-4'-PCB-114	3.363	-0.008	-5.03	4.25	45.47
XB-3-PCB-115	3.194	0.013	-7.48	7.08	47.64
XB-4'-PCB-115	3.401	-0.010	-4.24	3.52	45.41
XB-6-PCB-115	3.237	0.003	-8.78	5.24	46.16
XB-4-PCB-115	3.228	0.005	-8.53	5.49	46.94
XB-3-PCB-116	3.187	0.014	-7.49	7.03	47.71
XB-4-PCB-116	3.167	0.021	-7.84	7.80	47.72
XB-3-PCB-117	3.266	0.001	-8.63	4.69	46.93
XB-4'-PCB-117	3.392	-0.009	-4.37	3.65	45.42
XB-2-PCB-118	3.344	-0.001	-10.70	4.17	45.91
XB-4-PCB-118	3.263	0.001	-7.81	4.85	46.84
XB-5-PCB-118	3.265	0.003	-7.34	5.24	46.78
XB-3'-PCB-118	3.300	0.001	-4.97	4.77	46.57
XB-4'-PCB-118	3.437	-0.008	-6.07	2.69	46.55
XB-3'-PCB-119	3.323	-0.001	-4.29	4.39	46.53
XB-4'-PCB-119	3.472	-0.009	-5.01	2.35	46.49
XB-2-PCB-119	3.290	0.002	-9.98	4.87	46.00
XB-4-PCB-119	3.258	-0.002	-8.29	4.94	46.10
XB-3'-PCB-120	3.315	-0.004	-6.28	4.12	45.81
XB-4-PCB-120	3.253	0.002	-7.69	4.97	46.87

XB-5-PCB-120	3.296	-0.002	-7.80	4.04	46.81
XB-2-PCB-121	3.208	0.005	-8.86	6.24	46.03
XB-3'-PCB-121	3.320	-0.003	-7.10	4.31	45.78
XB-4-PCB-121	3.257	0.000	-8.85	4.91	46.13
XB-3-PCB-122	3.380	-0.005	-6.66	3.46	46.50
XB-4'-PCB-122	3.245	0.009	-5.15	5.92	47.50
XB-3'-PCB-122	3.266	0.005	-5.92	5.30	46.64
XB-3'-PCB-123	3.261	0.004	-6.12	5.44	46.66
XB-4'-PCB-123	3.231	0.008	-5.92	6.05	47.50
XB-2-PCB-123	3.363	-0.014	-11.48	1.84	45.68
XB-4-PCB-123	3.306	-0.005	-7.57	4.14	45.84
XB-2-PCB-124	3.286	-0.003	-8.13	4.31	45.64
XB-3'-PCB-124	3.340	-0.004	-6.65	3.31	46.69
XB-4'-PCB-124	3.229	0.009	-5.69	6.28	47.52
XB-5-PCB-124	3.355	-0.008	-7.40	3.98	45.79
XB-2-PCB-125	3.431	-0.007	-7.47	2.84	45.68
XB-3'-PCB-125	3.455	-0.006	-5.91	2.40	46.66
XB-4'-PCB-125	3.237	0.008	-4.74	6.32	47.46
XB-4-PCB-126	3.211	0.009	-6.56	6.43	47.55
XB-3'-PCB-126	3.588	-0.009	-6.99	1.34	46.57
XB-4'-PCB-126	3.305	-0.004	-6.93	4.12	46.60
XB-3'-PCB-127	3.285	-0.001	-7.37	4.61	45.83
XB-3-PCB-127	3.485	-0.008	-7.93	1.98	46.72
XB-4-PCB-127	3.212	0.010	-6.86	6.50	47.57
XB-3-PCB-128	3.229	0.004	-8.62	5.60	46.76
XB-4-PCB-128	3.212	0.012	-7.25	6.72	47.61
XB-2'-PCB-129	3.244	0.004	-5.28	5.59	46.58
XB-3'-PCB-129	3.438	-0.008	-6.26	2.67	46.53
XB-3-PCB-129	3.186	0.014	-7.04	7.12	47.62
XB-4-PCB-129	3.199	0.013	-7.34	6.85	47.64

XB-5-PCB-129	3.228	0.005	-8.34	5.75	46.89
XB-2-PCB-130	3.218	0.008	-6.90	5.61	46.76
XB-2'-PCB-130	3.308	0.008	-9.37	4.16	46.82
XB-3'-PCB-130	3.226	0.003	-7.45	5.90	46.72
XB-3-PCB-130	3.211	0.010	-6.24	6.56	47.52
XB-4-PCB-130	3.307	-0.002	-7.72	3.91	46.72
XB-5'-PCB-130	3.268	-0.001	-8.18	4.78	46.04
XB-3'-PCB-131	3.428	-0.007	-5.46	2.83	46.51
XB-3-PCB-131	3.188	0.015	-7.19	7.19	47.52
XB-4-PCB-131	3.307	0.000	-8.43	3.91	46.72
XB-3'-PCB-132	3.323	-0.002	-7.77	3.73	46.75
XB-3-PCB-132	3.228	0.010	-5.31	6.20	47.49
XB-4-PCB-132	3.311	-0.002	-6.49	3.86	46.68
XB-2-PCB-133	3.293	0.002	-11.81	4.54	46.86
XB-3-PCB-133	3.286	0.000	-7.71	4.28	46.81
XB-5-PCB-133	3.261	-0.001	-7.77	4.88	46.08
XB-2'-PCB-134	3.359	-0.002	-8.16	3.75	46.99
XB-3'-PCB-134	3.413	-0.006	-5.48	3.03	46.96
XB-3-PCB-134	3.245	0.003	-8.09	5.13	46.51
XB-3-PCB-136	3.331	-0.002	-6.57	3.62	46.75
XB-6-PCB-136	3.279	-0.001	-7.10	4.63	45.99
XB-2'-PCB-137	3.273	-0.002	-6.49	4.57	45.84
XB-4'-PCB-137	3.334	-0.006	-7.15	3.64	45.83
XB-2-PCB-137	3.207	0.008	-7.87	5.89	46.93
XB-3-PCB-137	3.183	0.014	-7.59	7.22	47.62
XB-4-PCB-137	3.190	0.014	-7.46	7.03	47.65
XB-5-PCB-137	3.233	0.007	-8.26	5.76	46.91
XB-2-PCB-138	3.213	0.008	-7.20	5.67	46.74
XB-3-PCB-138	3.211	0.012	-6.55	6.62	47.52
XB-2'-PCB-138	3.263	-0.001	-7.76	4.77	46.06

XB-4-PCB-138	3.247	0.003	-7.81	5.37	46.72
XB-4'-PCB-138	3.255	0.002	-7.52	5.01	46.84
XB-5'-PCB-138	3.243	0.005	-7.67	5.57	46.79
XB-3-PCB-139	3.187	0.014	-7.58	7.04	47.70
XB-4'-PCB-139	3.314	-0.005	-6.31	4.08	45.78
XB-4-PCB-139	3.209	0.009	-8.83	6.06	46.96
XB-6-PCB-139	3.233	0.004	-9.65	5.46	46.23
XB-2-PCB-140	3.229	0.007	-6.70	5.69	46.68
XB-3-PCB-140	3.220	0.012	-5.69	6.43	47.50
XB-4-PCB-140	3.285	0.000	-6.73	4.40	46.67
XB-4'-PCB-140	3.256	-0.001	-8.20	4.95	46.10
XB-2-PCB-141	3.212	0.008	-7.93	5.58	46.95
XB-3-PCB-141	3.173	0.016	-7.42	7.54	47.63
XB-4-PCB-141	3.185	0.015	-7.22	7.32	47.66
XB-5'-PCB-141	3.357	-0.007	-6.93	3.93	45.80
XB-5-PCB-141	3.215	0.006	-8.18	6.05	46.92
XB-2'-PCB-142	3.359	-0.005	-4.75	3.40	45.44
XB-3-PCB-142	3.174	0.018	-7.50	7.45	47.76
XB-4-PCB-142	3.154	0.022	-7.80	8.18	47.74
XB-2'-PCB-143	3.297	-0.003	-7.17	3.94	45.74
XB-2-PCB-143	3.232	0.008	-7.27	5.79	46.89
XB-3-PCB-143	3.190	0.015	-6.21	6.94	47.60
XB-4-PCB-143	3.202	0.013	-6.51	6.74	47.60
XB-5-PCB-143	3.240	0.005	-6.95	5.23	46.90
XB-2'-PCB-144	3.302	-0.003	-6.55	4.28	45.74
XB-2-PCB-144	3.182	0.014	-8.23	6.38	46.96
XB-3-PCB-144	3.192	0.014	-7.39	6.88	47.71
XB-4-PCB-144	3.220	0.007	-8.45	5.63	46.97
XB-5'-PCB-144	3.344	-0.006	-5.98	3.63	45.77
XB-6-PCB-144	3.225	0.005	-8.80	5.91	46.28

XB-2'-PCB-145	3.292	-0.003	-6.45	4.40	45.72
XB-2-PCB-145	3.214	0.009	-7.61	6.00	46.92
XB-3-PCB-145	3.217	0.012	-5.98	6.39	47.66
XB-4-PCB-145	3.242	0.004	-7.39	5.15	46.92
XB-6-PCB-145	3.250	0.003	-8.04	5.32	46.23
XB-2'-PCB-146	3.249	0.000	-7.76	5.02	46.09
XB-2-PCB-146	3.223	0.006	-7.35	5.51	46.82
XB-3-PCB-146	3.262	0.003	-7.76	4.83	46.82
XB-4'-PCB-146	3.260	0.001	-7.68	4.87	46.85
XB-5'-PCB-146	3.299	-0.002	-7.78	3.95	46.83
XB-5-PCB-146	3.263	-0.001	-8.11	4.76	46.07
XB-2'-PCB-147	3.276	-0.001	-6.37	4.69	45.78
XB-3-PCB-147	3.240	0.005	-8.56	5.21	46.98
XB-4'-PCB-147	3.336	-0.007	-6.36	3.64	45.78
XB-2'-PCB-148	3.222	0.006	-8.67	5.82	46.08
XB-2-PCB-148	3.242	0.006	-6.63	5.41	46.78
XB-3-PCB-148	3.265	0.002	-6.98	4.80	46.80
XB-4'-PCB-148	3.262	0.000	-8.03	5.14	46.13
XB-5-PCB-148	3.287	-0.004	-7.19	4.32	46.05
XB-2-PCB-149	3.266	0.009	-8.18	4.48	46.80
XB-2'-PCB-149	3.271	0.000	-7.47	4.82	46.03
XB-3-PCB-149	3.342	-0.004	-7.90	3.40	46.78
XB-4'-PCB-149	3.278	0.000	-6.41	4.58	46.80
XB-5'-PCB-149	3.268	0.003	-6.11	5.17	46.79
XB-6-PCB-149	3.266	-0.001	-8.18	4.48	45.98
XB-2-PCB-150	3.232	0.005	-6.34	5.64	46.75
XB-3-PCB-150	3.329	-0.002	-6.81	3.64	46.76
XB-4'-PCB-150	3.271	0.000	-6.90	4.94	46.07
XB-6-PCB-150	3.259	0.000	-7.35	5.24	45.98
XB-2'-PCB-151	3.315	-0.003	-6.20	3.97	45.77

XB-2-PCB-151	3.232	0.007	-9.10	5.64	47.01
XB-3-PCB-151	3.240	0.004	-8.23	5.28	46.99
XB-5'-PCB-151	3.357	-0.007	-5.89	3.97	45.79
XB-2'-PCB-152	3.333	-0.004	-6.12	3.67	45.74
XB-2-PCB-152	3.223	0.008	-7.18	5.90	46.99
XB-3-PCB-152	3.242	0.005	-7.08	5.12	46.96
XB-2-PCB-153	3.248	0.002	-7.96	5.08	46.09
XB-4-PCB-153	3.260	0.001	-7.69	4.84	46.85
XB-5-PCB-153	3.238	0.005	-7.27	5.57	46.83
XB-2'-PCB-154	3.227	0.006	-8.48	5.62	46.04
XB-2-PCB-154	3.257	0.002	-7.57	5.10	46.03
XB-4'-PCB-154	3.254	-0.001	-8.55	4.98	46.11
XB-4-PCB-154	3.266	0.000	-6.81	4.77	46.79
XB-5-PCB-154	3.266	0.004	-6.31	5.19	46.81
XB-2-PCB-155	3.247	0.002	-7.54	5.38	46.04
XB-4-PCB-155	3.260	-0.001	-7.18	4.96	46.08
XB-3-PCB-156	3.177	0.016	-8.70	7.46	47.63
XB-4-PCB-156	3.179	0.014	-8.46	7.30	47.69
XB-5-PCB-156	3.415	-0.005	-9.91	2.26	46.93
XB-3'-PCB-156	3.284	0.003	-5.71	4.99	46.62
XB-4'-PCB-156	3.461	-0.009	-6.70	2.40	46.58
XB-3-PCB-157	3.202	0.012	-7.29	6.83	47.53
XB-4-PCB-157	3.255	0.001	-8.54	4.90	46.77
XB-3'-PCB-157	3.295	0.000	-6.98	4.06	46.74
XB-4'-PCB-157	3.221	0.010	-6.44	6.44	47.54
XB-3'-PCB-158	3.293	0.002	-5.07	4.85	46.58
XB-3-PCB-158	3.177	0.014	-8.57	7.46	47.70
XB-4'-PCB-158	3.456	-0.008	-5.70	2.52	46.54
XB-4-PCB-158	3.215	0.007	-9.69	5.74	47.00
XB-3'-PCB-159	3.279	-0.002	-6.93	4.77	45.86

XB-3-PCB-159	3.157	0.019	-8.91	7.96	47.65
XB-4-PCB-159	3.169	0.016	-8.72	7.58	47.72
XB-5-PCB-159	3.214	0.009	-9.02	6.25	46.97
XB-3'-PCB-160	3.408	-0.009	-4.62	3.35	45.49
XB-3-PCB-160	3.162	0.018	-9.07	7.82	47.79
XB-4-PCB-160	3.142	0.022	-9.49	8.41	47.79
XB-3'-PCB-161	3.294	-0.005	-6.19	4.50	45.84
XB-4-PCB-161	3.188	0.010	-9.62	6.55	47.02
XB-3-PCB-161	3.181	0.014	-8.59	7.36	47.73
XB-6-PCB-161	3.215	0.006	-9.50	5.79	46.27
XB-2-PCB-162	3.247	0.007	-9.98	4.77	46.73
XB-3'-PCB-162	3.248	0.005	-7.00	5.60	46.75
XB-3-PCB-162	3.256	0.003	-8.90	4.89	46.82
XB-4'-PCB-162	3.219	0.009	-6.92	6.32	47.56
XB-5-PCB-162	3.249	0.000	-8.95	5.21	46.11
XB-4'-PCB-163	3.454	-0.008	-5.53	2.53	46.54
XB-3-PCB-163	3.240	0.003	-9.28	5.22	47.00
XB-3'-PCB-163	3.287	0.001	-4.74	4.88	46.58
XB-3'-PCB-164	3.262	0.005	-6.15	5.26	46.72
XB-3-PCB-164	3.366	-0.004	-8.67	3.01	46.79
XB-4'-PCB-164	3.231	0.008	-5.34	6.03	47.51
XB-2-PCB-164	3.204	0.008	-7.99	5.53	46.79
XB-6-PCB-164	3.277	0.000	-8.95	4.40	46.00
XB-2-PCB-165	3.195	0.009	-8.57	5.73	47.02
XB-3'-PCB-165	3.295	-0.004	-6.05	4.37	45.84
XB-3-PCB-165	3.230	0.005	-9.43	5.47	47.02
XB-3-PCB-166	3.152	0.018	-9.64	7.90	47.78
XB-4'-PCB-166	3.379	-0.008	-5.03	3.82	45.46
XB-4-PCB-166	3.144	0.023	-9.39	8.46	47.78
XB-4-PCB-167	3.243	0.002	-8.45	5.12	46.90

XB-5-PCB-167	3.240	0.004	-8.11	5.76	46.85
XB-3'-PCB-167	3.230	0.006	-7.21	5.90	46.76
XB-4'-PCB-167	3.221	0.010	-6.26	6.36	47.56
XB-3'-PCB-168	3.426	-0.006	-7.19	2.64	46.73
XB-4'-PCB-168	3.230	0.010	-5.82	6.24	47.51
XB-2-PCB-168	3.221	0.004	-9.32	5.57	46.01
XB-4-PCB-168	3.250	0.001	-9.53	5.37	46.18
XB-3-PCB-169	3.530	-0.008	-8.73	1.60	46.76
XB-4-PCB-169	3.200	0.010	-7.60	6.72	47.61
XB-2-PCB-170	3.252	0.013	-10.82	5.01	46.97
XB-2'-PCB-170	3.199	0.009	-7.77	5.95	46.77
XB-3'-PCB-170	3.205	0.011	-6.96	6.69	47.56
XB-3-PCB-170	3.173	0.018	-8.08	7.67	47.67
XB-4'-PCB-170	3.294	-0.001	-8.43	4.10	46.76
XB-4-PCB-170	3.187	0.016	-7.94	7.25	47.68
XB-5-PCB-170	3.227	0.008	-8.90	5.84	46.95
XB-3'-PCB-171	3.212	0.012	-6.51	6.59	47.54
XB-3-PCB-171	3.175	0.016	-8.65	7.46	47.74
XB-4'-PCB-171	3.297	-0.002	-7.69	4.05	46.72
XB-4-PCB-171	3.212	0.006	-9.56	5.77	46.99
XB-2'-PCB-172	3.209	0.007	-8.01	5.72	46.87
XB-2-PCB-172	3.185	0.012	-8.70	6.34	47.00
XB-3'-PCB-172	3.240	0.003	-8.52	5.28	46.85
XB-3-PCB-172	3.164	0.018	-8.38	7.73	47.69
XB-4-PCB-172	3.179	0.016	-8.23	7.45	47.71
XB-5'-PCB-172	3.255	0.000	-8.73	4.89	46.12
XB-5-PCB-172	3.215	0.008	-8.62	6.13	46.98
XB-2'-PCB-173	3.253	0.004	-5.81	5.55	46.55
XB-3'-PCB-173	3.417	-0.008	-6.29	2.94	46.55
XB-3-PCB-173	3.144	0.021	-9.00	8.21	47.82

XB-4-PCB-173	3.141	0.022	-9.19	8.29	47.79
XB-3'-PCB-174	3.335	-0.003	-8.47	3.46	46.81
XB-3-PCB-174	3.178	0.015	-7.44	7.34	47.65
XB-4-PCB-174	3.185	0.014	-7.32	7.12	47.66
XB-5-PCB-174	3.268	0.002	-8.10	4.47	46.96
XB-6'-PCB-174	3.272	0.000	-8.89	4.32	46.01
XB-3'-PCB-175	3.258	0.002	-7.62	4.90	46.84
XB-3-PCB-175	3.178	0.015	-8.25	7.25	47.76
XB-4-PCB-175	3.185	0.009	-9.27	6.60	47.01
XB-5'-PCB-175	3.258	-0.001	-7.66	4.91	46.09
XB-6-PCB-175	3.212	0.006	-9.53	5.89	46.32
XB-2'-PCB-176	3.216	0.008	-7.44	5.82	46.81
XB-3'-PCB-176	3.384	-0.006	-7.74	2.81	46.78
XB-3-PCB-176	3.188	0.013	-7.34	6.94	47.73
XB-4-PCB-176	3.208	0.008	-8.57	5.97	46.97
XB-6'-PCB-176	3.247	0.001	-8.28	5.18	46.00
XB-2-PCB-177	3.212	0.010	-7.45	6.02	46.73
XB-3'-PCB-177	3.237	0.004	-9.34	5.26	47.01
XB-3-PCB-177	3.207	0.010	-6.40	6.61	47.54
XB-4-PCB-177	3.273	0.001	-7.41	4.58	46.73
XB-2-PCB-178	3.193	0.010	-9.26	6.08	46.81
XB-3-PCB-178	3.232	0.006	-9.35	5.35	46.86
XB-5-PCB-178	3.255	-0.002	-7.62	4.99	46.10
XB-2'-PCB-178	3.196	0.010	-8.99	5.96	47.04
XB-3'-PCB-178	3.229	0.006	-9.39	5.47	47.05
XB-2'-PCB-179	3.219	0.008	-7.29	5.83	46.81
XB-2-PCB-179	3.209	0.009	-8.48	6.13	47.00
XB-3'-PCB-179	3.359	-0.004	-7.55	3.11	46.79
XB-3-PCB-179	3.217	0.006	-8.24	5.93	47.01
XB-6'-PCB-179	3.248	0.001	-7.91	5.09	46.01

XB-2'-PCB-180	3.228	0.003	-8.49	5.43	46.12
XB-2-PCB-180	3.191	0.010	-9.09	6.07	46.97
XB-3-PCB-180	3.167	0.017	-8.52	7.68	47.68
XB-4'-PCB-180	3.250	0.001	-8.35	5.03	46.88
XB-4-PCB-180	3.171	0.016	-8.32	7.68	47.71
XB-5'-PCB-180	3.244	0.004	-7.94	5.50	46.87
XB-5-PCB-180	3.214	0.005	-9.20	5.86	46.97
XB-2'-PCB-181	3.252	0.000	-7.24	5.07	45.80
XB-3-PCB-181	3.143	0.021	-9.49	8.16	47.82
XB-4'-PCB-181	3.322	-0.005	-7.00	3.82	45.82
XB-4-PCB-181	3.140	0.023	-9.33	8.49	47.80
XB-2'-PCB-182	3.206	0.006	-9.27	6.10	46.09
XB-2-PCB-182	3.207	0.010	-8.55	6.05	46.92
XB-3-PCB-182	3.176	0.018	-7.58	7.37	47.67
XB-4'-PCB-182	3.253	0.001	-8.70	5.23	46.17
XB-4-PCB-182	3.181	0.014	-7.68	7.25	47.66
XB-5-PCB-182	3.230	0.008	-7.66	5.88	46.96
XB-2-PCB-183	3.162	0.017	-9.31	6.73	46.98
XB-3-PCB-183	3.178	0.016	-8.54	7.27	47.76
XB-4-PCB-183	3.207	0.007	-9.37	5.64	47.01
XB-6-PCB-183	3.202	0.007	-9.86	6.18	46.31
XB-2'-PCB-183	3.244	0.001	-8.42	5.32	46.04
XB-4'-PCB-183	3.257	0.001	-7.40	4.94	46.84
XB-5'-PCB-183	3.241	0.004	-6.98	5.48	46.84
XB-2-PCB-184	3.178	0.012	-13.79	6.81	46.93
XB-3-PCB-184	3.186	0.015	-7.56	6.99	47.73
XB-4'-PCB-184	3.247	0.000	-8.19	5.16	46.12
XB-6-PCB-184	3.217	0.006	-9.17	6.23	46.28
XB-2'-PCB-185	3.288	-0.002	-6.86	4.42	45.77
XB-5'-PCB-185	3.353	-0.007	-6.75	4.02	45.82

XB-2-PCB-185	3.157	0.017	-9.57	7.05	47.17
XB-3-PCB-185	3.150	0.022	-8.86	8.26	47.84
XB-4-PCB-185	3.135	0.024	-9.06	8.70	47.80
XB-2'-PCB-186	3.279	-0.001	-6.86	4.54	45.76
XB-2-PCB-186	3.192	0.013	-8.77	6.55	47.13
XB-3-PCB-186	3.167	0.019	-7.66	7.62	47.80
XB-4-PCB-186	3.154	0.021	-8.35	7.96	47.76
XB-2'-PCB-187	3.250	0.000	-8.04	5.15	46.07
XB-2-PCB-187	3.184	0.012	-9.12	6.21	47.03
XB-3-PCB-187	3.229	0.004	-9.29	5.44	47.04
XB-4'-PCB-187	3.259	0.001	-7.25	4.89	46.85
XB-5'-PCB-187	3.243	0.003	-7.07	5.51	46.85
XB-2'-PCB-188	3.230	0.004	-8.40	5.68	46.10
XB-2-PCB-188	3.209	0.010	-8.48	6.16	47.01
XB-3-PCB-188	3.248	0.004	-8.56	4.91	47.02
XB-4'-PCB-188	3.264	0.000	-8.02	5.10	46.13
XB-3-PCB-189	3.152	0.019	-9.75	8.14	47.68
XB-4-PCB-189	3.156	0.016	-9.83	7.93	47.75
XB-5-PCB-189	3.208	0.009	-9.83	6.36	47.01
XB-3'-PCB-189	3.237	0.007	-7.50	6.12	46.81
XB-4'-PCB-189	3.202	0.010	-7.50	6.97	47.60
XB-3'-PCB-190	3.269	0.001	-5.72	5.14	46.61
XB-4'-PCB-190	3.444	-0.008	-6.25	2.52	46.58
XB-2-PCB-190	3.193	0.016	-11.90	6.15	47.16
XB-3-PCB-190	3.138	0.020	-10.36	8.28	47.84
XB-4-PCB-190	3.132	0.025	-10.20	8.82	47.83
XB-2-PCB-191	3.149	0.015	-9.91	6.88	46.97
XB-3'-PCB-191	3.250	0.005	-7.00	5.41	46.77
XB-3-PCB-191	3.174	0.018	-9.22	7.68	47.76
XB-4'-PCB-191	3.230	0.010	-5.89	6.14	47.55

XB-4-PCB-191	3.191	0.008	-10.57	6.32	47.06
XB-5'-PCB-191	3.250	-0.001	-7.00	5.41	46.76
XB-2-PCB-192	3.164	0.015	-10.31	6.67	47.19
XB-3'-PCB-192	3.279	-0.002	-6.78	4.74	45.87
XB-3-PCB-192	3.130	0.022	-10.45	8.56	47.86
XB-4-PCB-192	3.125	0.027	-10.23	9.02	47.85
XB-2-PCB-193	3.172	0.012	-9.42	6.33	47.03
XB-3'-PCB-193	3.340	-0.003	-7.30	3.24	46.77
XB-3-PCB-193	3.221	0.006	-10.16	5.59	47.06
XB-4'-PCB-193	3.228	0.011	-5.96	6.26	47.56
XB-2-PCB-194	3.172	0.012	-9.48	6.59	47.01
XB-3-PCB-194	3.159	0.019	-9.17	7.94	47.71
XB-4-PCB-194	3.166	0.016	-9.11	7.63	47.74
XB-5-PCB-194	3.201	0.009	-9.49	6.48	47.01
XB-2'-PCB-195	3.202	0.009	-8.25	6.05	46.74
XB-3'-PCB-195	3.200	0.012	-7.08	6.80	47.57
XB-3-PCB-195	3.135	0.022	-10.20	8.33	47.87
XB-4'-PCB-195	3.334	-0.004	-8.23	3.41	46.76
XB-4-PCB-195	3.130	0.024	-10.00	8.69	47.83
XB-2'-PCB-196	3.150	0.017	-10.40	6.90	47.01
XB-3'-PCB-196	3.163	0.018	-9.39	7.79	47.80
XB-3-PCB-196	3.169	0.017	-8.62	7.57	47.70
XB-4'-PCB-196	3.200	0.007	-10.22	6.04	47.05
XB-4-PCB-196	3.167	0.015	-8.58	7.96	47.70
XB-5-PCB-196	3.211	0.010	-8.61	6.26	47.00
XB-6'-PCB-196	3.193	0.008	-10.81	6.40	46.32
XB-3-PCB-197	3.176	0.016	-8.39	7.22	47.78
XB-4-PCB-197	3.195	0.009	-9.61	6.24	47.02
XB-6-PCB-197	3.207	0.007	-9.97	6.04	46.32
XB-2'-PCB-198	3.207	0.008	-8.28	6.08	46.82

XB-2-PCB-198	3.141	0.017	-10.73	7.08	47.21
XB-3-PCB-198	3.126	0.023	-10.18	8.69	47.88
XB-4-PCB-198	3.124	0.027	-10.12	9.03	47.85
XB-5'-PCB-198	3.249	-0.001	-8.36	5.03	46.13
XB-3'-PCB-198	3.220	0.007	-8.29	5.73	46.89
XB-2'-PCB-199	3.209	0.011	-12.24	5.71	47.05
XB-2-PCB-199	3.186	0.012	-9.18	6.52	46.96
XB-3'-PCB-199	3.185	0.009	-10.04	6.79	47.09
XB-3-PCB-199	3.163	0.017	-8.41	7.73	47.71
XB-4-PCB-199	3.175	0.017	-8.19	7.50	47.70
XB-5-PCB-199	3.240	0.004	-8.97	4.97	47.01
XB-2'-PCB-200	3.195	0.009	-7.79	6.38	46.81
XB-3'-PCB-200	3.360	-0.004	-8.20	3.05	46.84
XB-3-PCB-200	3.141	0.020	-8.88	8.17	47.86
XB-4-PCB-200	3.129	0.024	-9.49	9.17	47.81
XB-6'-PCB-200	3.274	-0.002	-8.84	4.50	46.04
XB-2-PCB-201	3.159	0.016	-9.60	7.20	46.99
XB-3-PCB-201	3.177	0.014	-8.24	7.40	47.77
XB-4-PCB-201	3.199	0.008	-9.43	6.09	47.03
XB-6-PCB-201	3.262	0.001	-12.31	4.80	46.31
XB-3'-PCB-201	3.229	0.004	-9.14	5.28	47.07
XB-2-PCB-202	3.180	0.010	-9.29	6.61	47.03
XB-3-PCB-202	3.208	0.007	-9.27	6.18	47.07
XB-2'-PCB-203	3.319	-0.003	-11.85	3.97	46.07
XB-2-PCB-203	3.133	0.019	-10.80	7.52	47.19
XB-3-PCB-203	3.137	0.021	-10.33	8.32	47.88
XB-4'-PCB-203	3.223	0.004	-8.28	5.85	46.88
XB-4-PCB-203	3.118	0.027	-10.12	9.21	47.85
XB-5'-PCB-203	3.237	0.003	-7.60	5.53	46.88
XB-2'-PCB-204	3.209	0.005	-9.14	6.04	46.11

XB-2-PCB-204	3.203	0.011	-12.46	5.82	47.16
XB-3-PCB-204	3.140	0.020	-9.46	8.17	47.86
XB-4'-PCB-204	3.255	0.001	-8.68	5.25	46.16
XB-4-PCB-204	3.132	0.022	-9.53	8.52	47.81
XB-2-PCB-205	3.122	0.020	-11.58	7.44	47.20
XB-3'-PCB-205	3.223	0.005	-7.64	5.85	46.80
XB-3-PCB-205	3.127	0.022	-10.90	8.65	47.90
XB-4'-PCB-205	3.220	0.012	-6.65	6.44	47.59
XB-4-PCB-205	3.109	0.029	-11.02	9.62	47.88
XB-2'-PCB-206	3.214	0.011	-15.59	5.54	46.97
XB-2-PCB-206	3.188	0.014	-13.84	6.09	47.22
XB-3'-PCB-206	3.158	0.019	-9.16	7.93	47.74
XB-3-PCB-206	3.128	0.024	-11.05	8.61	47.92
XB-4'-PCB-206	3.205	0.015	-12.38	5.87	47.73
XB-4-PCB-206	3.109	0.029	-10.98	9.56	47.87
XB-5'-PCB-206	3.200	0.010	-9.13	6.51	47.03
XB-2'-PCB-207	3.145	0.017	-10.24	7.58	47.00
XB-3'-PCB-207	3.165	0.016	-9.05	7.68	47.79
XB-3-PCB-207	3.136	0.022	-10.08	8.28	47.90
XB-4'-PCB-207	3.205	0.007	-9.94	5.87	47.05
XB-4-PCB-207	3.121	0.027	-9.92	9.09	47.84
XB-6'-PCB-207	3.189	0.007	-10.52	6.51	46.32
XB-2'-PCB-208	3.172	0.012	-9.93	6.83	47.04
XB-2-PCB-208	3.136	0.018	-10.77	7.71	47.20
XB-3'-PCB-208	3.216	0.007	-9.71	5.67	47.10
XB-3-PCB-208	3.125	0.022	-10.03	8.63	47.90
XB-4-PCB-208	3.116	0.027	-10.17	9.31	47.86
XB-2-PCB-209	3.129	0.019	-11.62	7.94	47.21
XB-3-PCB-209	3.127	0.022	-10.77	8.56	47.92
XB-4-PCB-209	3.105	0.027	-10.84	9.33	47.88

APPENDIX D

LICENSE FOR USE OF CHAPTER 2 IN DISSERTATION

JOHN WILEY AND SONS LICENSE
TERMS AND CONDITIONS

Feb 20, 2021

This Agreement between Old Dominion University -- Eric Marsan ("You") and John Wiley and Sons ("John Wiley and Sons") consists of your license details and the terms and conditions provided by John Wiley and Sons and Copyright Clearance Center.

License Number	5005000555392
License date	Feb 09, 2021
Licensed Content Publisher	John Wiley and Sons
Licensed Content Publication	Chemistry - A European Journal
Licensed Content Title	Halogen-Bonding Interactions of Polybrominated Diphenyl Ethers and Thyroid Hormone Derivatives: A Potential Mechanism for the Inhibition of Iodothyronine Deiodinase
Licensed Content Author	Craig A. Bayse, Eric S. Marsan
Licensed Content Date	Apr 10, 2017
Licensed Content Volume	23
Licensed Content Issue	27
Licensed Content Pages	9
Type of use	Dissertation/Thesis
Requestor type	Author of this Wiley article
Format	Electronic
Portion	Full article
Will you be translating?	No
Title	COMPUTATIONAL ANALYSIS OF TYPE 3 DEIODINASE: DIMER STRUCTURE, MOLECULAR DYNAMICS SIMULATIONS, SUBSTRATE BINDING, AND POTENTIAL INHIBITORS
Institution name	Old Dominion University

APPENDIX E

LICENSE FOR USE OF CHAPTER 3 IN DISSERTATION

JOHN WILEY AND SONS LICENSE
TERMS AND CONDITIONS

Feb 20, 2021

This Agreement between Old Dominion University -- Eric Marsan ("You") and John Wiley and Sons ("John Wiley and Sons") consists of your license details and the terms and conditions provided by John Wiley and Sons and Copyright Clearance Center.

License Number	5005000898482
License date	Feb 09, 2021
Licensed Content Publisher	John Wiley and Sons
Licensed Content Publication	Chemistry - A European Journal
Licensed Content Title	Halogen Bonding Interactions of Polychlorinated Biphenyls and the Potential for Thyroid Disruption
Licensed Content Author	Eric S. Marsan, Craig A. Bayse
Licensed Content Date	Feb 25, 2020
Licensed Content Volume	26
Licensed Content Issue	23
Licensed Content Pages	8
Type of use	Dissertation/Thesis
Requestor type	Author of this Wiley article
Format	Electronic
Portion	Full article
Will you be translating?	No
Title	COMPUTATIONAL ANALYSIS OF TYPE 3 DEIODINASE: DIMER STRUCTURE, MOLECULAR DYNAMICS SIMULATIONS, SUBSTRATE BINDING, AND POTENTIAL INHIBITORS
Institution name	Old Dominion University

VITA

ERIC SCOTT MARSAN

Department of Chemistry and Biochemistry
4541 Hampton Boulevard
Old Dominion University
Norfolk, VA 23508

Office Tel: (757) 683-4078
Home Tel: (703) 999-3546
Fax: (757) 683-4628
Email: emarsan@odu.edu

EDUCATION

Ph.D. in Chemistry, College of Sciences, Old Dominion University, Norfolk, VA. Major field: Computational Chemistry. Dissertation: *Computational Analysis of Type 3 Iodothyronine Deiodinase: Potential Inhibitors, Substrate Binding, and Dimer Structure.* Expected August 2021.

Bachelor of Science, Chemistry, Christopher Newport University, Newport News, VA. May 2015.

PUBLICATIONS

Bayse, Craig A.; Marsan, Eric S.; Garcia, Jenna A.; Tran-Thompson, Alexis T. Thyroxine Binding to Type III Deiodinase. *Sci. Reports* **2020,** *10,* 15401.

Marsan, Eric S.; Bayse, Craig A. A Halogen Bonding Perspective on Iodothyronine Deiodinase Activity. *Molecules* **2020,** *25* (6), 1328.

Marsan, Eric S.; Bayse, Craig A. Halogen Bonding in Polychlorinated Biphenyls: Potential Inhibitors of Iodothyronine Deiodinase. *Chem. Eur. J.* **2020,** *26*, 5200-5207.

Marsan, Eric S.; Bayse, Craig A. Halogen-Bonding Interactions of Polybrominated Diphenyl Ethers and Thyroid Hormone Derivatives: A Potential Mechanism for the Inhibition of Iodothyronine Deiodinase. *Chem. Eur. J.* **2017,** *23*, 6625-6633.

Tabackman, Alexa A.; Frankson, Rochelle; Marsan, Eric S.; Perry, Kay; Cole, Kathryn E. Structure of 'linkerless' hydroxamic acid inhibitor-HDAC8 complex confirms the formation of an isoform-specific subpocket. *J. Struct. Biol.,* **2016,** *195*, 373-378.

PRESENTATIONS

Marsan, Eric S.; Bayse, Craig A. *Effect of Dimerization and Halogen Bonding on Substrate Binding to the Thyroid Hormone Deactivating Deiodinase 3 Protein.* A Presentation at the Biochemistry and Chemistry Seminar Series at Old Dominion University, Norfolk VA, October 2019.

Marsan, Eric S.; Bayse, Craig A. *Effect of Dimerization and Halogen Bonding on Substrate Binding to the Thyroid Hormone Deactivating Deiodinase 3 Protein.* American Chemical Society National Meeting and Exposition, Orlando FL, April 2019.

Marsan, Eric S.; Bayse, Craig A. *Halogen-Bonding Interactions of Polybrominated Diphenyl Ethers and Thyroid Hormone Derivatives: A Potential Mechanism for the Inhibition of Iodothyronine Deiodinase.* Poster Presentation at the American Chemical Society National Meeting and Exposition, Washington D.C., August 2017.